

**COMMISSIONING OF THE ATLAS LIQUID ARGON
CALORIMETERS**

by

Erfan Rezaie

B.Sc., University of British Columbia, 2005

A THESIS SUBMITTED IN PARTIAL FULFILLMENT
OF THE REQUIREMENTS FOR THE DEGREE OF
MASTER OF SCIENCE
in the Department of Physics

© Erfan Rezaie 2008
SIMON FRASER UNIVERSITY
Spring 2008

All rights reserved. This work may not be
reproduced in whole or in part, by photocopy
or other means, without the permission of the author.

APPROVAL

Name: Erfan Rezaie
Degree: Master of Science
Title of thesis: Commissioning of the ATLAS Liquid Argon Calorimeters

Examining Committee: Dr. H. Trottier, Professor, Department of Physics, SFU
Chair

Dr. M. Vetterli, Professor, Department of Physics,
SFU/TRIUMF
Senior Supervisor

Dr. D. O'Neil, Assistant Professor, Department of
Physics, SFU
Supervisor

Dr. R. McPherson, Associate Professor,
IPP/UVIC
Supervisor

Dr. S. Johnson, Senior Lecturer, Department of
Physics, SFU
Internal Examiner

Date Approved: March 4, 2008



SIMON FRASER UNIVERSITY
LIBRARY

Declaration of Partial Copyright Licence

The author, whose copyright is declared on the title page of this work, has granted to Simon Fraser University the right to lend this thesis, project or extended essay to users of the Simon Fraser University Library, and to make partial or single copies only for such users or in response to a request from the library of any other university, or other educational institution, on its own behalf or for one of its users.

The author has further granted permission to Simon Fraser University to keep or make a digital copy for use in its circulating collection (currently available to the public at the "Institutional Repository" link of the SFU Library website <www.lib.sfu.ca> at: <<http://ir.lib.sfu.ca/handle/1892/112>>) and, without changing the content, to translate the thesis/project or extended essays, if technically possible, to any medium or format for the purpose of preservation of the digital work.

The author has further agreed that permission for multiple copying of this work for scholarly purposes may be granted by either the author or the Dean of Graduate Studies.

It is understood that copying or publication of this work for financial gain shall not be allowed without the author's written permission.

Permission for public performance, or limited permission for private scholarly use, of any multimedia materials forming part of this work, may have been granted by the author. This information may be found on the separately catalogued multimedia material and in the signed Partial Copyright Licence.

While licensing SFU to permit the above uses, the author retains copyright in the thesis, project or extended essays, including the right to change the work for subsequent purposes, including editing and publishing the work in whole or in part, and licensing other parties, as the author may desire.

The original Partial Copyright Licence attesting to these terms, and signed by this author, may be found in the original bound copy of this work, retained in the Simon Fraser University Archive.

Simon Fraser University Library
Burnaby, BC, Canada

Abstract

ATLAS, a multi-purpose detector built at the LHC at CERN, requires an extensive commissioning campaign to be ready for proton-proton collisions. In this work, we focus on the commissioning of the liquid Argon (LAr) calorimeters, with emphasis on commissioning with cosmic rays. First we outline one phase of the commissioning work, which involves testing of the front-end electronics of the two endcap calorimeters. We then describe two cosmic ray generators as input to a Monte-Carlo simulation of cosmic rays in ATLAS, and compare their results. Finally, we explain a technique developed for this work which uses information from the Tile calorimeters to predict the timing of cosmic rays within the LAr calorimeters, because cosmic rays occur randomly in time whereas the electronics are clocked at $\frac{1}{40.08 \text{ MHz}}$. The results from this analysis tool are compared to default tools, using both simulated and real cosmic ray data in the calorimeters.

Acknowledgments

There are a great number of people without whom this thesis would not have been possible.

First and foremost is of course my main supervisor, Mike Vetterli, who allowed me to pursue this topic and supported it throughout. I am grateful for his time and advice. Dugan O'Neil also served as a key adviser on many issues and lent valuable knowledge when it was needed.

There are a couple other senior collaborators on ATLAS whose help was invaluable. These include my external supervisor, Rob McPherson, who probably knows more about the detector than anyone else I know, and Hong Ma, who may compete with Rob in that category. I am indebted to both of these people for their knowledge and timely responses to my many queries.

Many people in the ATLAS Canada collaboration either directly or indirectly helped in producing some of the work in this thesis. These include, in no particular order, Manuella Vincter, Peter Krieger, Richard Teuscher, and Rolf Seuster.

I will always remember the help the following graduate students lent me; Tayfun Ince, Gabe Rosenbaum, Eduardo Nebot Del Busto, and Bin Guo. In particular, thanks to Gabe for his vast expertise in all areas and to Bin for his help with Athena, Atlantis, and more.

Thank you to the entire ATLAS Liquid Argon Commissioning crew for the training and assistance during my shift work and analysis.

Of course I want to thank all past and present members of the SFU High Energy Physics group. These include, in no particular order, Marco Bieri, Doug Schouten, Dag Gillberg, Travis Stewart, Gary Pike, Zhiyi Liu, Jennifer Godfrey, Yann Codeau, Jyothsna Rani, and Dr. Walker. In particular, thanks to Rod Walker for all his help in using computing grid tools and to Doug Schouten for using Athena, and almost everything else I needed help with.

Finally, thanks to my family and friends who were always curious and supportive in all my endeavors.

Contents

Approval	ii
Abstract	iii
Acknowledgments	iv
Contents	vi
List of Tables	ix
List of Figures	x
1 Introduction	1
1.1 The Large Hadron Collider	1
1.2 The ATLAS Experiment	3
1.2.1 Physics Motivation	5
1.2.2 Coordinate System	7
1.2.3 Detectors	7
1.2.4 ATLAS Software	11
2 Calorimetry and the ATLAS Calorimeters	14
2.1 Calorimetry	14
2.1.1 Particle Interactions	15
2.1.2 Particle Showers	17
2.1.3 Sampling Calorimeters	18
2.2 The ATLAS Calorimeters	18
2.2.1 Electromagnetic Barrel (EMB) and End-Cap (EMEC) Calorimeters .	20

2.2.2	Hadronic End-Cap (HEC) Calorimeter	21
2.2.3	Forward Calorimeter (FCAL)	26
2.2.4	Hadronic Tile Calorimeter	26
3	Calorimeter Commissioning	29
3.1	Purpose	29
3.2	Commissioning Phases	30
3.2.1	Warm/Cold Commissioning	31
3.2.2	Commissioning with Cosmic Ray Muons	33
4	Warm/Cold Commissioning of End-Cap Calorimeters	36
4.1	Electronics Layout	36
4.1.1	Front-End Boards	38
4.2	Calibration Data	38
4.2.1	Pedestal Runs	39
4.2.2	Delay Runs	39
4.2.3	Ramp Runs	43
5	Monte-Carlo Simulation of Cosmic Rays	45
5.1	Motivation	46
5.2	Cosmic Ray Generators	46
5.2.1	Muon Gun Generator	47
5.2.2	Air Shower Generator	48
5.3	Simulation and Digitization	50
5.4	Results	54
6	Cosmic Ray Reconstruction and Analysis	58
6.1	Signal Reconstruction	58
6.1.1	Reconstruction Tools and Timing	60
6.2	Using Tile Calorimeters	61
6.2.1	Tile Timing Tool	63
6.3	Cosmic Ray MC Analysis	66
6.4	Distribution of the LAr Cell Timing	70
6.4.1	MC Cosmic Rays in the EM Barrel Calorimeter	70

6.4.2	MC Cosmic Rays in the Endcap Calorimeters	75
6.5	Cosmic Ray Data Analysis	76
6.5.1	Setup	76
6.5.2	Combined LAr/Tile Barrel Runs	79
6.5.3	Combined LAr/Tile End-Cap Runs	80
6.6	Cosmic Ray Energy Deposits	82
7	Conclusion and Outlook	87
	Bibliography	89
A	LAr Mapping Diagrams	92

List of Tables

5.1	Parameters of each muon gun dataset used in this study.	48
5.2	Parameters used for the air shower simulations produced for this work using CORSIKA.	50
6.1	Parameters used for the Iteration peak reconstruction tool.	61
6.2	Details of the cosmic ray data taking periods used for this analysis. This information is taken mainly from [23]. Under the LAr Crates and Tile Modules columns, the top rows refer to the top sections of the calorimeter ($y > 0$) and the bottom rows refer to the bottom calorimeter sections ($y < 0$). The layouts of the LAr crates are given in Appendix A.	78

List of Figures

1.1	A schematic of the LHC ring is shown along with the four main experiments, including ATLAS [1].	2
1.2	The proton accelerator chain consisting of the Linac2 (50 MeV), PSB (1.4 GeV), PS (26 GeV), and SPS (450 GeV) prior to injection into the LHC ring [3]. . .	4
1.3	Shown here is the ATLAS experiment comprised of the various detector elements [5].	6
1.4	The ATLAS Inner Detector [5].	9
1.5	The ATLAS LAr and Tile calorimeters [5].	10
1.6	The ATLAS muon spectrometers [5].	12
1.7	A flow diagram of the full chain of Monte-Carlo production using ATLAS software.	13
2.1	Contributions to the photon interaction cross-section in lead. The relevant symbols here are $\sigma_{p,e}$ (Photoelectric effect), $\sigma_{Compton}$ (Compton scattering), $\sigma_{Rayleigh}$ (Rayleigh Scattering), and κ_{nuc} or κ_e (Pair production off the nucleus or electron). This figure is taken from [6].	16
2.2	An example of an electromagnetic shower initiated by an electron.	17
2.3	A simplified example of one layer of a LAr/absorber sampling calorimeter. Here a particle initiates a shower within the absorber and the charged particles ionize the LAr, inducing a current in the readout electrode.	19
2.4	A cut out of the EM barrel calorimeter (left) and the EMEC inner and outer wheels showing the accordion structure (right) [4].	20
2.5	A view of the granularity of the different segments of the EM barrel [4].	22
2.6	A cut out of the EM endcap calorimeter (EMEC) [4].	23
2.7	A HEC module showing a cutaway of the read-out structure [1].	24

2.8	A cut out view of the four LAr gaps and readout electrode structure contained between two copper plates in the HEC [4].	25
2.9	An image showing the FCAL matrix employing rods and tubes [4].	27
2.10	A module of the Tile calorimeter consisting of vertical scintillating plastic tiles in an iron absorber [4].	28
3.1	A picture taken after installation of the LAr barrel calorimeter (centre), surrounded here by the magnetic toroids, before being moved into position in Nov. 2005. Soon after, the front-end electronics were tested.	30
3.2	A LAr endcap was installed in spring 2006. Shortly after, each electronic crate was connected and electronics calibration runs were performed for each electronic channel.	32
3.3	A cosmic ray event from Monte-Carlo simulations shown here in the LAr barrel using the Atlantis event display software.	34
4.1	An open view of an endcap cryostat showing the cold to warm feedthroughs connecting the calorimeter cells to the front-end electronics [11].	37
4.2	The allocation of feedthroughs in the endcaps [11].	38
4.3	Examples of a noisy (top) and dead (bottom) channel found in pedestal runs during warm calibration data taking. If the RMS is significantly higher than the average of all other channels, it is an indication of a noisy channel, whereas a dead channel typically displays a small RMS compared to the average. . . .	40
4.4	A comparison of the pedestal RMS of a warm (red/top) and cold (black/bottom) run for the same FEB. Note that the noise is reduced at LAr temperature. . .	41
4.5	Examples of problems found monitoring delay runs. Clockwise from top left: An example of a dead channel, a distorted channel, and a fast-shaper problem on a FEB.	42
4.6	An example of a ramp run showing the slope (top) and offset (bottom) of the DAC to ADC linear relationship. A comparison with a reference run (red) indicated that, in this particular case, the cabling of a group of channels in a FEB (black) had changed from the default (red).	44
5.1	The coordinate system used in CORSIKA [17].	51

5.2	An air shower created by a primary proton with energy 1 TeV and $\theta_p = 0$ simulated by CORSIKA. All other parameters are the same as in Table 5.2. Here the blue lines correspond to hadrons, whereas the red lines correspond to muons. The plot dimensions are ± 5 km in the x and y directions (perpendicular to the shower axis) from center and from a surface altitude of 507.3 m to the first interaction height of 30 km.	52
5.3	A graphical representation of the simulation of cosmic rays in ATLAS. The layout here is of the ATLAS cavern, access shafts, and surface buildings using Geant3, similar to the current Geant4 simulation [9].	53
5.4	A comparison of the angle of the muons with respect to the vertical (left) and the momentum of the muons (right) at the surface, for the muon gun dataset 4950 (black) and the air shower simulation (red).	55
5.5	A comparison of the LAr cell energy for muon gun dataset 4950 and the air shower simulation.	55
5.6	A comparison of the angle of the muons with respect to the vertical (left) and the momentum of the muons (right) at the surface, for air showers caused by α -particles (red) and protons (black). These are for all muons on the surface which pass the optimization cuts, such as passing through a sphere of radius 25 m, centred around the IP.	56
5.7	A comparison of the angle of the muons with respect to the vertical (left) and the momentum of the muons (right) at the surface, for air showers caused by α -particles (red) and protons (black). These are only for muons which pass the optimization cuts and produce a hit within ATLAS.	57
6.1	The LAr ionization current pulse and the shaped signal with the 25 ns time samples given by the points [11].	59
6.2	The layout of the Tile trigger boards used in coincidence for cosmic data taking.	62
6.3	The response of the TMF algorithm after applying artificial trigger times using a constant of 40 ns (left) and a Gaussian distribution with $\sigma = 10$ ns (right). Plotted here is the time from TMF at $y = 0$ using cosmic ray MC dataset 4936.	63

6.4	The global time offset t_{global} for each FEB in the top (left) and bottom (right) LAr sections having at least 50 muon hits each with a minimum cell energy deposit of 300 MeV. This is from all cosmic data taken in the EM barrel. Details of these data are given in Section 6.5.	65
6.5	A check of the TileInfo tool performed by applying artificial trigger times during the digitization of MC dataset 4936. A constant offset of 40 ns (left) and a random offset from Gaussian distribution with $\sigma = 10$ ns (right) are applied.	66
6.6	Result of the calculation of the global time offset t_{global} for MC dataset 5003 (LAr Endcap) in the top (left) and bottom (right) LAr sections. The peaks on the left and right of each plot correspond respectively to muon hits in the Tile barrel and extended barrel regions.	67
6.7	A Gaussian fit of the global time offset t_{global} in the endcap region for the top (left) and bottom (right) LAr sections.	68
6.8	The results of the LAr cell times found in the EMEC using the TileInfo and Iteration tools. The plot on the left is for LAr cells with a minimum energy of 150 MeV, while the plot on the right is for cells with energy less than 150 MeV, but greater than zero.	69
6.9	The results of the LAr cell times for MC dataset 5003 with noise included, found using the Iteration (left), Fixed (center), and TileInfo (right) tools. The minimum LAr cell energy required is 450 MeV.	70
6.10	The timing in the LAr cells for dataset 4936 found using the Iteration (left) and TileInfo (right) methods of reconstruction. The minimum cell energy is required to be 150 MeV and only muons within the Tile and LAr barrel regions are included.	71
6.11	The LAr cell timing using the Iteration method with only those muons included which have a hit in both the top and bottom sections of the LAr barrel calorimeter.	72
6.12	Similar to Figure 6.11, except that here only the middle layer of the LAr barrel calorimeter is included.	72
6.13	The same as in Figure 6.12, except that the top (left) and bottom (right) sections of the LAr calorimeter are shown separately.	73

6.14	As in Figure 6.13, but including only those events which produce hits within the designated cylinder around the IP.	74
6.15	The same as in Figure 6.12, except here with a cut on projectivity using the η and ϕ values of the cells for each event. Only those events are included that produce hits in cells with η and ϕ values that fall within the granularity of middle layer cells.	74
6.16	The LAr cell timing distribution in the EMEC using the Iteration tool on MC dataset 5003. This is performed for a minimum cell energy of 50 MeV (left) and 150 MeV (right).	75
6.17	The LAr cell timing distribution in the HEC using the Iteration tool on MC dataset 5003. This is performed for a minimum cell energy of 150 MeV (left) and 850 MeV (right).	76
6.18	A Gaussian fit of the global time offset t_{global} between the LAr and Tile barrel calorimeters for the top (left) and bottom (right) LAr sections.	80
6.19	A comparison between the results of the LAr cell times for EM barrel data taken in Aug/Oct 2006.	81
6.20	The TOF of each LAr cell to the $y = 0$ plane (TOF_{IP} and $TOF_{y=0}$) as a function of the cell time for projective cosmic muon events in the LAr barrel. The left plot is for cells in the top section and the right for cells in the bottom section.	81
6.21	The LAr cell coverage during the combined LAr/Tile cosmic data taking period of Jun/Jul 07. The cells shown here are only those for which calibration data were available.	83
6.22	The results of the LAr cell times for cosmic data taken in the HEC, on the A-side. The cell times are computed using the Iteration (left) and TileInfo (right) tools for comparison. The minimum cell energy required in the HEC is 500 MeV in this case.	83
6.23	The energy deposited per cell for MC dataset 5003 with noise included, found using the Iteration, Fixed, and TileInfo reconstruction methods. The minimum LAr cell energy required is 450 MeV.	84
6.24	The energy deposited per cell for real data in the LAr electromagnetic barrel (EMB) calorimeter using each of the reconstruction methods; TileInfo, Iteration, and Fixed.	85

6.25	The energy deposited per cell in the LAr hadronic endcap (HEC) calorimeter using the Iteration (left) and TileInfo (right) reconstruction tools.	85
6.26	The energy deposited per cell in the LAr hadronic endcap (HEC) calorimeter for MC dataset 5003 with noise included (left) and real data (right) using the TileInfo reconstruction tool.	86
A.1	The mapping of the crates in LAr barrel on the A-side (top) and C-side (bottom).	93
A.2	The mapping of the crates in LAr endcap on the A-side.	94

Chapter 1

Introduction

The world's largest particle accelerator, the LHC (Large Hadron Collider), is set to collide protons in 2008. One of the four detectors, ATLAS (A Toroidal LHC Apparatus), has been installed and integrated with the underground accelerator ring. Many of its components have already been tested and final commissioning is being performed to ensure everything is ready when data taking begins.

After an introduction to the ATLAS detector and its components, particularly the calorimeters, and an overview of calorimetry, this work focuses on the commissioning of the LAr (Liquid Argon) calorimeters. The emphasis is placed on commissioning with cosmic rays. The first chapters are to relay to the reader the importance of commissioning a detector as complex as ATLAS, focusing on the LAr calorimeters.

1.1 The Large Hadron Collider

After the successes of high energy particle accelerators such as LEP (Large Electron-Positron) at CERN, the Tevatron at Fermilab, and others¹, the LHC is the next step in collider physics. It has the primary goal of answering questions raised by the Standard Model of Particle Physics, particularly the need to discover the Higgs boson, but also to potentially uncover something new and perhaps unexpected, in the realm of the fundamental particles of nature. More of the physics motivation behind the construction of the LHC will be covered in the following section.

¹RHIC at BNL, HERA at DESY, PEP-II at SLAC

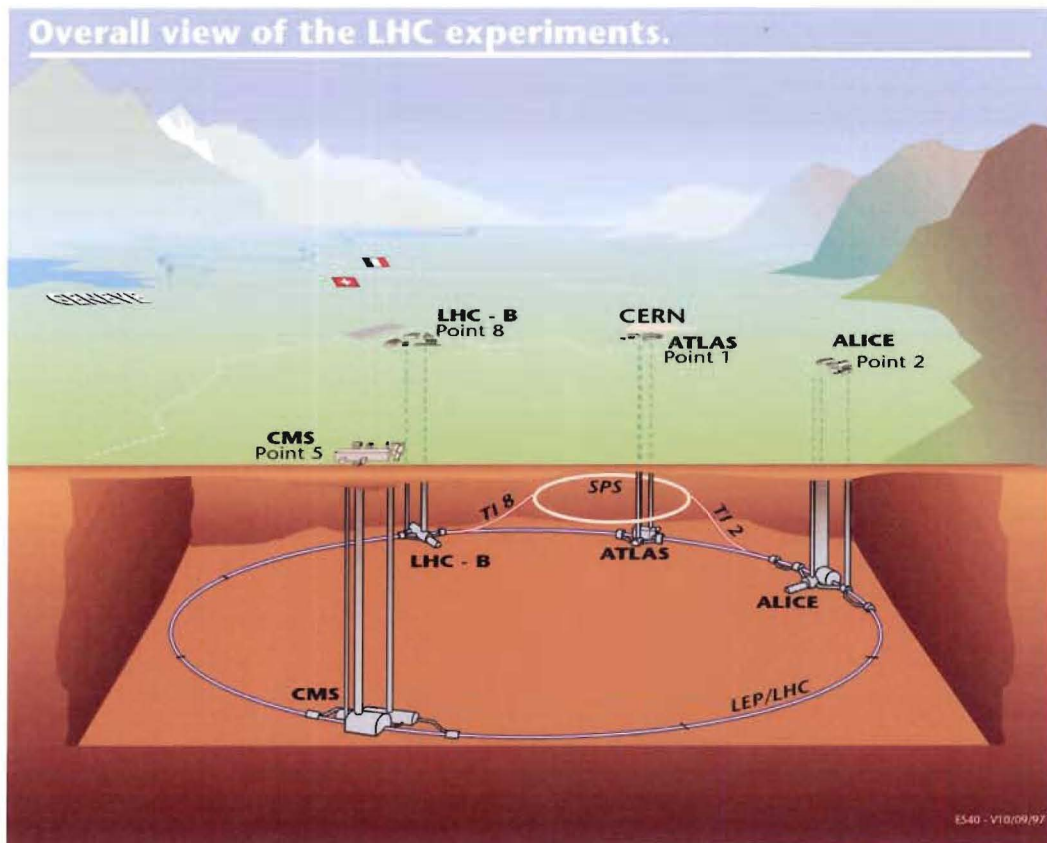


Figure 1.1: A schematic of the LHC ring is shown along with the four main experiments, including ATLAS [1].

The LHC is 27 km in circumference and spans the French-Swiss border near Geneva, Switzerland (Fig. 1.1). It will collide 7 TeV (10^{12} electron-Volts) protons on 7 TeV protons, to be the highest energy collider to date at 14 TeV in the centre of mass frame. The machine luminosity, or beam intensity, is designed to peak at 10^{34} $\text{cm}^{-2}\text{s}^{-1}$, which was determined by the physics goals of ATLAS and the other high luminosity experiment on the LHC ring, CMS (Compact Muon Solenoid). This design luminosity is a function of the number of proton bunches per beam (2808) and the number of protons per bunch (1.15×10^{11}), as well as the revolution frequency and the beam optics configuration [2]. These proton bunches are intended to cross each other every 25 ns, or with a frequency of 40 MHz, with an average of 23 $p - p$ (proton-proton) collisions per bunch. ATLAS was specifically designed with these collision rates in mind.

Since the LHC is being constructed in the LEP tunnel, the existing injection accelerators were upgraded to be used for pre-acceleration of the protons prior to being injected into the LHC ring. This injector chain comprises the Linac2 (Linear Accelerator), the PSB (Proton Synchrotron Booster), the PS (Proton Synchrotron), and the SPS (Super Proton Synchrotron) as shown in Fig. 1.2. Starting from 1.4 GeV at the Linac2, the various Proton Synchrotrons increase the proton beam energy to 450 GeV before entering the LHC. From there, superconducting magnets steer the two proton beams in opposite directions. There exists also the capability to accelerate heavy ions, such as Pb, to collide with one another for use in particular for the ALICE experiment.

1.2 The ATLAS Experiment

ATLAS was designed to be a multi-purpose LHC detector, with strong emphasis on making a discovery of the Higgs boson as well as physics beyond the Standard Model such as SUSY (Super-Symmetry). The physics goals outlined below, predominantly determine the design choices for the various detectors that make up ATLAS. The main criteria include efficient tracking, particularly at high luminosity, high precision calorimetry, and muon spectrometers to track muons on their own, without information from other detector systems. A large angular coverage and good decision making for reading out signals (triggering), particularly for low momentum collisions were also part of the design criteria. Apart from physics goals, the design and particularly the materials chosen were determined by the high radiation environment of the colliding proton beams, and the cost.

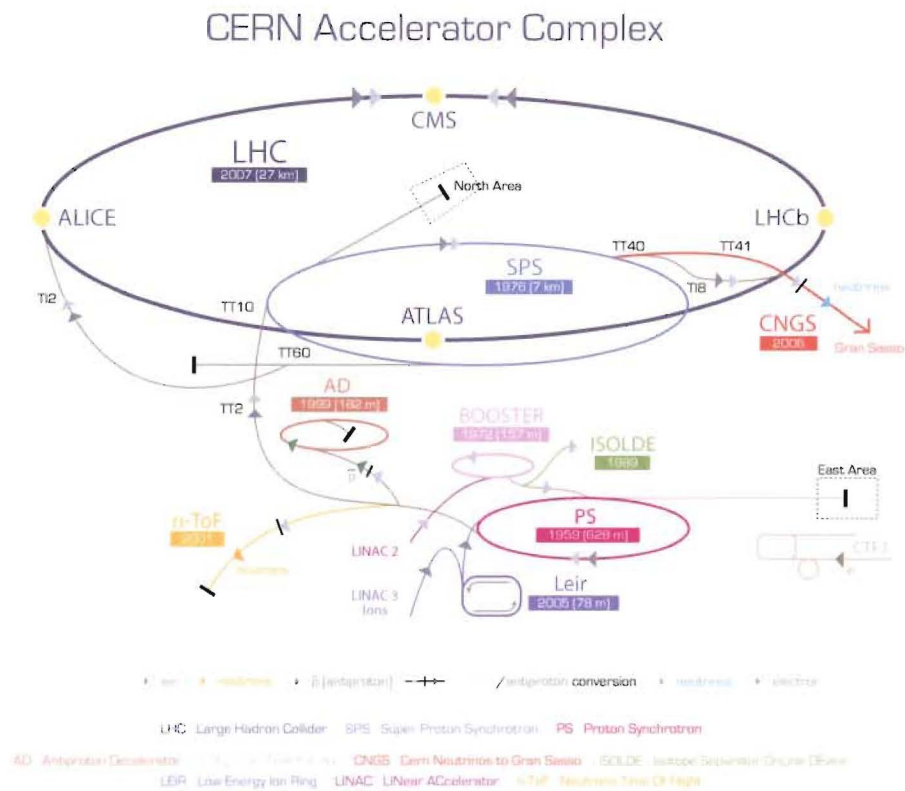


Figure 1.2: The proton accelerator chain consisting of the Linac2 (50 MeV), PSB (1.4 GeV), PS (26 GeV), and SPS (450 GeV) prior to injection into the LHC ring [3].

The ATLAS detector is comprised of many sub-detectors including the inner detectors for tracking, electromagnetic and hadronic calorimeters, muon spectrometers, and two different magnetic field configurations used for tracking particle trajectories. Altogether, the detector is almost cylindrical in shape at 44 m long with a diameter of 25 m. It weighs over 7000 tons, and is shown in Fig. 1.3. In the sections to follow, only a brief overview of each detector component is given; a full review can be found in the ATLAS Technical Design Report (TDR) [4].

1.2.1 Physics Motivation

The Standard Model (SM) of Particle Physics is currently the best theoretical framework used to describe the fundamental particles and their interactions. It has been very successful at predicting, for example, the existence of the W and Z bosons as well as nearly every one of its components. One major component of the SM, however, has yet to be observed by any experiment. This is the Higgs boson, which is predicted to exist and act as the manifestation of the Higgs field, a mechanism through which the fundamental particles are thought to gain their mass. This Higgs mechanism is responsible for the spontaneous breaking of the electroweak symmetry, which must occur in order to explain the non-zero mass of the W and Z bosons. A discovery, or perhaps exclusion, of a Higgs boson is one of the primary mandates of the LHC and ATLAS, since it could potentially make or break the SM.

Many have been looking beyond the SM for decades now, since its 19 free parameters force many to believe that the SM could be a subset of a more elegant theory that unifies all the fundamental forces of nature. The most popular theory extending the SM is SUSY, which predicts the existence of super-partners to the SM particles, some of which are predicted to exist at the TeV energy scale. To this end, ATLAS was designed to be able to detect, with high precision, events with missing energy and multiple jets of particles created through decays of supersymmetric particles.

If the SM is in fact confirmed with the discovery of a Higgs boson, there are still many parameters which require higher precision measurements. ATLAS was also designed to make precision measurements of quantities, such as the masses of quarks and the elements of the CKM matrix, which describe the mixing of quark generations.

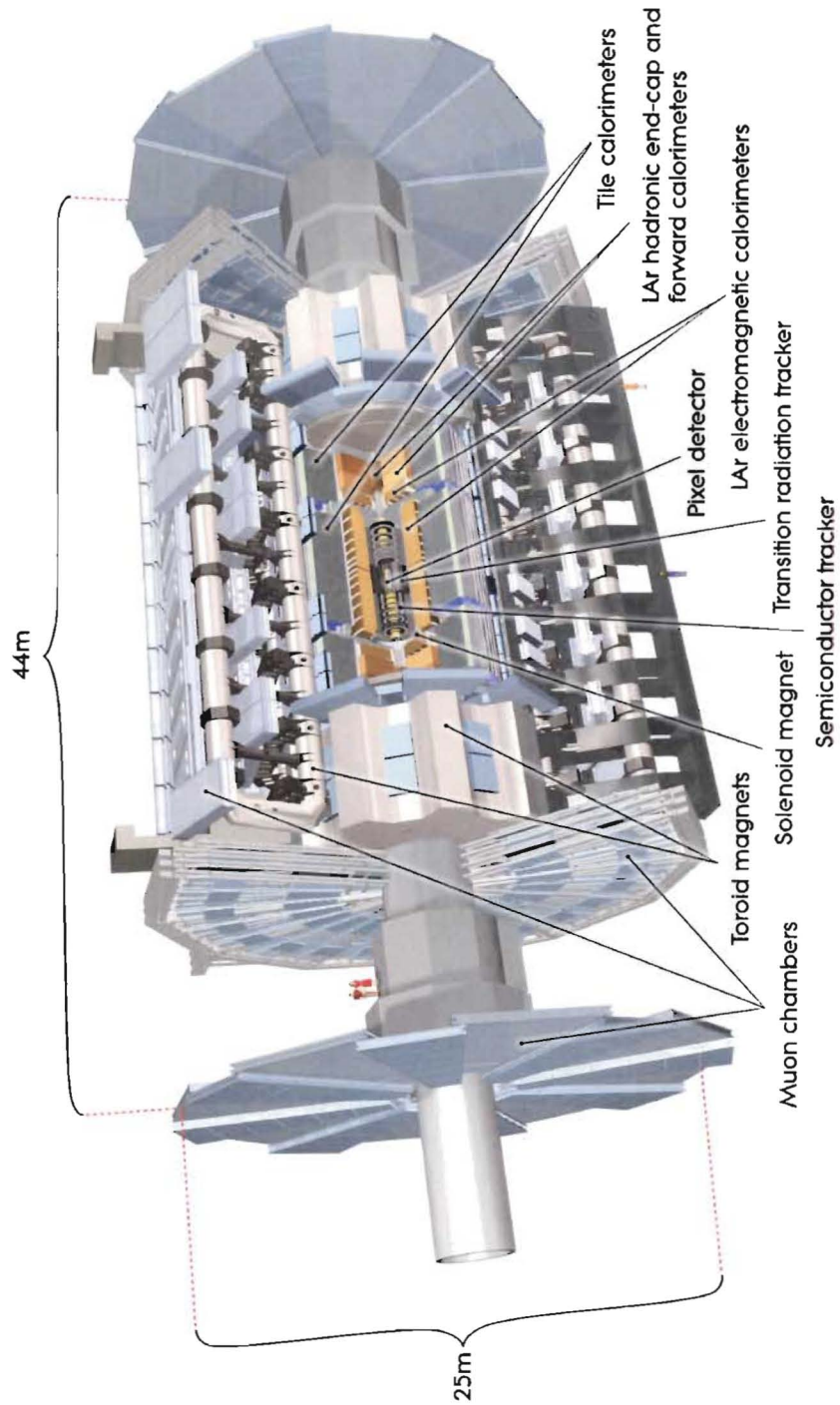


Figure 1.3: Shown here is the ATLAS experiment comprised of the various detector elements [5].

1.2.2 Coordinate System

Many of the descriptions in the following sections on the detector elements will require knowledge of how the coordinate system in ATLAS is defined. In ATLAS, the (x, y, z) coordinates are measured from its centre or IP (Interaction Point), which is defined as $(x, y, z) = (0, 0, 0)$. From the IP and looking at ATLAS from the centre of the LHC ring, the positive z -axis is defined as going along the beam-line from right to left, the positive y -axis is pointing upwards towards the surface, and the positive x -axis points towards the centre of the LHC. As with other collider experiments, the spherical coordinate system is used for the event analysis, with the azimuthal angle ϕ measured around the z -axis, with $\phi = 0$ defined by the positive x -axis, and the polar angle θ measured from the z -axis. It is, however, more practical to use pseudorapidity, which is defined as $\eta = -\ln(\tan(\theta/2))$, because differences in η are invariant under a change in reference frame along z . This is useful since $p-p$ collisions are in fact individual parton (quark and gluon) collisions. The sharing of the proton momentum by the partons causes a momentum imbalance such that the detector is not in the CM frame. The constituent partons of $p-p$ collisions will therefore need to be boosted to the CM frame, which is made convenient by the invariant quantity $\Delta\eta$.

1.2.3 Detectors

A brief overview of each detector system is given here. Each detector was designed for a particular purpose and the design choices were based mainly on the physics goals, the radiation environment, and the cost. For further details on each sub-detector, consult the ATLAS TDR [4].

Inner Detector

A very high density of particle tracks is expected near the IP from $p-p$ collisions at the LHC. Detectors which can identify these tracks with high precision are required to make momentum measurements with the resolutions needed by the physics goals. There are three main detector elements that make up the Inner Detector (ID), as shown in Fig. 1.4. These include pixel and microstrip (SCT) semiconductor tracking detectors, as well as a transition radiation tracker (TRT). The semiconductor segments provide the necessary granularity as close to the IP as possible, but the number of layers is restricted because of their high cost

and the amount of material they introduce, which causes multiple scattering and increases the number of secondary particles reaching the calorimeters. The main purpose of the pixel detectors is to provide very high granularity and precision measurements of the particle tracks near the IP, with efficient handling of information for triggering purposes. Along with the pixels, the microstrip layers, made up of silicon wafers, are designed to provide additional precision measurements per track, but in the intermediate radial range where the granularity can be reduced to save on cost. In addition to yielding good pattern recognition, the silicon microstrips contribute to the measurement of momentum, impact parameter, and vertex position. The pixels provide three spatial points per particle track, whereas the strips yield four measurements per track. Further away from the IP, the TRT completes the track reconstruction with the use of its narrow straw tube detectors, but also provides electron identification through the detection of transition-radiation photons. The latter are produced by highly relativistic particles traversing the boundary between materials with different indices of refraction. A xenon based gas mixture both absorbs the transition-radiated photons and detects the original radiating particle through ionization. Altogether, these three sub-detectors provide precise and efficient track reconstruction near the IP, for a pseudorapidity region of $-2.5 < \eta < 2.5$ with both a barrel region around the IP and an endcap at each end. All of these inner detector components are placed within a 2 T magnetic field provided by the central solenoid (CS) superconducting magnet, which deflects charged particle tracks for measuring momentum.

Calorimeters

The calorimeters in ATLAS will provide energy measurements with good resolution for electrons, photons, and jets of hadrons. Missing transverse energy, \cancel{E}_T , is the amount of energy in the plane transverse to the $p - p$ collision axis that is not accounted for, due to undetected particles. It is therefore a signature of many interesting particle interactions and accounting for all the energy from a given collision is crucial for physics studies. As a result, the ATLAS calorimeters were designed to cover as much angular region as possible. An outline of the ATLAS calorimetry system is shown in Fig. 1.5. The calorimeters consist of a barrel, centred around the IP, and endcap sections located at each end. The electromagnetic (EM) calorimeter is a lead/liquid-argon (LAr) detector employing an accordion geometry which ensures complete symmetry in ϕ and leaves no azimuthal cracks. There are both a barrel (EMB) section and two endcap (EMEC) sections with such a configuration. In both

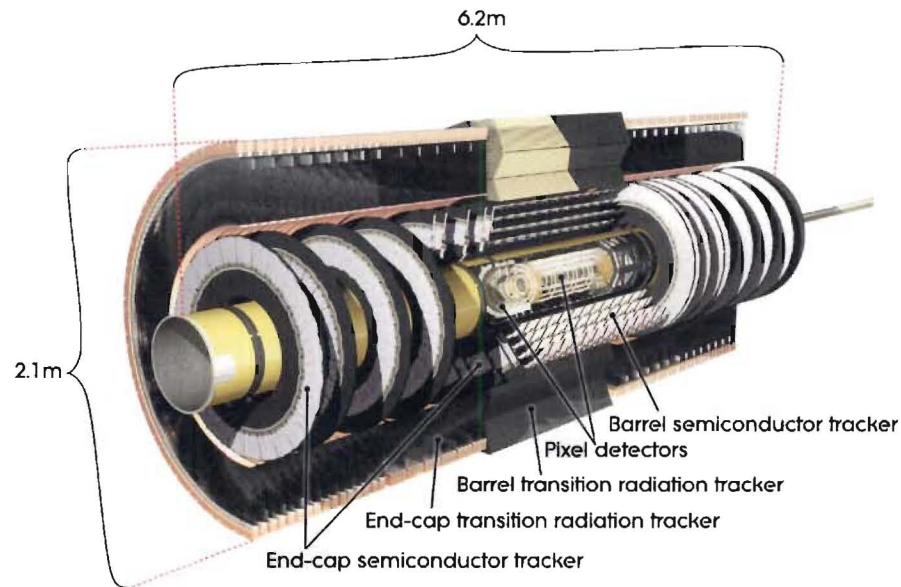


Figure 1.4: The ATLAS Inner Detector [5].

cases, a narrow radial region called a preshower detector enhances particle identification and yields precise measurements of position in η . At larger pseudorapidities where there is higher radiation, LAr is also used for the calorimeters because of its intrinsic resistance to radiation. In the endcaps, there are hadronic calorimeters (HEC), which use a more conventional geometry of parallel plates made of copper, and forward calorimeters (FCAL), which use a rather novel electrode structure wherein copper or tungsten tubes are set into a copper or tungsten matrix. Both the HEC and FCAL were designed to be able to provide good energy resolution for high energy jets and remain radiation-hard. Further away from the IP, another hadronic calorimeter surrounds the EM barrel and also extends over the endcaps. This is the Tile calorimeter, so called due to its composition of iron and scintillating tiles. Signals produced in the scintillating tiles and the photomultiplier tubes (PMTs) are very fast. All the hadronic calorimeters were designed to provide good energy resolution without affecting too much the muons escaping into the outer spectrometers. The sections in the positive z direction are referred to as the A-side while the sections in the negative z direction are called the C-side. Further details of the ATLAS calorimeter systems are given in the next chapter.

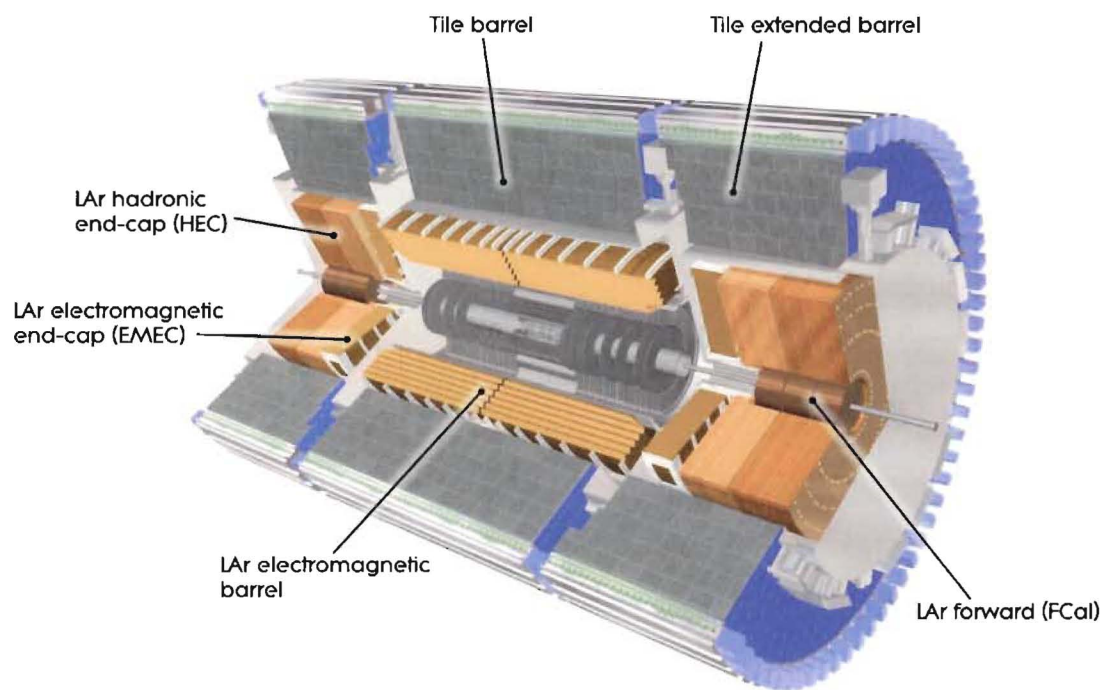


Figure 1.5: The ATLAS LAr and Tile calorimeters [5].

Muon Spectrometer

High energy muons are key signatures of several interesting physics processes at the LHC. ATLAS was therefore designed to include high resolution muon spectrometers with wide angular coverage and the capability to operate independently of other detector components. A main ingredient to the operation of the ATLAS muon system is the large superconducting air-core toroid magnet system that deflects the muon tracks. This includes a barrel toroid and two endcap toroids, which depending on the pseudorapidity range, bend the muons on their own or combine to do so. In the bending direction of the magnetic field, measurement of the muon track position is provided by Monitored Drift Tubes (MDTs), whereas Cathode Strip Chambers (CSCs) are used in regions with high radiation, located at large η values, because of their finer granularity. The Resistive Plate Chambers (RPCs) in the barrel region and the Thin Gap Chambers (TGCs) in the endcaps serve as the trigger chambers, which have a better time resolution than the 25 ns bunch spacing of the LHC. All four types of muon detectors are designed for a particular purpose, but they all read out signals based on drifted ions caused by muons ionizing a gas mixture. The layout of the muon spectrometers is given in Fig. 1.6.

1.2.4 ATLAS Software

All of the aforementioned detector systems will provide signals which need to be converted to physical measurements, such as energy or momentum, through a process called event reconstruction. This is true of both data from real collisions as well as Monte-Carlo (MC) simulations. The Athena framework is the main piece of ATLAS software which was implemented to perform not only reconstruction, but the “full-chain” described in Fig 1.7. For simulation of the experiment, event generation is typically performed by standalone programs such as Pythia through an Athena interface. This process produces an event record called HepMC, which contains the event’s information such as particle ID and vertices, and is used as the input for simulation. Geant4 is currently used to simulate the energy deposition by particles within a given detector, referred to as G4 Hits. Digitization, with or without the inclusion of electronics noise, mimics the digital signals that would be produced if the events were real, producing G4 Digits. The reconstruction is therefore the same for both real and simulated data. The many conversion factors, particularly for reconstruction, are stored in databases that are accessed when running an Athena reconstruction job. Athena itself

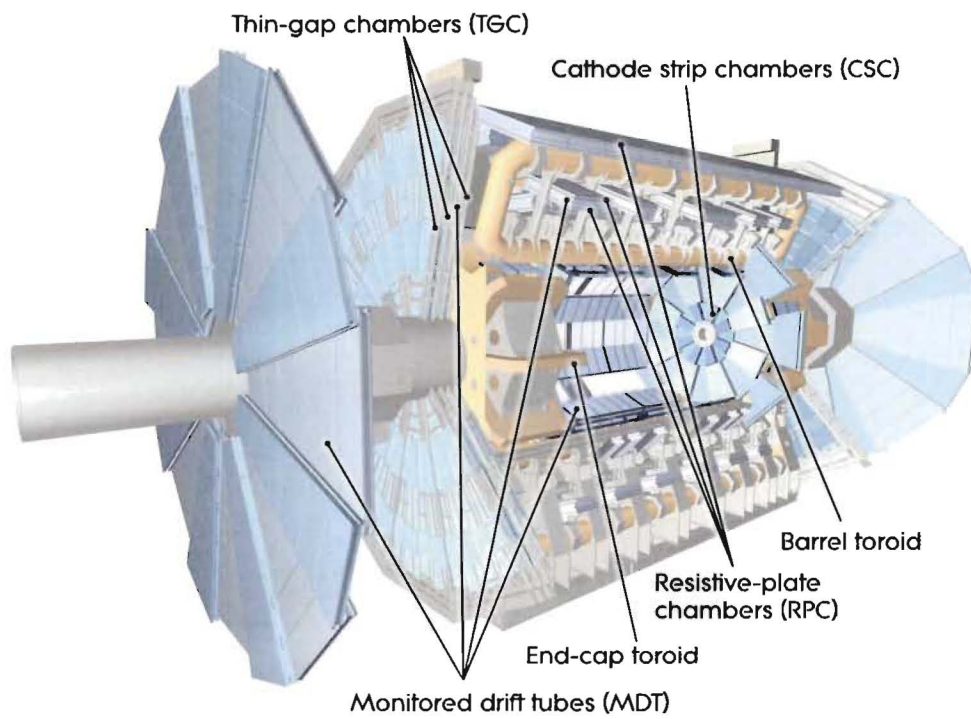


Figure 1.6: The ATLAS muon spectrometers [5].

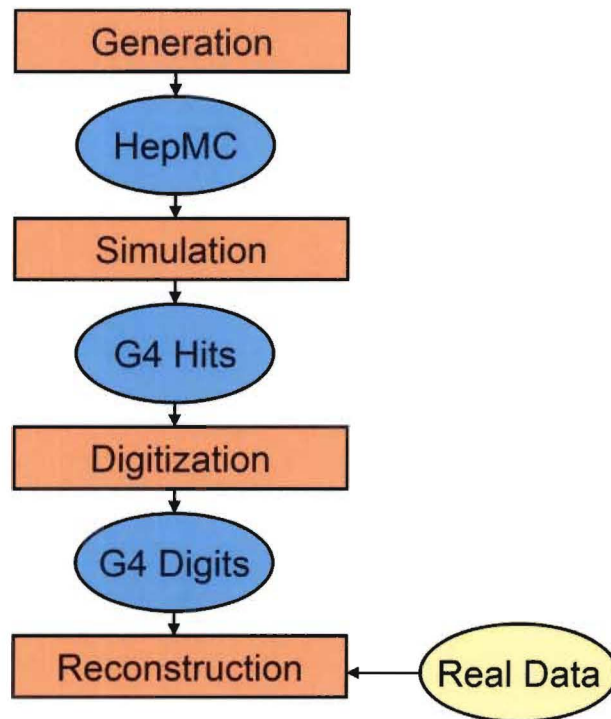


Figure 1.7: A flow diagram of the full chain of Monte-Carlo production using ATLAS software.

consists of many software packages related to a particular process, such as digitization or reconstruction. These packages are constantly being updated as analysis of MC, test-beam, and commissioning data continues. With each major Athena software release, there are also typically new geometries representing, for example, test-beam or cosmic ray commissioning. For this work, Athena releases 11.0.41 and 12.0.1 were used for the full-chain analysis, while various versions of release 12 and release 13.0.10 were used for reconstruction.

Chapter 2

Calorimetry and the ATLAS Calorimeters

Measuring energy is an important part of any particle physics experiment. Calorimeters measure the energy deposited by particles. This information can be used to identify particle types. In this chapter, the processes by which calorimeters measure energy are explained, followed by an overview of the ATLAS calorimetry system, including the types and purposes of each calorimeter.

2.1 Calorimetry

Calorimeters are designed such that incident particles deposit their energy within the calorimeter material, predominantly through the creation of particle showers whose energies are absorbed and measured. These particle showers are either entirely contained within the sensitive volume of the calorimeter, called homogeneous calorimeters, or their energy is sampled in many stages, leading to an estimate of the total shower energy. The latter are referred to as sampling calorimeters. Because of the high cost of materials required for homogeneous calorimeters, the sampling type was chosen for ATLAS [4]. An interesting property of calorimeters is that the energy resolution increases with increasing particle energy, whereas in particle tracking detectors using magnetic fields, the opposite is true. Because calorimeters use the interaction of the incident particles with material to measure the energy, all particles are detected, including electrically neutral ones with the exception

of neutrinos. Different calorimeter designs are used for particles interacting via electromagnetic processes and for particles which produce hadronic showers. Each calorimeter is typically optimized to measure particles produced by one type of shower.

2.1.1 Particle Interactions

Particles interact with the calorimeter material via an electromagnetic or hadronic process, depending on the incident particle. For electromagnetic interactions, there are several methods by which the incoming particle will release energy. All charged particles can lose energy through the ionization of surrounding atoms or molecules and at higher energies, through bremsstrahlung¹, particularly for lighter particles, such as electrons and positrons. A critical energy, E_c , is defined as the energy at which the energy loss through ionization for electrons and positrons equals the loss via bremsstrahlung. The latter process produces photons, which also interact electromagnetically. There are three main processes by which photons can lose energy; the photoelectric effect, Compton scattering, and pair production. In Figure 2.1, the contribution from each of these processes to the total cross-section for photon interactions in lead is shown. In the photoelectric effect, an incident photon is absorbed by an atom, which becomes excited and consequently ejects an electron. This process is dominant for low energy photons. Compton scattering involves the scattering of a photon from an atomic electron and for a large range in energy, is the most probable method for a photon to lose its energy, as seen in Figure 2.1. At higher energies, the dominant method of interaction is via pair production. In this process, a photon with energy greater than $2m_e c^2$ can decay into an electron-positron pair, with a nearby atomic nucleus or electron serving to conserve momentum.

The interaction of hadrons, such as pions (π 's) and kaons (K's), with material is more complicated. Although charged hadrons will lose energy through ionization, at energies in the MeV range and beyond it is also possible that they will interact via the strong nuclear force, which is also the only method of interaction for neutral hadrons such as neutrons. Through this nuclear interaction, a hadron interacts with an atomic nucleus, which can emit a number of other hadrons in a process referred to as nuclear spallation.

A quantity $\langle dE/dx \rangle$ called the ionization density or specific ionization is defined, which measures the average energy loss through ionization per unit length of material. All charged

¹Radiation caused by charged particles decelerating after being deflected by other charged particles.

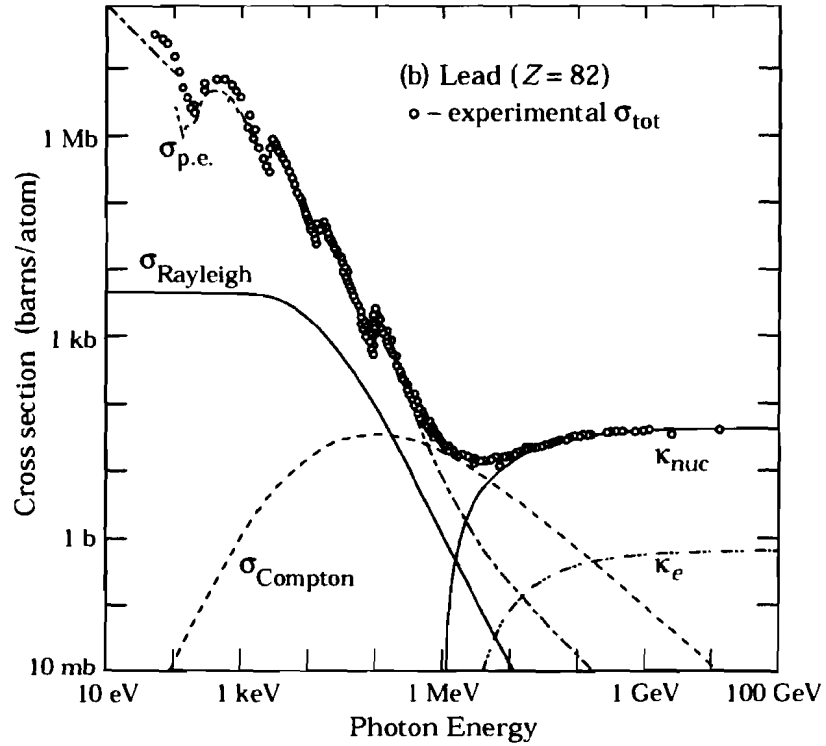


Figure 2.1: Contributions to the photon interaction cross-section in lead. The relevant symbols here are $\sigma_{p.e}$ (Photoelectric effect), σ_{Compton} (Compton scattering), σ_{Rayleigh} (Rayleigh Scattering), and κ_{nuc} or κ_e (Pair production off the nucleus or electron). This figure is taken from [6].

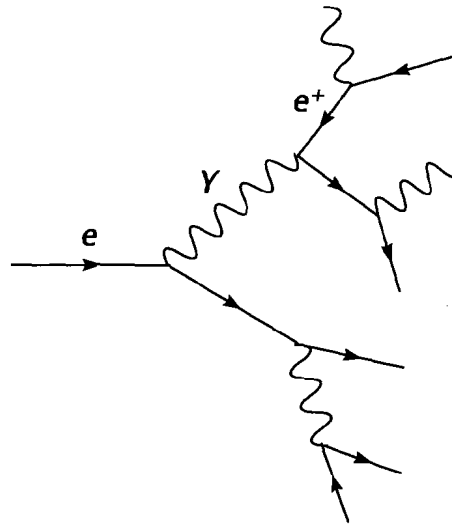


Figure 2.2: An example of an electromagnetic shower initiated by an electron.

particles follow a particular trend with respect to their energy based on their properties, such as mass and velocity, and the properties of the material they are traversing. This $\langle dE/dx \rangle$ function has a minimum and particles with an energy that corresponds to this minimum ionization region are referred to as minimum ionizing particles, or *mips*. In LAr, for example, *mips* lose 2.13 MeV per cm on average.

2.1.2 Particle Showers

Based on the electromagnetic interactions described above, it is easy to see how an electromagnetic shower of particles can be produced. High energy electrons (or positrons) will predominantly produce photons through bremsstrahlung, and the corresponding high energy photons will mostly pair produce electrons and positrons, which will continue the trend of producing more and more electromagnetically interacting particles. A simplified example of an electromagnetic shower is shown in Figure 2.2. The shower will continue until the energy falls below E_c , at which point the particles will lose their energy mainly through ionization.

Hadronic showers are produced in a similar way, but with different particle interactions involved. Through nuclear reactions, a hadron that strikes a nucleus may produce new hadrons [7]. The energy and number of particles increases until at some depth the shower

particles are absorbed and the particle multiplication decreases. On average, approximately 1/3 of the particles produced in the first hadronic interaction are electromagnetic, predominately due to the decay of neutral pions ($\pi^0 \rightarrow \gamma\gamma$). All hadronic showers, therefore, contain an electromagnetic component.

2.1.3 Sampling Calorimeters

In a sampling calorimeter, one material is used for shower development while another component is used to measure the shower energy. The former is called the passive medium and the latter is the active medium. A large array of sandwiched passive and active materials makes many separate measurements of the shower, sampling the shower energy each time. Typically, a high-density material such as lead is used for the passive medium whereas the active medium requires a material capable of producing a signal, usually through light generation or the formation of ions. In the ATLAS calorimeters, LAr and scintillating plastic are used for the active medium material. For LAr, the charged particles produced in the shower ionize the argon, leaving electron-ion pairs. An applied electric field directs the electrons to a positive voltage terminal, inducing a current proportional to the energy deposited. An example of a particle entering a LAr calorimeter is shown in Figure 2.3. In the case of scintillating plastic, charged particles excite the molecules which emit photons that propagate to PMTs². The signal induced by the photons is proportional to the energy deposited. The drift time of a LAr detector is usually several hundred nanoseconds, whereas the signal from a PMT is much faster. Reasons for the choices of each type of material are given in the sections below. In this sampling technique, the energy resolution actually improves with the incident particle energy. This is because higher energy corresponds to more particles in the shower and hence the sampling fluctuations are reduced leading to a more accurate measurement of the energy.

2.2 The ATLAS Calorimeters

The design and operation of the calorimetry system are now presented in detail.

²Refer to Section 1.2.3

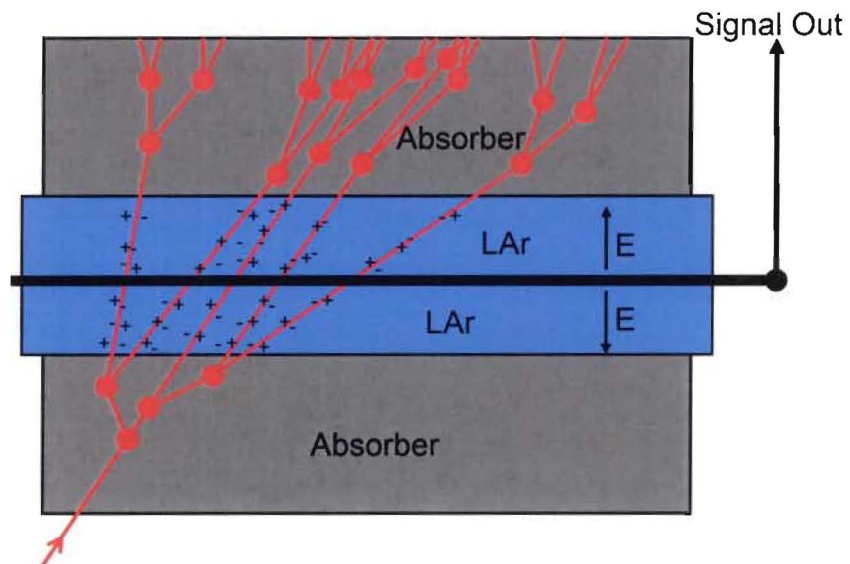


Figure 2.3: A simplified example of one layer of a LAr/absorber sampling calorimeter. Here a particle initiates a shower within the absorber and the charged particles ionize the LAr, inducing a current in the readout electrode.

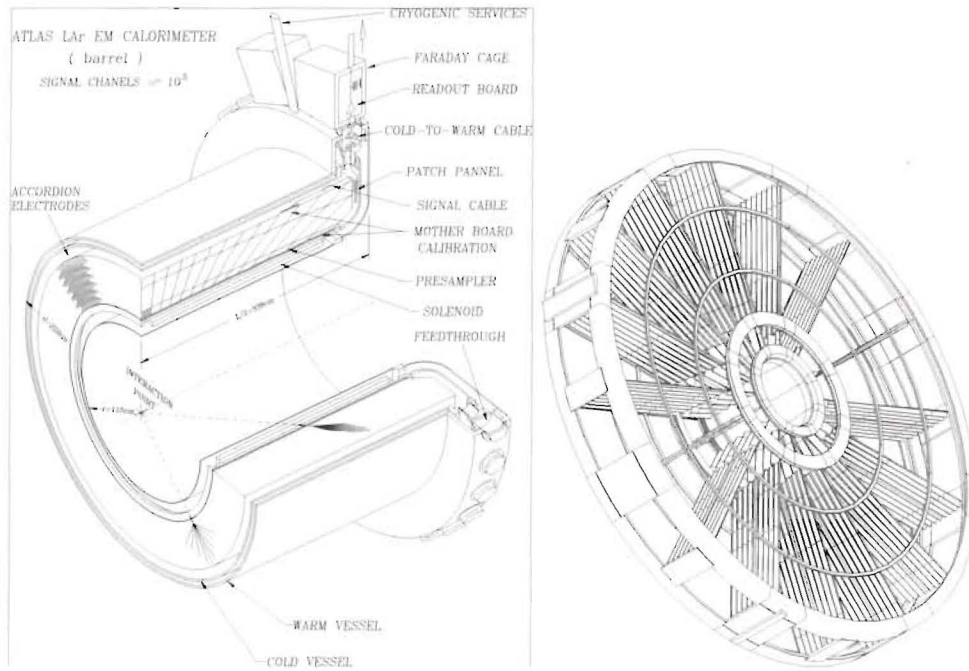


Figure 2.4: A cut out of the EM barrel calorimeter (left) and the EMEC inner and outer wheels showing the accordion structure (right) [4].

2.2.1 Electromagnetic Barrel (EMB) and End-Cap (EMEC) Calorimeters

The EMB covers the pseudo-rapidity region of $|\eta| < 1.475$ and the EMEC covers $1.375 < |\eta| < 3.2$, which is broken down into an inner ($1.375 < |\eta| < 2.5$) and an outer ($2.5 < |\eta| < 3.2$) wheel. An accordion geometry in both calorimeters ensures full azimuthal coverage ($0 < \phi < 2\pi$) with no dead regions. Both the EMB and EMEC use lead as the absorber to generate the electromagnetic showers and LAr as the active material, which is kept at 87 K within a cryostat. For mechanical reasons, stainless steel covers the lead absorber plates, whose thickness varies to optimize the energy resolution. In the barrel, the LAr gap is constant at 2.1 mm, whereas in the endcap the gap thickness increases with radius since the absorbers remain at a constant thickness but the height of the accordion waves increases with radius. Copper sandwiched with Kapton insulators forms the electrodes between LAr gaps. The electrodes distribute the high voltage (HV) that allows the electrons to drift and induce the current which is read out.

The barrel and endcaps are each divided into three longitudinal sampling layers. The first

sampling is called the strip or front section and provides precision position measurements. Sampling 2, or the middle layer, contains most of the electromagnetic shower energy and is divided into square towers with a granularity of $\Delta\eta \times \Delta\phi = 0.025 \times 0.025$ in the EMB and the EMEC inner wheel. The third sampling, or back section, helps in the separation between hadronic and electromagnetic showers. The granularity in the barrel for these various samplings is shown in Figure 2.5. A presampler section also exists in both the EMB and EMEC to detect the energy of showers initiated by material in front of the electromagnetic calorimeters, such as the inner detector, cryostat, and solenoid coils. Cells are made up of 3 consecutive planes covering 0.025 radians in ϕ and are formed such that they are pointing towards the IP in both η and ϕ .

There are around 170,000 electronic channels that read out the signals from the EM calorimeter cells. The electronic signals are sent to the channels via cables through the cryostat feedthroughs.

2.2.2 Hadronic End-Cap (HEC) Calorimeter

Housed within the same cryostat as the EMEC, the HEC also uses LAr as the active material, but uses copper plates as the absorbers, in a more conventional geometry than the accordion structure of the EMB and EMEC. There are two independent wheels of each HEC, covering the range of $1.5 < |\eta| < 3.2$. A partially assembled HEC wheel is pictured in Figure 2.7. The two wheel copper plate design was chosen mainly for resistance to radiation and cost effectiveness, while still providing the necessary coverage. Each wheel consists of 32 identical modules. A module consists of 24 copper plates for the front wheel and 16 plates for the rear wheel. In all cases, the copper plates are separated by an 8.5 mm LAr gap that contains three electrodes. There are therefore four LAr gaps between each pair of copper plates. The outer electrodes carry the HV while the central electrode provides the signal readout. A cross sectional view of a HEC read-out structure in the inter-plate gap is shown in Figure 2.8. The four gaps limit both the HV required per gap and the pile-up of ions, while providing redundancy if there is a failure in one gap.

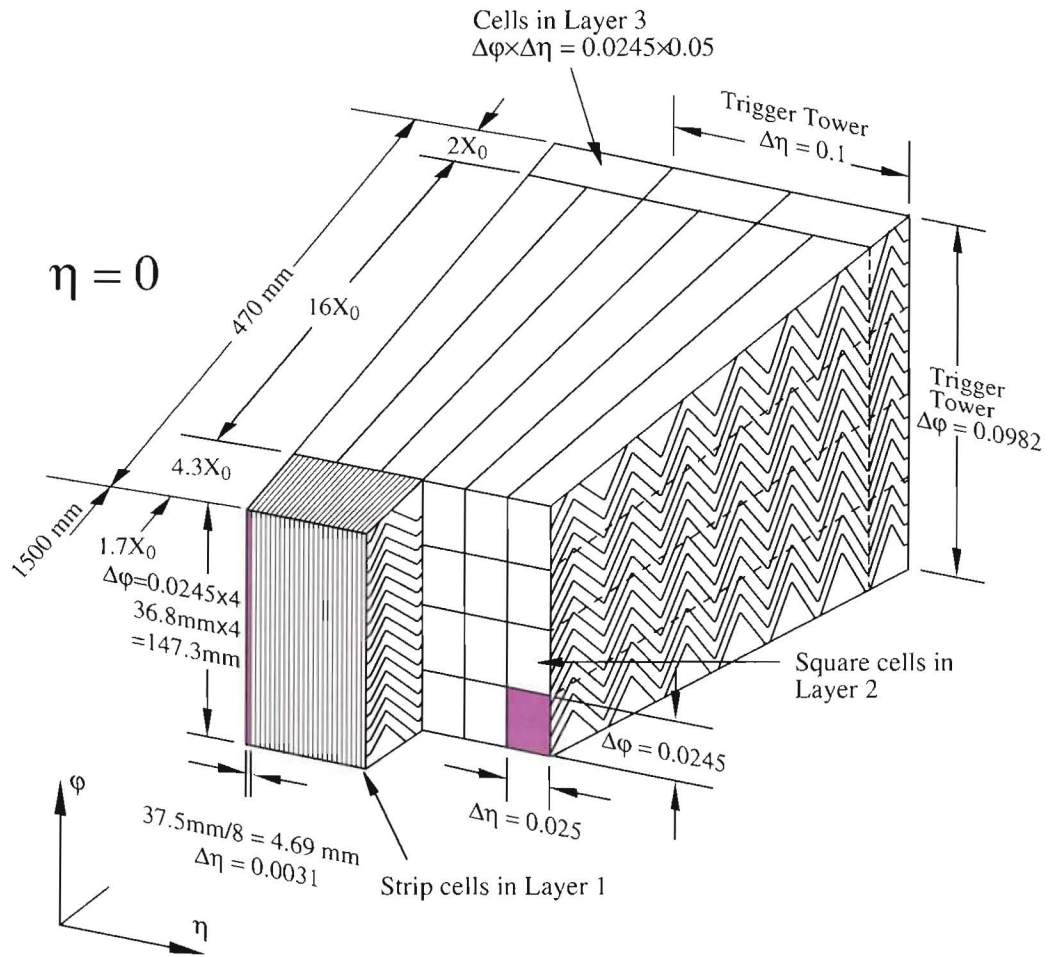


Figure 2.5: A view of the granularity of the different segments of the EM barrel [4].

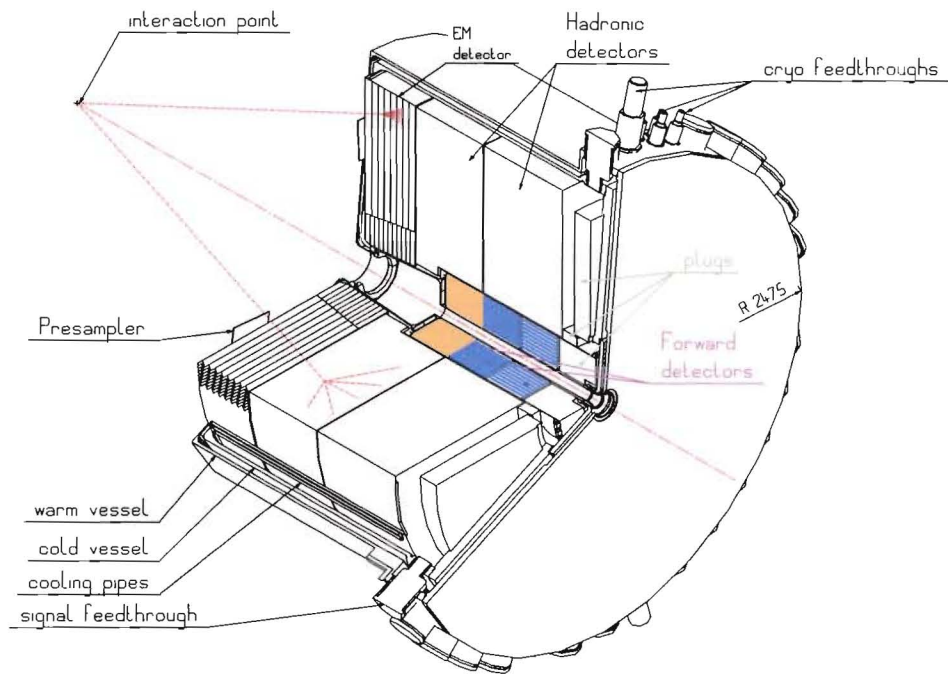


Figure 2.6: A cut out of the EM endcap calorimeter (EMEC) [4].

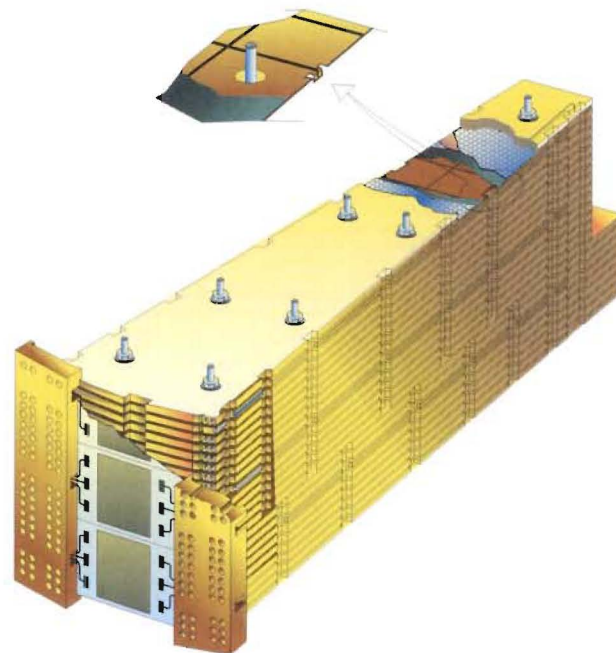


Figure 2.7: A HEC module showing a cutaway of the read-out structure [1].

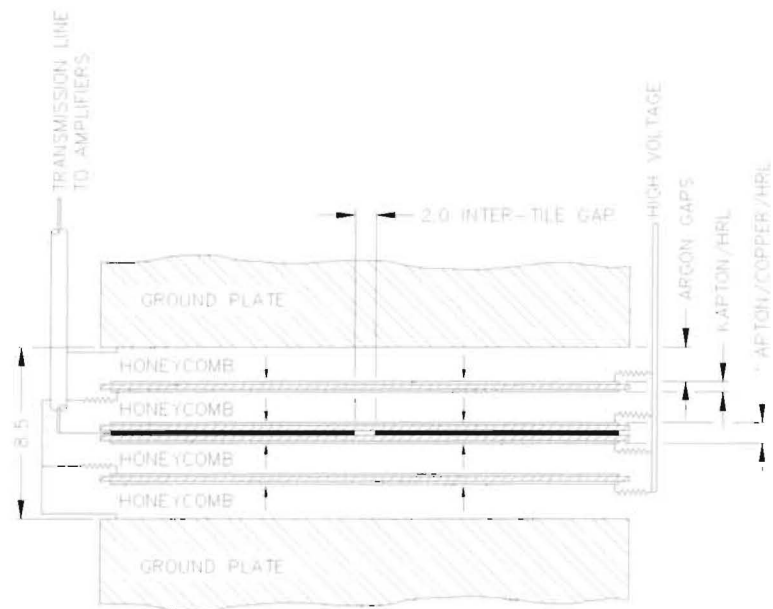


Figure 2.8: A cut out view of the four LAr gaps and readout electrode structure contained between two copper plates in the HEC [4].

2.2.3 Forward Calorimeter (FCAL)

Another calorimeter section within each endcap cryostat is the FCAL, which also employs LAr. It covers the region $3.1 < |\eta| < 4.9$. The design was chosen to meet specific requirements for resisting radiation because of the high radiation environment close to the beamline. The FCAL consists of an EM module using copper and two hadronic modules which use tungsten for the absorbing material. Because of the large ion buildup in this forward region, it is necessary for the LAr gaps to be as small as possible. As a result, each FCAL module makes use of a metal absorber matrix (See Figure 2.9) made of copper or tungsten, depending on the module. This matrix contains equally spaced holes that contain a copper tube that acts as ground, within which a rod, made of the same material as the matrix body, is inserted and supplies the HV. The small annular gap between the rod and tube contains the LAr. This gap size ranges from $250 \mu\text{m}$ for the EM module to 375 and $500 \mu\text{m}$ for the two hadronic modules. These design choices were meant to achieve good shower containment with high density material while maintaining uniformity in the angular coverage.

2.2.4 Hadronic Tile Calorimeter

Located just outside of the LAr calorimeters in the barrel region, the Tile calorimeter is yet another sampling calorimeter. Due mainly to costs and relaxed radiation considerations, it uses scintillating plastic tiles as the active material and iron plates as the absorbers. There is a main barrel section covering the region $|\eta| < 1.0$ and two extended barrel sections that cover the region $0.8 < |\eta| < 1.7$. In between the barrel and each extended barrel section is a 68 cm gap that provides space for service cables and electronics for the ID and the LAr calorimeters. Within this gap there exists an extension to the extended barrel, called the ITC (Intermediate Tile Calorimeter). The ITC consists mainly of scintillators, referred to as gap and crack scintillators, which primarily sample hadronic and electromagnetic showers, respectively. In the Tile calorimeter, the 3 mm thick scintillating tiles are staggered vertically within an iron absorber, as shown in Figure 2.10. Two independent PMTs read out the fast signals produced by the scintillating tiles from two sides using WLS (Wavelength shifting) fibers. The current produced by the PMT is transformed by a shaper into a 50 ns wide pulse. Readout cells are grouped together with granularity $\Delta\eta \times \Delta\phi = 0.1 \times 0.1$ to be pseudo-projective towards the IP.

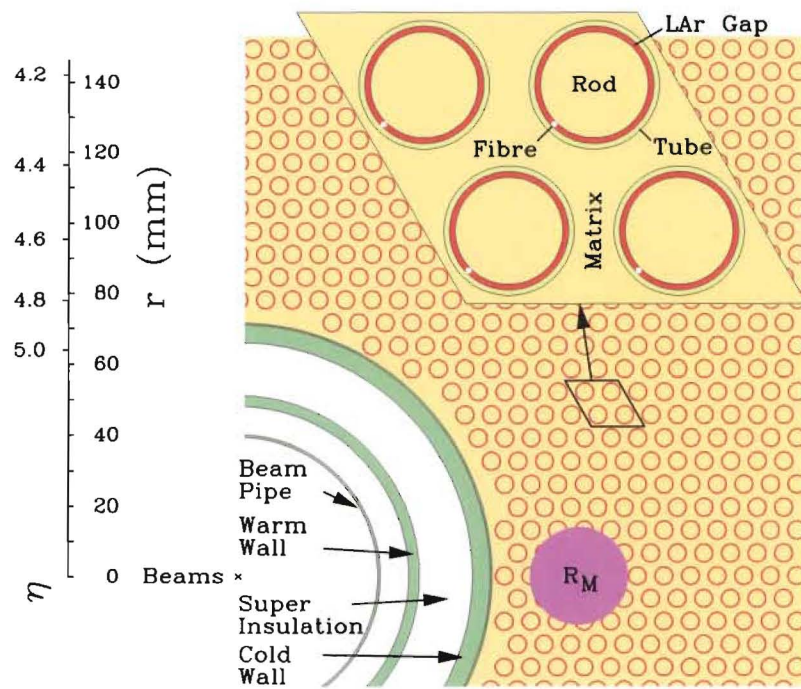


Figure 2.9: An image showing the FCAL matrix employing rods and tubes [4].

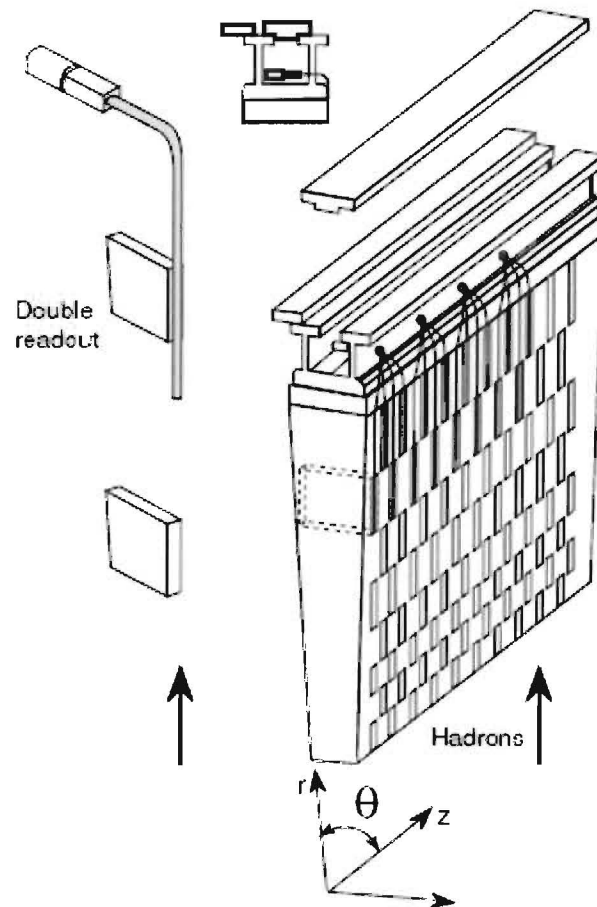


Figure 2.10: A module of the Tile calorimeter consisting of vertical scintillating plastic tiles in an iron absorber [4].

Chapter 3

Calorimeter Commissioning

There are quite a few steps involved in commissioning a detector the size of ATLAS. Commissioning with $p - p$ collisions is beyond the scope of this work. In this thesis, the term commissioning is restricted to the process of getting the detector to a state of readiness for first beam. Here we discuss the commissioning phases for the LAr calorimeter, including front-end electronics testing during both warm and cold stages and data taking with cosmic rays, which is the main focus of this work.

3.1 Purpose

Prior to taking data from $p - p$ collisions, it is important to understand completely the response of the calorimeters, because reconstructing all of the energy deposited by particles for any given event is crucial to all physics studies. Missing energy, for example, is one of the most important signatures of many interesting new physics processes. This is the undetected energy signalled by a momentum imbalance between outgoing particles after a collision, usually caused by a particle escaping the detector without being detected. But mismeasurement of the energy can also lead to an apparent missing energy, so one needs to measure accurately all of the energy deposited in the calorimeter. Therefore, each calorimeter cell must be well understood. To reach this level of confidence in the detector readout, we perform several phases of calorimeter commissioning.

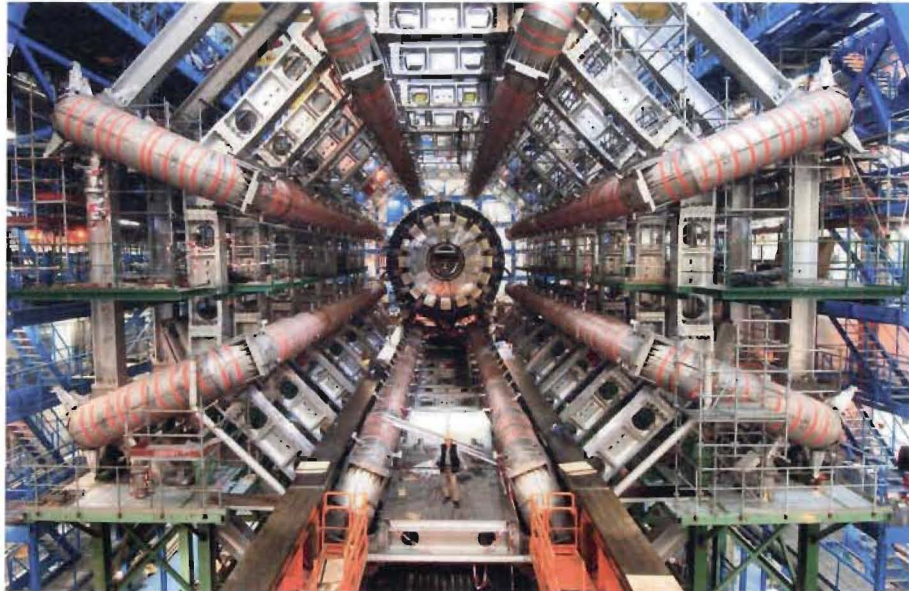


Figure 3.1: A picture taken after installation of the LAr barrel calorimeter (centre), surrounded here by the magnetic toroids, before being moved into position in Nov. 2005. Soon after, the front-end electronics were tested.

3.2 Commissioning Phases

The commissioning of the calorimeters was broken down into three phases [8], with the first two referring primarily to the installation and integration of the readout electronics. Phase three comprises the testing and initial operation of each detector component. This is the work discussed here.

Phase three itself is divided into several stages of testing and operation. These include testing of each electronic channel both prior to cooling of the detector with LAr and afterward. In addition, data are taken with cosmic rays, and later from beam gas and beam halo events during the initial single beam running. The first of these stages is referred to here as Warm/Cold Commissioning, as it deals with the electronics response at room temperature (Warm) and subsequently after cooling down to the LAr temperature of 87 K (Cold). All problematic electronic channels and other issues, such as faulty electronic boards and problems related to cabling, are documented during the warm testing phase and are re-tested

during the cold phase. The purpose of this stage is to identify problems in the front-end electronics and if needed, determine solutions such as replacing components. The results of the electronics calibration runs are also used to update the database with measured conversion factors required for reconstructing the signal in each calorimeter cell.

Detection of cosmic ray muons allows for the first detector-wide test with data from real particles, and is also a good opportunity to operate the detectors over a sustained period of time. Not only can it be used to check the electronics as with the warm/cold testing, but the actual ionization of the LAr allows for a check of the energy calibration of the calorimeter. This includes checking the calibration constants being used to reconstruct cosmic ray energies and the timing of the signals used for the reconstruction. It is important to determine, for example, any timing offsets between various subdetectors and whether the energy reconstructed is as expected.

Beam gas events occur when the proton beam scatters off residual gas particles in the beam line, as it is not a perfect vacuum. There is a plan to study these events during single beam running. These events are ideal for studying the barrel section because they produce particles with roughly the same trajectories as for $p - p$ collisions. Beam halo events are mainly caused by the beam focusing elements, which produce a halo of particles around the focused beam as it passes through a narrower region. This halo is ideal to study the endcap regions since the particles travel parallel to the beamline. Beam gas and beam halo events have been simulated [9], but are not discussed further in this work.

3.2.1 Warm/Cold Commissioning

This commissioning stage refers to the testing of all the front-end electronics, which convert the ionization within a calorimeter cell to a signal that is proportional to the energy deposited in that particular cell. As there are no actual particles in this stage, signals are created by sending a calibration pulse through the entire front-end electronic system, which effectively mimics a signal created by ionization of the LAr.

There are several types of runs taken during this commissioning stage which check the signal through each electronic channel. These include pedestal, delay, ramp, and to a lesser extent single DAC¹ runs. Pedestal runs check the level of noise in each channel by looking

¹Digital to Analog Converter

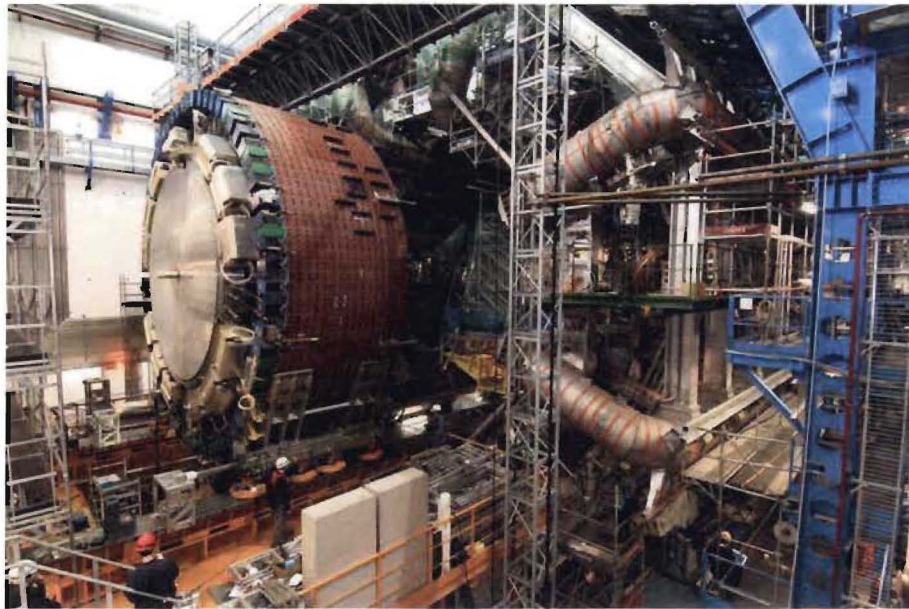


Figure 3.2: A LAr endcap was installed in spring 2006. Shortly after, each electronic crate was connected and electronics calibration runs were performed for each electronic channel.

at the ADC² value with no injected signal and its RMS (Root Mean Square) value. The pedestal is subtracted when there is a real signal. The RMS value gives an indication of the size of the noise for a particular channel. Delay runs measure the pulse shape as a function of time for each channel. This is useful in checking that the pulse shape is nominal and that it does not occur too late or early with respect to other channels. In delay runs, signals are injected at times varying by 1 ns over the whole readout range. The ramp determines the corresponding ADC value for an input DAC value. This is used in the conversion step from raw data to energy. Its stability over time is a quantity that is monitored routinely. Runs are taken in all three gain regimes of the calorimeter: High, Medium, and Low.

Through the monitoring of these electronics calibration runs, dead or noisy channels are discovered and documented, and larger problems such as faulty FEBs (Front-End Boards) are investigated. As a result, all front-end electronics issues are well understood prior to data taking with real particles.

3.2.2 Commissioning with Cosmic Ray Muons

Cosmic ray muons are the first events to occur in ATLAS, prior to collisions, that will allow for testing of the detector as a whole with real particles. In the calorimeters, we can analyze the energy deposition and timing of these cosmic ray events using the sub-detectors together for the first time. The focus here is on cosmic rays within the LAr calorimeters. The calorimeters were designed to detect particles coming from collisions occurring at the IP. These are called projective events, such that the closer a particle's trajectory is through the IP, the more projective it is. Cosmic rays, however, do not necessarily pass through or even near the IP, making them predominantly non-projective events. There is therefore a challenge in detecting non-projective events in a detector designed for projective ones. In the LAr barrel region, cosmic ray events are predominantly projective and therefore provide a good opportunity to observe the calorimeter working with collision-like events. In the endcaps, however, cosmic rays are almost entirely non-projective, and in fact occur almost vertically, from the top to bottom of each endcap. As a result, much effort has been put into understanding events with these trajectories using Monte-Carlo (MC) simulations (see Fig. 3.3) and into determining methods to identify them correctly within the endcaps, in addition to the barrel. To that end, trigger boards [10] were built and installed on the

²Analog to Digital Converter

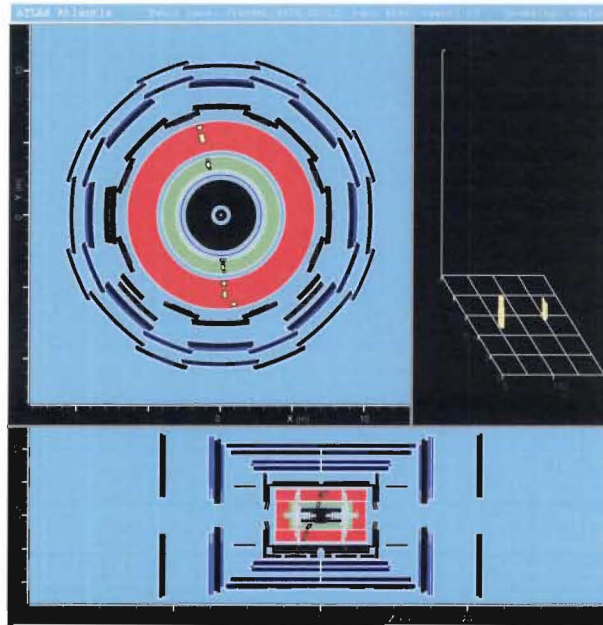


Figure 3.3: A cosmic ray event from Monte-Carlo simulations shown here in the LAr barrel using the Atlantis event display software.

Tile calorimeter barrel and endcap sections on the top and bottom modules, to be used in coincidence with one another as the main trigger for cosmic rays in the LAr. As for the simulations, extensive studies were done using Monte-Carlo generated muons, as well as a full air shower generator, to determine the rates and energies of cosmic muons within the LAr barrel and endcaps.

In order to correctly reconstruct the energy deposited by the cosmic ray generated muons in the calorimeter cells, the timing of the events needs to be well known. Considerable effort was put into using the information from the Tile calorimeter and triggers to predict the timing of the events in the LAr calorimeters. This is particularly important for the non-projective events in the endcaps. From a well-understood timing of cosmic ray events, we can reconstruct the signals left by the muons effectively and perhaps use the energy deposits to perform energy calibrations for the calorimeters.

Apart from any potential calibration of the calorimeter, taking data with cosmic rays is an extremely useful exercise because it also tests the readiness of the process of going from data acquisition to physics analysis. Although the size of the data is small relative to

what is expected from first collisions, it is a good check of the ability of the software and hardware to handle the large sets of data files, access to the databases, and to see how well this process of data taking will proceed.

Chapter 4

Warm/Cold Commissioning of End-Cap Calorimeters

As explained in the previous chapter, Warm and Cold commissioning is a process that mainly checks the response of the electronic readout, which in this case corresponds to the front-end electronics connected to each ATLAS endcap calorimeter. In the following sections, a general description of the layout of the electronics used for this commissioning stage will be given, followed by an analysis of each type of measurement performed. As all of the measurements done when the endcaps were warm (room temperature) were repeated when the calorimeters were cooled to LAr temperature, we will focus here on the warm measurements and only indicate some differences during the cold testing. It is noteworthy that all of these tests were also performed in the EM barrel calorimeter.

4.1 Electronics Layout

The electronics system for reading out signals produced in the LAr calorimeters is complex and a complete description of its design and operation is beyond the scope of this work. Here we will only briefly describe the front-end electronics system of the endcap calorimeters.

Much of the digital electronics are located in a control room far away from the detector. The more sensitive analog electronics, however, are placed on the detector. For each endcap wheel these are placed at the outer ends, in front-end crates (FECs), which are connected to the calorimeter cells via the cold to warm cryostat feedthroughs shown in Figure 4.1.

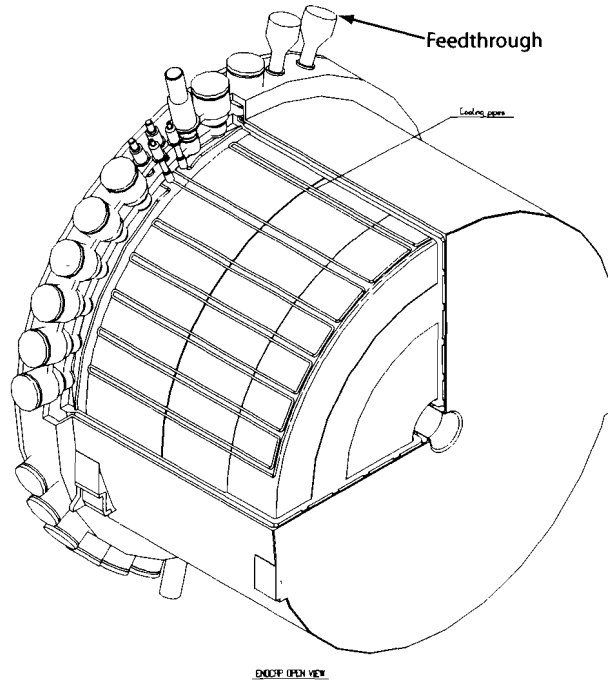


Figure 4.1: An open view of an endcap cryostat showing the cold to warm feedthroughs connecting the calorimeter cells to the front-end electronics [11].

Housed within each FEC are various types of electronics boards used for the signal readout. These include calibration boards used to inject precisely known current pulses to the readout electrodes to simulate energy deposits in the calorimeters and front-end boards (FEBs) which perform most of the immediate signal processing. These will be described in the following section. There are also tower builder boards (TBBs) and control boards which are related to the trigger, and monitoring boards, all of which are not discussed any further here. As shown in Figure 4.2, each FEC is served by two feedthroughs and there are 13 FECs in each endcap. The FECs are broken down into three types: In the region $1.6 < |\eta| < 2.4$, they are called standard EMEC crates, for the inner EMEC wheel and HEC, the cables are connected to special HEC-EMEC crates, and the FCAL has its own FEC. There is a different number of FEBs within each FEC and each FEB holds 128 electronic channels. Each FEC has its own low voltage power supply (LVPS) which supplies the power to the electronic channels. The temperature of these power supplies must be controlled within specified limits.

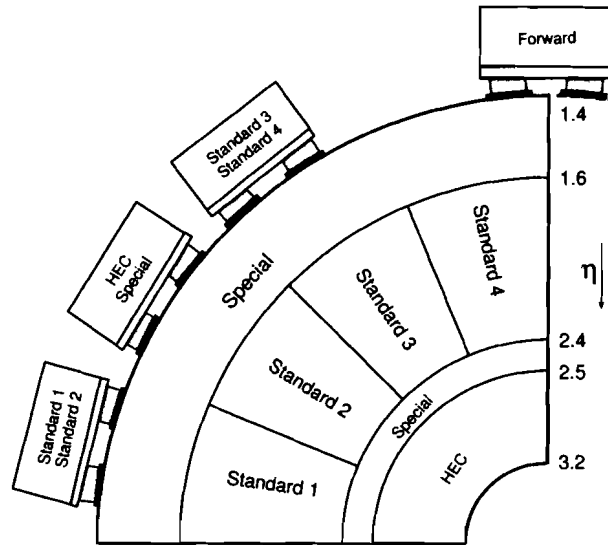


Figure 4.2: The allocation of feedthroughs in the endcaps [11].

4.1.1 Front-End Boards

Each FEB contains the electronics required to amplify, shape, and digitize the signal from the calorimeter, as well as other functions such as sampling and pipelining [11]. The analog signal sent to the FEB is amplified, split into three gain scales, and shaped. Three gain scales are required to extend the dynamic range of the signal without degradation. Four channels are connected to each shaper chip, which applies a bipolar shaping function. The shaped signals are sampled at a 40 MHz rate, corresponding to the LHC bunch crossing frequency. Signals from each channel are digitized via an ADC, which by default digitizes 5 time samples ideally around the signal peak, though up to 32 samples can be digitized to read out the entire signal. There are 8 channels per ADC chip. The digitized signals are stored and sent to Read Out Driver (ROD) modules.

4.2 Calibration Data

Each ROD is responsible for processing the digitized samples from the FEBs and making the processed data available to the DAQ (Data Acquisition System). Calibration runs are

performed through the use of the calibration boards mentioned earlier. The current generated from a calibration board DAC is read by a FEB and processed by a ROD, simulating a physics signal. Shiftworkers can monitor the calibration runs for various issues such as dead, noisy, or distorted channels. As mentioned in the previous chapter, the warm/cold commissioning phase consisted of several types of calibration runs including pedestal, delay, ramp, and single DAC runs. Each of these types of runs will be explained below, with the exception of single DAC runs, which were not used for the majority of the analysis. Each type of calibration run was taken in each of the three gains (high, medium, and low). Monitoring tools were created so that shiftworkers could quickly analyze plots of each type of run and make decisions. The entire warm and cold commissioning data taking period and analysis is documented on the ATLAS wiki [12] and is still ongoing.

4.2.1 Pedestal Runs

The pedestal is the level of ADC counts present when there is no signal. A pedestal run, therefore, is performed by reading out the digitized signal from the FEB, without applying any input from the calibration board, though the LVPS is turned on. The pedestal and the pedestal RMS are checked for each channel. The stability of the pedestal level is usually monitored for a given read-out channel over a long period of time. The pedestal RMS, which is essentially a measure of the pedestal width in ADC counts, is also referred to as the electronic noise. Careful attention is paid to large variations of the RMS between channels, as well as to the stability over time. A large RMS value is a clear indication of a noisy channel, whereas a dead channel is typically identified by a low RMS value. An example of each is given in Figure 4.3. A comparison of the RMS of a warm and cold pedestal run for the same FEB is shown in Figure 4.4. The noise is reduced at LAr temperature, as expected. The pedestal values from the calibration runs are stored in a database called the conditions database, to be used during data analysis. In particular, it is used to subtract the correct pedestal from the signal produced in each calorimeter cell.

4.2.2 Delay Runs

In delay runs, a current pulse is sent at specific time intervals from a calibration board and read by a FEB, over the entire read-out range. In this case the interval was chosen to be 1 ns up to the range of 230 ns. The signal that is read-out is the complete shaped waveform

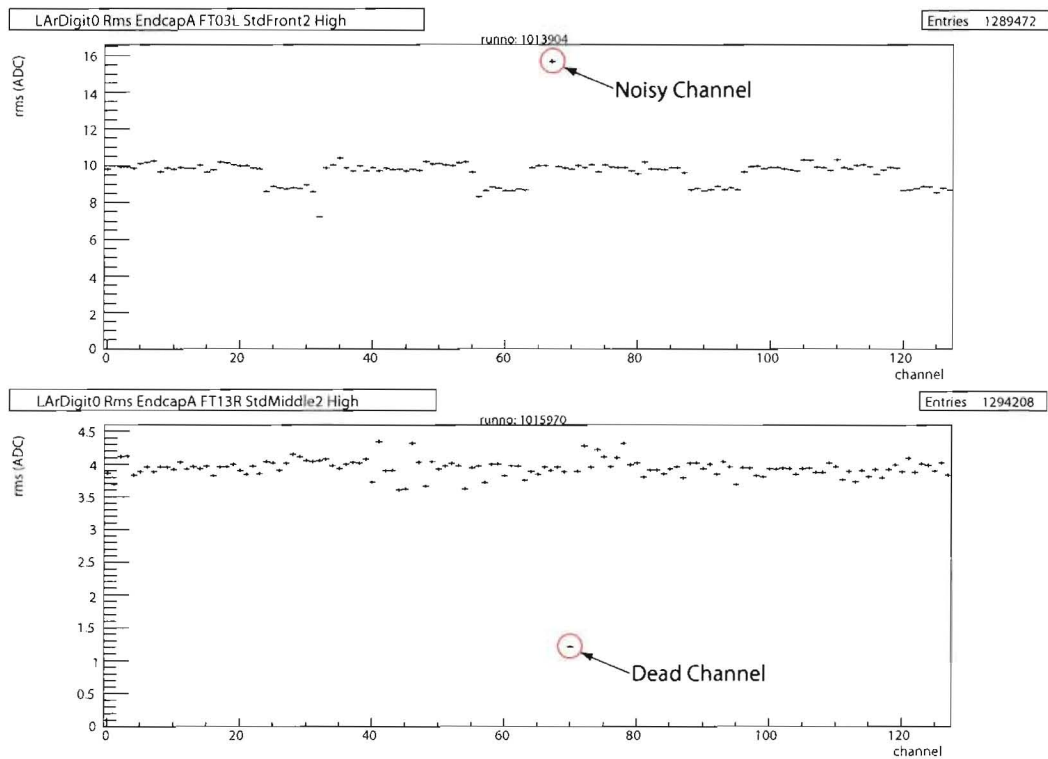


Figure 4.3: Examples of a noisy (top) and dead (bottom) channel found in pedestal runs during warm calibration data taking. If the RMS is significantly higher than the average of all other channels, it is an indication of a noisy channel, whereas a dead channel typically displays a small RMS compared to the average.

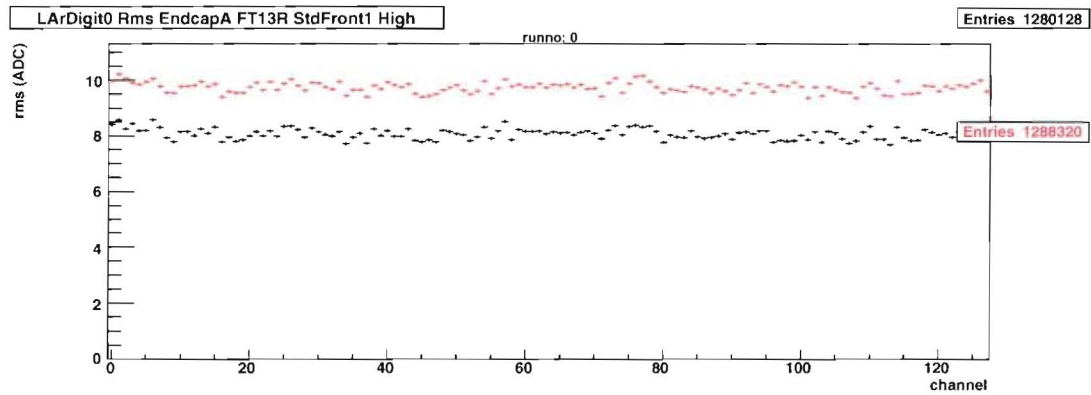


Figure 4.4: A comparison of the pedestal RMS of a warm (red/top) and cold (black/bottom) run for the same FEB. Note that the noise is reduced at LAr temperature.

for a given channel. This signal, which is intended to simulate a physics pulse shape, is used to identify problematic channels and FEBs. Dead channels are clearly identified with a flat or very low amplitude response, whereas channels with distorted waveforms are more difficult to observe. An example of each is given in Figure 4.5. As all of these tests were also performed on the surface prior to installation of the calorimeters in the cavern, many problematic channels were already documented. One main task of the shiftworkers was therefore to check problematic channels against the old results, to see if new problems had arisen. One problem which was found looking at delay runs during warm testing was a fast-shaper problem on some FEBs. As mentioned earlier, four channels are connected to a shaper chip on a FEB, and it was found that for some FEBs the waveform of four channels was narrower and would occur earlier in time in relation to the other channels in that FEB. An example of this effect is shown in Figure 4.5. For the most part, these faulty shapers have been replaced.

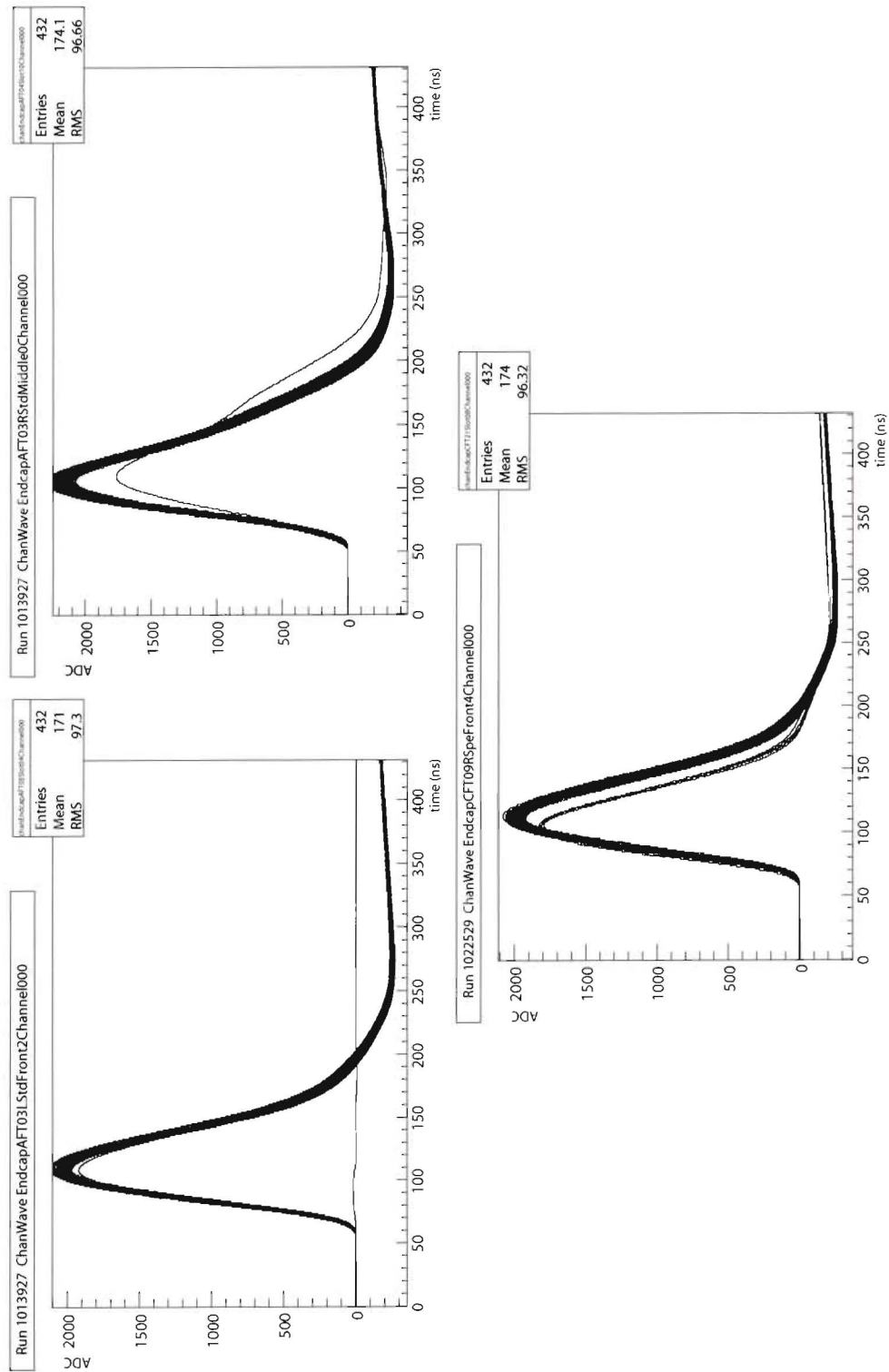


Figure 4.5: Examples of problems found monitoring delay runs. Clockwise from top left: An example of a dead channel, a distorted channel, and a fast-shaper problem on a FEB.

4.2.3 Ramp Runs

The calibration board DAC feeds the FEB an analog signal. The DAC range and interval of measurement are controlled by the calibration run DAQ program. For a given DAC count sent to a particular FEB, the ADC output is referred to as the ramp. The relationship between the DAC input and the output ADC count is measured. It is a linear relationship and therefore its slope and offset are monitored for each channel of each FEB. Its stability over time is also documented. In Figure 4.6, an example is given of two ramp runs, both of which are from FEBs in the same slot of two different standard EMEC crates. It indicated that the cabling of a group of channels for that particular FEB had been changed from the default and the database therefore needed to be updated. The value of the ramp slope and offset are stored in the conditions database to be applied during data analysis.

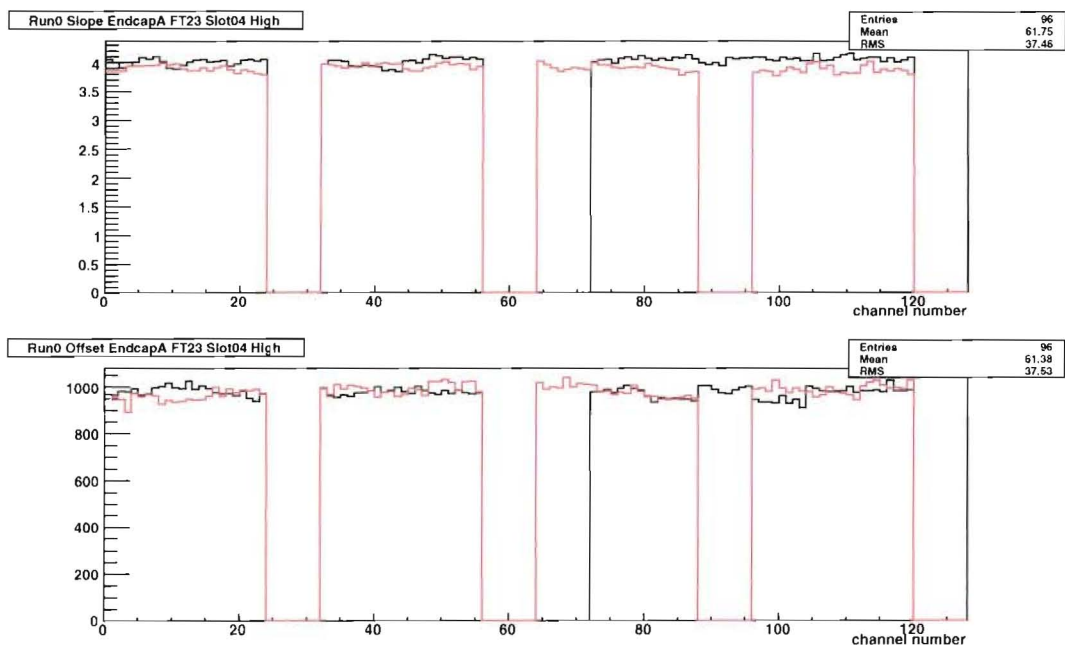


Figure 4.6: An example of a ramp run showing the slope (top) and offset (bottom) of the DAC to ADC linear relationship. A comparison with a reference run (red) indicated that, in this particular case, the cabling of a group of channels in a FEB (black) had changed from the default (red).

Chapter 5

Monte-Carlo Simulation of Cosmic Rays

Commissioning with cosmic rays is the first opportunity to run the full detector with real physics data prior to collisions from the LHC. For the calorimeters, it is therefore an important step in the testing and validation of calibration values. It is also an opportunity to operate the calorimeter systems together for the first time. Prior to cosmic ray data-taking in the calorimeters however, a great deal of effort was put into MC (Monte-Carlo) simulations of cosmic rays in order to understand the calorimeter response. In particular, the rates of muons from cosmic rays, the energy deposited, and the signal timing were among the issues the simulations were intended to study. Apart from using cosmic ray events for further electronics testing, the cosmic ray simulations were used to determine if calibrations could be performed as in earlier test-beam studies [13, 14, 15] and what the potential was for using cosmic rays for physics studies. Here we further outline the motivations and describe two main methods of cosmic ray generation, comparing the results of each after running through the full-chain¹ analysis. Explanations of the signal reconstruction methods can be found in the following chapter.

¹Refer to Section 1.2.4

5.1 Motivation

It is important to have as good an idea as possible of the rates, energy, and general usefulness of cosmic rays in the calorimeters prior to dedicating time and resources to real data taking. To that end, the ATLAS software package Athena was used to perform MC simulation of cosmic rays. The muon flux at the detector was of primary importance because it determined the level of triggering required to identify cosmic muons and the amount of data that could be collected in a given period of calorimeter running. The simulation also indicated how much energy would be expected to be deposited in each calorimeter and even within each calorimeter cell. For the endcap calorimeters, the simulation of non-projective muons from cosmic rays was used to show how the energy would be deposited in calorimeter cells which were designed for particles emerging from the IP. Consequently, the cell energy in the endcap calorimeters was a major issue to be explained by the simulation and is a main focus of this work. Related to this is knowledge of how the signal timing would be affected by the randomly occurring muon hits, given that the timing of the calorimeter cells is calibrated for particles coming from the IP. An understanding of the timing would lead to a more accurate reconstruction of the energy deposited and was therefore also a key factor that was studied in the simulated data.

5.2 Cosmic Ray Generators

Generation of cosmic ray muons was predominantly done using a “single muon gun” generator whose output consists of muon four-vectors in HepMC² format, defined by the muon’s energy and momentum three-vector (E, p_x, p_y, p_z) . The initial energy and angular distributions are determined based on surface cosmic ray flux measurements, with the minimum and maximum energy and angle defined by the user. These muons are generated on the surface directly above ATLAS. The surface height (above ATLAS) and dimensions of the grid in which muons can be generated are defined in the generator software. As this was the default cosmic ray generator used in ATLAS, it was decided to check the results of the muon gun against a full air shower generator.

An interface between an air shower program called CORSIKA (COsmic Ray SIMulations for KAscade) and ATHENA was already available at the time. CORSIKA was used to

²Refer to Section 1.2.4

simulate an air shower caused by a primary cosmic ray particle from the top of the Earth's atmosphere down to a user-defined altitude. The particles created in the air shower that survived to the given altitude were used in the same way as the muons from the muon gun. Again a rectangular surface is defined above the ATLAS cavern and the four-vectors are used as input to Geant4, which simulates the particles from the surface down into the detector. The location and size of the rectangular surface are again defined by the user. Another aspect common to both the muon gun and air shower generators is the ability to define a sphere of any radius centered at a given point within ATLAS, such that only muons with trajectories crossing the sphere are included. This was used to create projective datasets wherein only muons traveling near the IP were accepted, and also endcap specific datasets for which the sphere was defined around a particular endcap.

5.2.1 Muon Gun Generator

Several datasets were created using the muon gun generator, but only the ones used for this study are described. Table 5.1 gives a description of each cosmic ray dataset generated using the muon gun. In the case of datasets 4935, 4936, and 4950, the surface above ATLAS on which muons were generated was defined to be a square with sides of length 300 m and the maximum angle the muons could make with the vertical was set at 70° . Dataset 5003 used different initial parameters, including surface dimensions and the maximum angle allowed, to emphasize the A-side endcap. In all cases, however, these parameters were chosen to include as many muons that would make it inside ATLAS while constraining the computing time required to simulate each dataset to a reasonable value. Also, many of the parameters were based on an earlier study of cosmic ray simulations in ATLAS [9], which ensured all events of interest were included.

The energy thresholds and distance of closest approach to the IP (sphere radius) for each dataset are also given in Table 5.1. For all datasets, the upper limit on the muon surface energy was set at 2 TeV mainly based on results of measurements performed on the surface by cosmic ray experiments [16]. The lower energy threshold set between 5 and 10 GeV was chosen to include as many of the low energy muons as possible to create a realistic dataset. However, it has been shown that on average, muons with a surface energy of at least 50 GeV typically make it inside the cavern [9]. This, however, does not exclude lower energy muons from also making it within the cavern, leading to the decision of a lower energy threshold. Dataset 4935 is a semi-projective muon dataset, with a tolerance of 8 m

Table 5.1: Parameters of each muon gun dataset used in this study.

Dataset	Surface Dimensions	Energy Range	Angle Cut	Sphere Origin	Sphere Radius
4935	-150 m < X < 150 m -150 m < Z < 150 m	Lower: 5 GeV Upper: 2 TeV	70°	(0,0,0)	8 m
4936	-150 m < X < 150 m -150 m < Z < 150 m	Lower: 5 GeV Upper: 2 TeV	70°	(0,0,0)	2.5 m
5003	-84.4 m < X < 84.4 m -76.0 m < Z < 93.6 m	Lower: 10 GeV Upper: 2 TeV	45°	(0,-2.280,8.815)	5.855
4950	-150 m < X < 150 m -150 m < Z < 150 m	Lower: 5 GeV Upper: 2 TeV	70°	(0,0,0)	25 m

around the IP. This region covers all of the LAr barrel and most of the LAr endcaps, but the majority of the analysis performed on it was focused on the barrel calorimeter. Further analysis on the barrel calorimeter was performed using the projective dataset 4936, which had a tighter tolerance around the IP of 2.5 m. Dataset 5003 was produced specifically for the endcaps, with the sphere of tolerance centered around one endcap and large enough to include all muons passing through the endcap. The geometry used for dataset 5003 was the garaged endcap position, which is the position of the detector during real cosmic running since space is required for the construction and commissioning of other ATLAS detectors to run in parallel. The position of the endcap in the garage position is shifted 4 m along the z -axis away from the IP. Finally, dataset 4950 was produced solely for this work in order to have a direct comparison between the results of the muon gun and air shower generators. It uses the nominal endcap position, as in datasets 4935 and 4936, but includes all of the ATLAS detector, such that both the barrel and endcaps are entirely included.

5.2.2 Air Shower Generator

CORSIKA is a program that simulates the extensive air showers caused by high energy cosmic ray particles. It has the capability of simulating air showers caused by many types of primary particles, from light nuclei such as protons all the way up to iron nuclei, as well as photons and many elementary particles. The CORSIKA program can be divided into four parts; (1) The tracking of particles through ionization loss, scattering, and decay, (2)

Hadronic interactions of nuclei and hadrons with air nuclei at higher energies, (3) Simulation of hadronic interactions at lower energies, and (4) Transport and interaction of electromagnetically interacting particles. Several models are available for the latter three parts. For this work, the Dual-Parton Model (DPMJET) was used to simulate the high energy hadronic interactions and the Gamma Hadron Electron Interaction SHower code (GHEISHA), a well tested detector MC program, was used for the low energy hadronic interactions.

Apart from the primary particle, the user can define many initial parameters of the air shower. These include the number of events, the energy range of the primary particle, the range of zenith and azimuth angles, the surface altitude, atmospheric model, magnetic field, and particle interaction models, as well as numerous other parameters [17]. By default, the air shower is initiated at a random height above sea level, with an upper limit of approximately 113 km, which is the top of the atmosphere. However, most air showers are initiated below 30 km in altitude. For central Europe, as well as all other locations, the mass overburden vanishes above this altitude. Since nearly 90% of all incoming cosmic rays are protons [16], they were used as the primary particle for the air showers studied in this work. However, α -particle initiated air showers were also produced for comparison, as they make up approximately 9% of all cosmic rays.

All of the parameters used for the air showers in this work are given in Table 5.2. The energy range of the primary particle E_p is based on results of atmospheric cosmic ray experiments [16]. The coordinate system used by CORSIKA is shown in Figure 5.1. The zenith angle of the primary particle θ_p is defined as the angle between the particle's momentum and the vertical, and its azimuth ϕ_p is the angle measured from the horizontal component of the particle's momentum with respect to the magnetic north direction. In the standard CORSIKA program, a flat atmosphere is adopted with the air density decreasing with height. This is a good approximation for zenith angles less than 70° , but above this threshold the curvature of the Earth must be taken into account and the CURVED atmosphere model must be used. It was found that using the curved model with an upper limit zenith angle of 90° increased the time of the simulation by a large amount without increasing the statistics by any significant measure. As a result, the standard atmosphere model was used with an upper limit of 70° . The magnetic field at the elevation of the Point 1 site of the LHC in Meyrin was computed using *Geomag* [18]. CORSIKA contains several atmospheric models based on measurements of the density in 5 layers [17]. The best available model was the central Europe data measured above Stuttgart, Germany during

Table 5.2: Parameters used for the air shower simulations produced for this work using CORSIKA.

Energy Range of Primary Particle	$500 \text{ GeV} < E_p < 50 \text{ TeV}$
Zenith Angle Range of Primary Particle	$0 < \theta_p < 69.9^\circ$
Azimuth Angle Range of Primary Particle	$0 < \phi_p < 360^\circ$
Observation Level	507.3 m (Altitude of Meyrin) [19]
Horizontal Component of Earth's Magnetic Field, B_x	$22.18 \mu\text{T}$
Vertical Component of Earth's Magnetic Field, B_z	$41.49 \mu\text{T}$
Atmospheric Model	Central Europe, June 1993

various days in 1993. Our tests showed insignificant differences between winter (February) and summer (June) models.

CORSIKA software version 6.501 was used for this analysis and in total, 1 million proton produced air showers were generated using the aforementioned parameters. CORSIKA was used to plot an air shower with similar parameters as those used for the dataset created; this is shown in Figure 5.2. The output of CORSIKA was used in the same way as the output of the muon gun generator, except in this case each event could contain many particles instead of just the one muon. The same parameters were used here as for dataset 4950, encompassing the entire ATLAS detector.

5.3 Simulation and Digitization

The Geant4 program was used to perform the simulation of the particles from the surface down into the ATLAS detector. In addition to the standard ATLAS geometry, the rock overburden and access shafts were included in the simulation. The density of the overburden used was 2.33 g/cm^3 , which is an average of the predominant compound silica and other materials. The density actually ranges from 2.3 to 2.5 g/cm^3 with depth [9]. The response of only the calorimeters, referred to as hits, was turned on in the simulation, and the ATLAS magnetic fields were switched off. Figure 5.3 shows a graphical representation of an older Geant3 simulation [9] (similar to Geant4, which was not available) of muons from the surface passing through the overburden and access shafts to produce hits within the detector. The simulation stage stores the hits, which are later digitized to simulate the response of

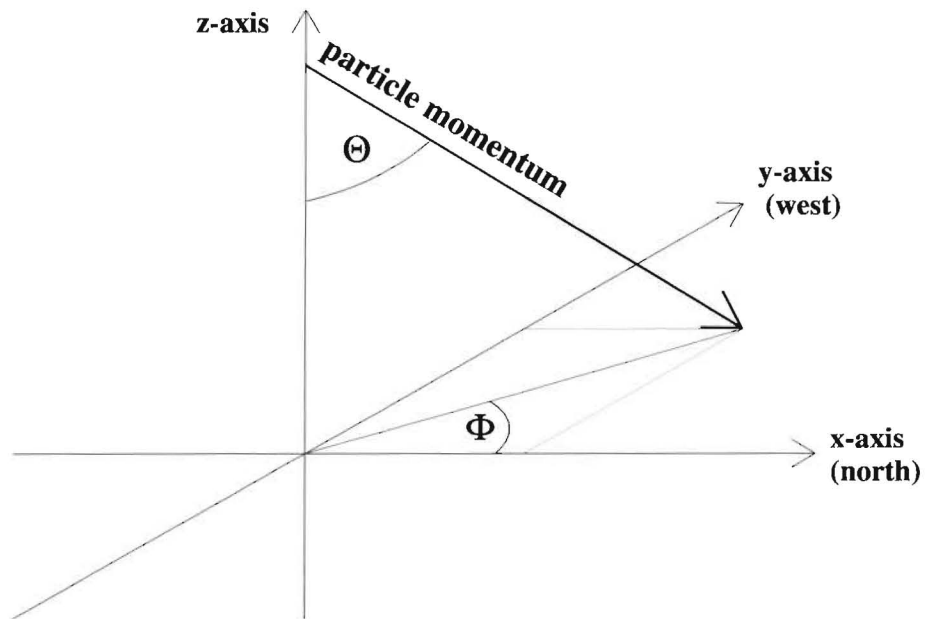


Figure 5.1: The coordinate system used in CORSIKA [17].

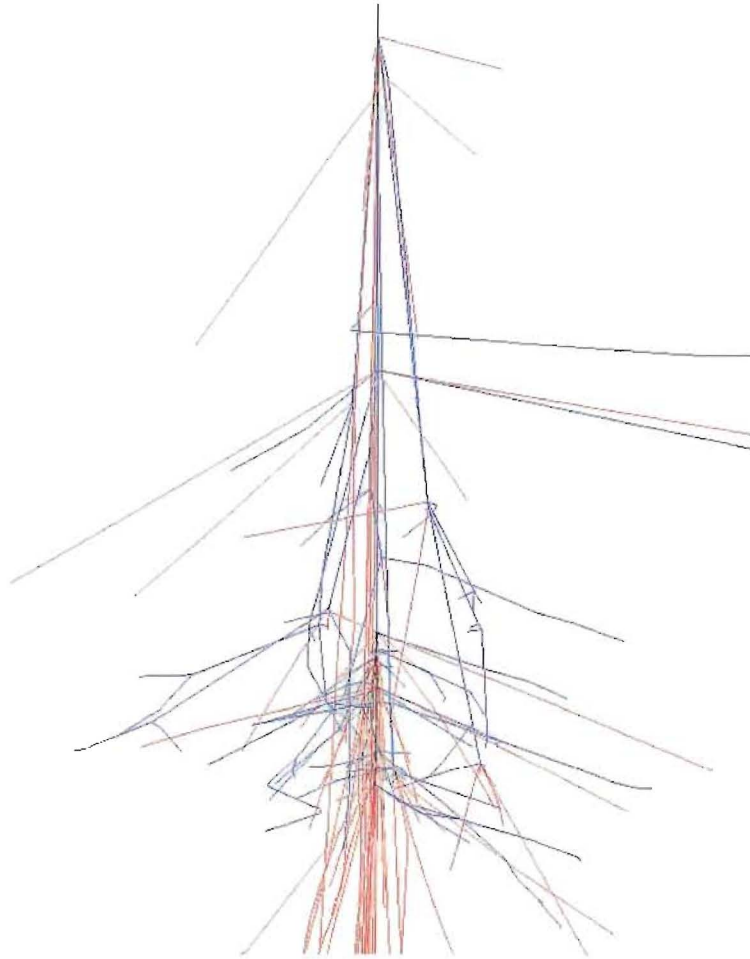


Figure 5.2: An air shower created by a primary proton with energy 1 TeV and $\theta_p = 0$ simulated by CORSIKA. All other parameters are the same as in Table 5.2. Here the blue lines correspond to hadrons, whereas the red lines correspond to muons. The plot dimensions are ± 5 km in the x and y directions (perpendicular to the shower axis) from center and from a surface altitude of 507.3 m to the first interaction height of 30 km.

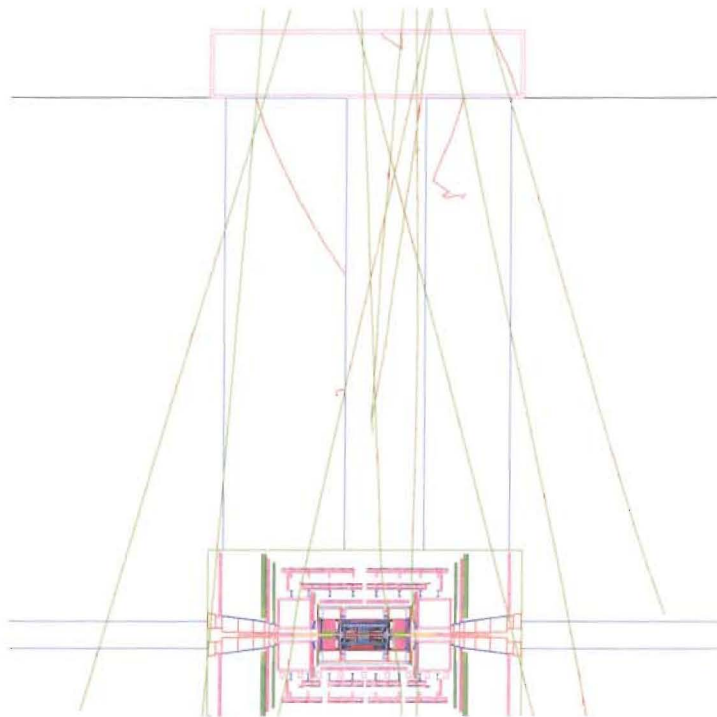


Figure 5.3: A graphical representation of the simulation of cosmic rays in ATLAS. The layout here is of the ATLAS cavern, access shafts, and surface buildings using Geant3, similar to the current Geant4 simulation [9].

the electronics. During digitization, electronics noise can also be mimicked by adding to each calorimeter cell values generated from a Gaussian distribution. A random value from a Gaussian distribution is used to place a weight on an element of the noise covariance matrix, and this is in turn used to weight the known RMS noise of that particular cell. The noise is added to the signal as an ADC count. No noise was included for the comparison of the air shower with the muon gun simulations, in order to reduce the time required to run the digitization and have reasonable file sizes. For the endcap analysis, however, dataset 5003 was digitized twice; once without and once with electronics noise, mainly to see how well the cosmic ray signal could be seen above the noise level. Each cell hit is converted to a digitized signal in a corresponding electronic channel and these digits are stored as for real data to be reconstructed. The methods of signal reconstruction are explained in Chapter 6.

5.4 Results

A comparison was made between the results from the cosmic-ray simulations using the muon gun and air shower generators. The muon gun dataset used in all cases here is dataset 4950. In Figure 5.4, the angle with respect to the vertical and the momentum of the incoming muon at the surface are given for each of the two generators. These are for all muons at the surface, which make it within the 25 m radius of the sphere centred around the ATLAS IP. As noted in Table 5.1, the minimum energy of muons for dataset 4950 was set to 5 GeV, and this same limit was set as the lower energy threshold in the air shower for muons surviving to the surface. The surface momentum comparison in Figure 5.4 suggests that perhaps the muon's initial momentum is either underestimated by the data used in the muon gun or overestimated by the models used by the air shower simulator. The larger average surface momentum of the muons from the air shower explains the slightly larger initial angle for the same muons, compared with the muon gun result. Through some testing with the muon gun generator, it was found that increasing the surface energy of the muon allowed more muons to be generated farther away from the center of the square surface. The reason is that the larger energy muons are able to traverse through more rock, which causes the angular distribution to be skewed towards larger angles. For the typical surface energies of muons from cosmic-rays, however, Figure 5.4 indicates that the majority are nearly vertical. The general agreement in both plots indicates the muon gun is a reasonably accurate generator of muons from cosmic rays.

The reconstructed results of each of the two methods of muon generation were also compared. Figure 5.5 shows the reconstructed energy in cells of the LAr calorimeters. The energy deposited per cell agrees very well for the two cosmic-ray generators. Typically, these muons are minimum ionizing particles and therefore deposit roughly the same amount of energy per cell.

Since, apart from protons, α -particles make up nearly the rest of all cosmic rays, they were also studied. 50,000 air showers caused by α -particles were also simulated using CORSIKA. The results were compared with those of the proton-induced air showers. The primary purpose was to check the effect the α -particle air showers would have on the muons that would survive into ATLAS. The angular distribution and momentum of the muons at the surface for each type of air shower were plotted for both muons producing a hit within ATLAS and for all muons that pass the optimization cuts, such as passing through the 25 m

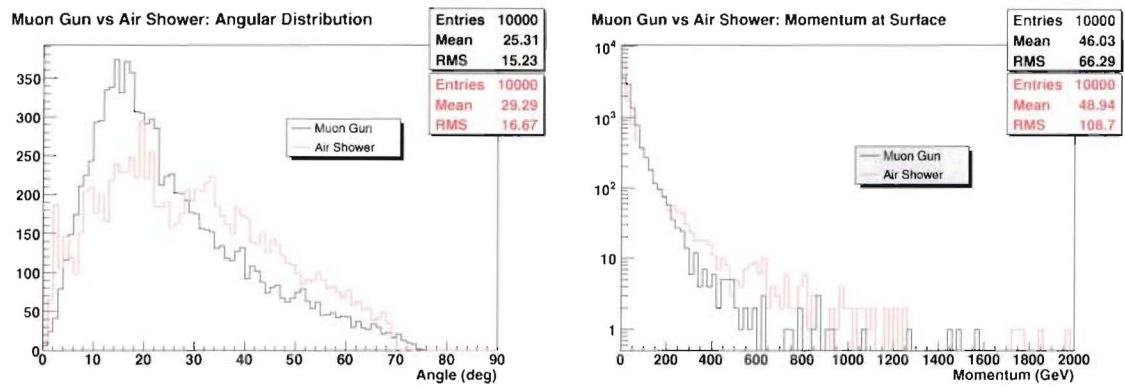


Figure 5.4: A comparison of the angle of the muons with respect to the vertical (left) and the momentum of the muons (right) at the surface, for the muon gun dataset 4950 (black) and the air shower simulation (red).

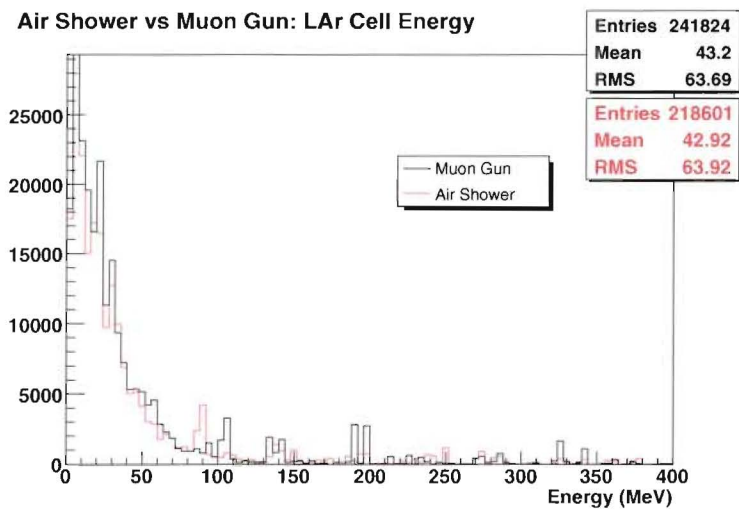


Figure 5.5: A comparison of the LAr cell energy for muon gun dataset 4950 and the air shower simulation.

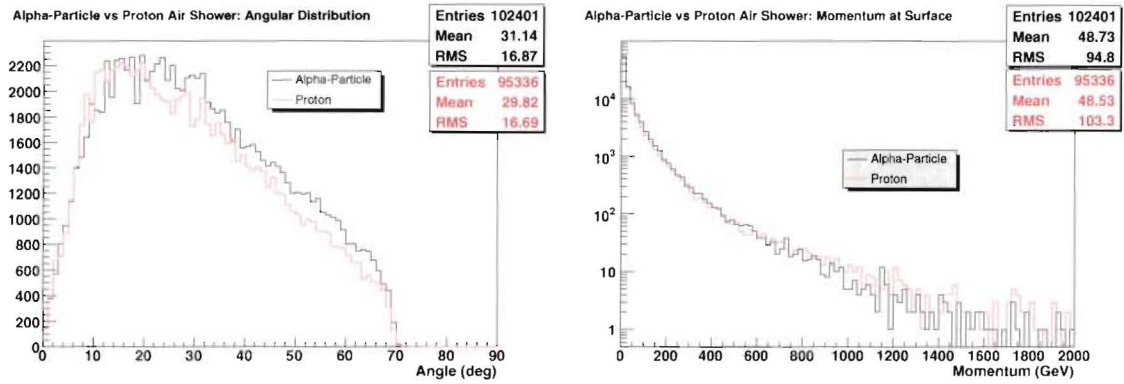


Figure 5.6: A comparison of the angle of the muons with respect to the vertical (left) and the momentum of the muons (right) at the surface, for air showers caused by α -particles (red) and protons (black). These are for all muons on the surface which pass the optimization cuts, such as passing through a sphere of radius 25 m, centred around the IP.

radius sphere around the IP. The results for the latter are given in Figure 5.6 and in Figure 5.7 for the former. In Figure 5.7, the angular distribution falls off much faster than in Figure 5.6 since it is far more likely that muons with a shorter, more vertical trajectory, will produce a hit within ATLAS. In all likelihood, the muons with a larger initial angle in Figure 5.6 lose too much energy traversing through more rock to produce a hit within ATLAS. Also note that the number of entries is different. Although the number of air showers is the same for each type of particle, the number of muons that survive to the surface above ATLAS is different. There are more muons for the same number of air showers for α -particle cosmic rays because they are more likely to interact via the strong force, leading to production of pions which decay to muons. The general agreement in these plots suggests that the muons of interest have similar properties for the two types of cosmic rays.

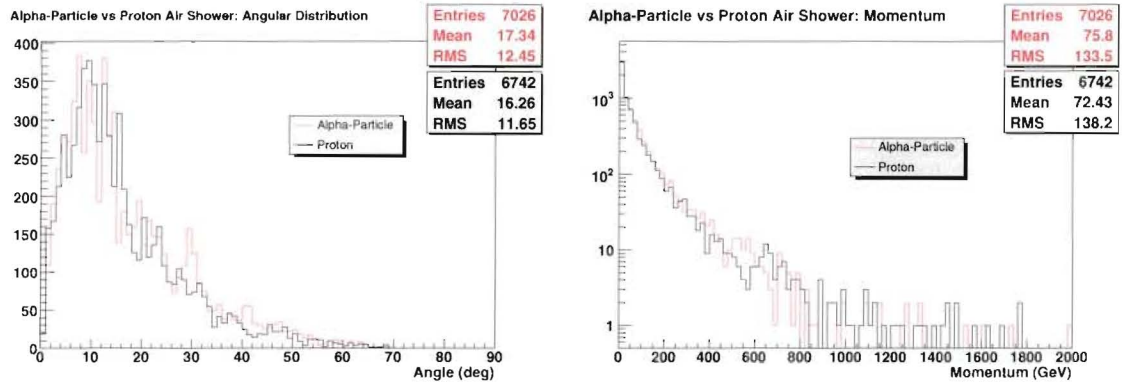


Figure 5.7: A comparison of the angle of the muons with respect to the vertical (left) and the momentum of the muons (right) at the surface, for air showers caused by α -particles (red) and protons (black). These are only for muons which pass the optimization cuts and produce a hit within ATLAS.

Chapter 6

Cosmic Ray Reconstruction and Analysis

There are various methods used to reconstruct the energy deposited in the calorimeters. It is a particular challenge for cosmic rays since the calorimeters were designed for particles emerging from the IP. The random occurrence of energy deposits by cosmic rays requires a dedicated trigger and reconstruction algorithm. In this chapter we outline the various methods of reconstruction available and compare the results of these methods applied to MC and real data in both the LAr barrel and endcap calorimeters.

6.1 Signal Reconstruction

For real data, the ionization current waveform induced by electrons drifting through the LAr gap is triangular in shape since the number of mobile electrons reduces linearly in time [4]. The bipolar shaping applied to this physics ionization current signal by the FEBs results in the waveform in Figure 6.1. Whether the signal came from real data or MC simulation, the shape of the signal and the methods applied to reconstruct the energy deposited in the LAr are the same. In Figure 6.1 the points represent the measured ADC counts, which are sampled approximately every 25 ns, corresponding to the 40 MHz LHC bunch frequency. In the LAr calorimeters, the amplitude of the ionization signal is proportional to the energy deposited. There are several methods available to determine the signal peak, such as polynomial fitting, but the method of Optimal Filtering (OF) is typically preferred because

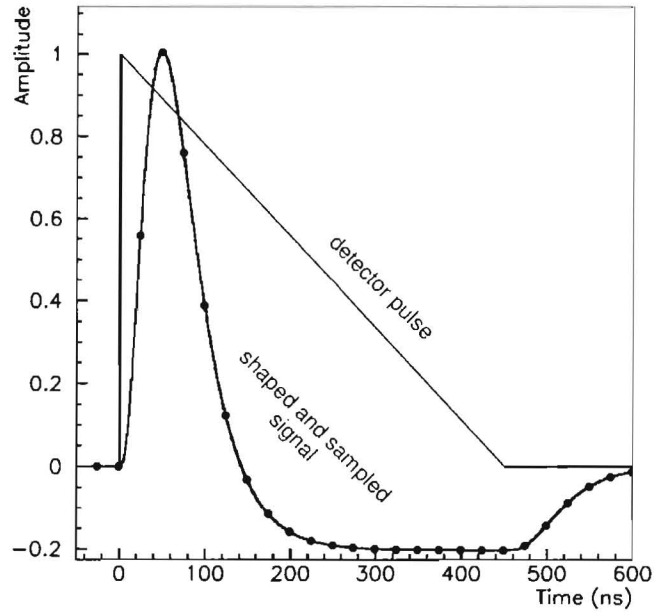


Figure 6.1: The LAr ionization current pulse and the shaped signal with the 25 ns time samples given by the points [11].

it minimizes the electronics noise contributions [20]. In this method, the amplitude of the signal peak (A) and the peak time deviation (t) are given by:

$$\begin{aligned}
 A &= \sum_{i=0}^{N-1} a_i s_i \\
 A \cdot t &= \sum_{i=0}^{N-1} b_i s_i
 \end{aligned} \tag{6.1}$$

where a_i and b_i are the optimal filtering coefficients (OFCs), s_i is the ADC count for the i -th time sample after pedestal subtraction, and N is the number of time samples, which is typically 5 in the ATLAS LAr calorimeters. The value t is the signal starting time and should be zero if the signal is well known. The OFCs are determined using calibration pulses for each channel in each gain and are stored in a database. For collisions occurring at the IP, the read-out clock and bunch crossings are synchronized such that the signal peak will always occur at a particular time sample (Typically the 3rd of 5 time samples from $t = 0$ as in Figure 6.1). For cosmic ray muon data, this is not the case since the cosmic

ray will occur randomly and therefore be asynchronous to the read-out clock. As a result, the a and b OFCs have been calculated in a region that spans between two time samples in bins of approximately 1 ns. The right set of OFCs is selected using the phase between the time at the peak of the calibration and physics pulses. Once the amplitude of the peak is determined, a set of conversion factors, such as the ramp¹, are applied to convert the ADC value to an energy value in units of MeV.

6.1.1 Reconstruction Tools and Timing

During the reconstruction process, one can define the method(s) to use to determine the signal peak. As mentioned above, for cosmic rays the peaks may occur at varying times with respect to a fixed time sample and it becomes a more difficult task to locate the peak. Several reconstruction tools have been created for this purpose.

The LAr reconstruction process is designed to loop over all requested tools until one succeeds in its task. Generally, the first tool in the list, which is intended to succeed, performs the most advanced reconstruction algorithm, with subsequent tools performing simpler tasks. For example, in many cases pedestal or ramp values are not available from the database and therefore fixed values may be used. One particular peak finding tool was created for cosmic rays, hereafter referred to as the Iteration tool. Its main task is to iterate over a range of time samples to find the maximum ADC value. It does this by taking an initial phase value to select the OFCs and therefore the values A and $A \cdot t$ of Equation 6.1. It then uses the result to determine another phase value and iterates until the relation $A \cdot t / A < 1$ ns is reached, which is sufficient as $A \cdot t / A = 0$ ns occurs when the time of the physics signal is perfectly known. The drawback to this method is that the iteration fails when the signal amplitude is small, and an accurate result is only achieved therefore for large signals. The default values used by the iteration tool are given in Table 6.1. Only the time sample range was varied in the studies presented here.

If the ADC counts available are below the required threshold, then the iteration tool fails, and a fixed time sample and phase are used to determine the peak using OF, here referred to as the Fixed method. There are also cases in which OFCs are not available for a particular channel and the OF method fails. One backup tool uses a cubic fit to three time samples around the expected peak location, which can be unknown for cosmic rays, making

¹Refer to Section 4.2.3

Table 6.1: Parameters used for the Iteration peak reconstruction tool.

Minimum ADC Required	15
Minimum Time Sample	2
Maximum Time Sample	10
Initial Phase	12 ns

this tool inaccurate for their reconstruction. Another tool averages the ADC counts over 5 time samples, starting from the default position of the second time sample. There is also a parabola fitting tool which is rarely used.

6.2 Using Tile Calorimeters

Commissioning with cosmic rays was planned to be performed before the full ATLAS trigger system became available, which in any event was designed for triggering on collisions from the IP. Consequently, trigger boards were built for the purpose of having a cosmic trigger generated by the Tile calorimeter [10]. In total, 8 trigger boards were connected, one for each of the sections in the Tile calorimeter, as pictured in Figure 6.2. The A-side and C-side are as defined in Section 1.2.3. The top section of the calorimeter is defined as $y > 0$ and the bottom as $y < 0$. A trigger on a cosmic ray signal is defined by applying the logical OR to signals in boards connected to the top (bottom) section and applying the logical AND to the resulting top and bottom signals (see Figure 6.2). Such a scenario would occur only if a particle deposited energy in both the top and bottom sections of the Tile calorimeter, which is indicative of a cosmic ray muon. Cosmic rays in the LAr are triggered using these Tile trigger boards in coincidence.

In order to use the information from the Tile trigger boards in reconstructing the signal in the LAr, an algorithm was developed called TileMuonFitter (TMF). In this algorithm, the energy deposited in the Tile cells is used to determine a muon track, which is propagated to the $y = 0$ plane. This is done by weighting cells with their energy density and fitting a track that minimizes the square of the orthogonal distance to those hit cells. The time of each hit cell is assigned to a point on the track closest to that cell. After shifting the time at each of these points along the track by the time-of-flight (TOF) to the horizontal plane, the mean is taken to yield the time at $y = 0$. This method depends on the timing of the cells

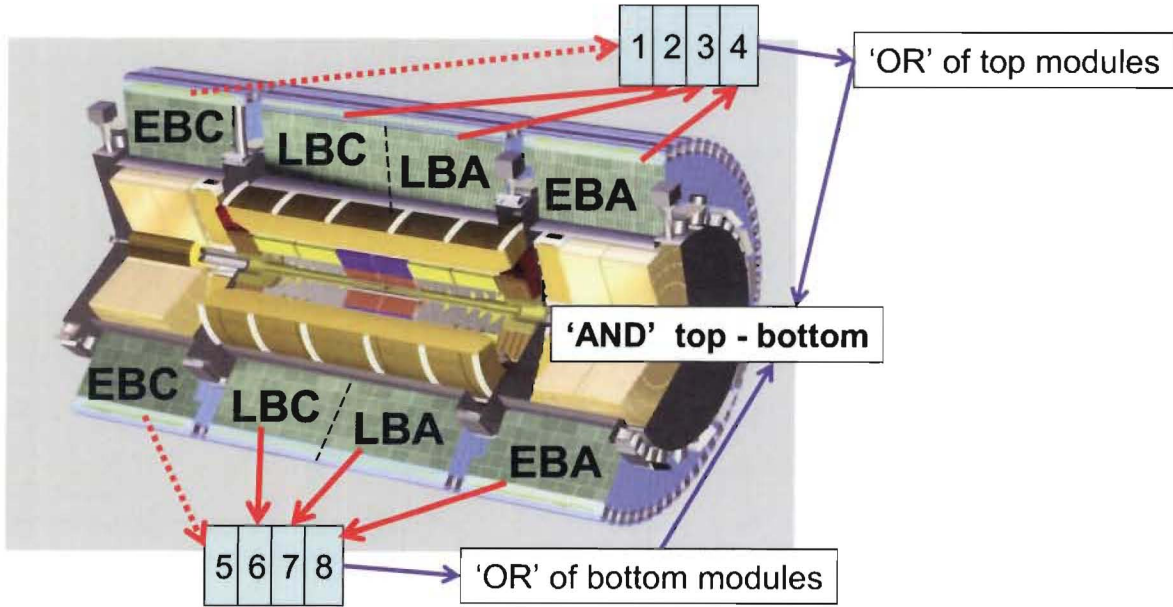


Figure 6.2: The layout of the Tile trigger boards used in coincidence for cosmic data taking.

in the Tile calorimeter, which have been calibrated in time by including time offsets per electronic channel calculated from LED or laser calibration runs.² In addition, the cell times have been corrected for the wavelength shifting fibers that carry the scintillation light to the PMTs. In the end, the output of the TMF algorithm is a time at $y = 0$ with a precision of 1-2 ns [21]. It also yields the position and direction of the muon in the horizontal plane.

Systematic tests were performed on this algorithm using various artificial time offsets to check the response. A Gaussian distribution with a mean of 0 and a standard deviation $\sigma = 10$ ns was applied to the trigger time during the digitization of a number of events from MC dataset 4936 (see Table 5.1). A constant offset of 40 ns was also applied to the trigger time in the same fashion. The results of the two tests are given in Figure 6.3. From these we concluded that the TMF algorithm responded as expected to offsets in the arrival time of cosmic muons.

²Laser light and LEDs (Light Emitting Diodes) are used to simulate the light from the Tile calorimeter scintillators in order to calibrate the response of the PMTs.

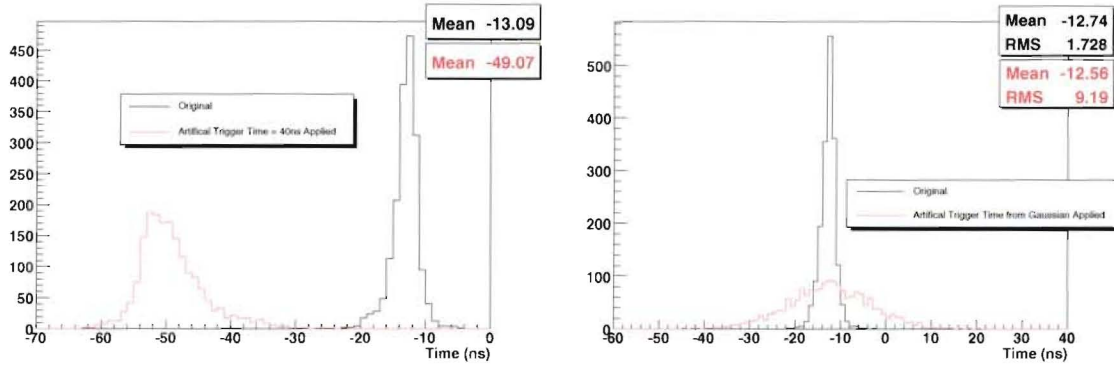


Figure 6.3: The response of the TMF algorithm after applying artificial trigger times using a constant of 40 ns (left) and a Gaussian distribution with $\sigma = 10$ ns (right). Plotted here is the time from TMF at $y = 0$ using cosmic ray MC dataset 4936.

6.2.1 Tile Timing Tool

A new reconstruction tool was written to use the information provided by the Tile calorimeter, through the TMF algorithm. The purpose of this tool was to determine the peak time and phase of the LAr signal, to be used by the OF method. This tool, henceforth referred to as the TileInfo tool, was incorporated into the reconstruction scheme for the LAr calorimeters. It extracts the information provided by TMF, including the time, position, and direction of the muon at $y = 0$. If a muon track does not exist for the given event, it uses the Fixed method by default, though the Iteration tool can also be invoked. Several timing corrections are applied to get the true time at each LAr cell. The first is the TOF along the muon track from the LAr cell to the $y = 0$ muon track position, which is subtracted (added) if the LAr cell is in the top (bottom) of the $y = 0$ plane. In ATLAS, cabling offsets correct for the TOF from each LAr cell to the IP, such that particles coming from the IP occur at the same time in the electronics for each cell. The second correction is, therefore, the TOF from each LAr cell to the IP. Finally, a timing offset exists between the Tile and LAr internal clocks. This global time offset is not known *a priori* and must be calculated from data or MC using results from another reconstruction tool, such as the Iteration tool. Once this is measured, the TileInfo tool shifts the time samples by the total time offset and calculates the phase. The following equation determines the total time offset, t_{LAr} , for the top and bottom LAr sections:

$$\begin{aligned}
t_{LAr}^{top} &= t_{TMF} - TOF_{y=0} - TOF_{IP} + t_{global}^{top} \\
t_{LAr}^{bot} &= t_{TMF} + TOF_{y=0} - TOF_{IP} + t_{global}^{bot}
\end{aligned}
\tag{6.2}$$

where t_{TMF} is the time at $y = 0$ from TMF, t_{global} is the global time offset between the LAr and Tile calorimeters, and $TOF_{y=0}$ and TOF_{IP} are the time-of-flight values between each LAr cell position and the $y = 0$ and IP positions respectively. Note that the sign in front of $TOF_{y=0}$ is negative for events in the top section and positive for events in the bottom section, assuming the muon is traveling downward. The signs are reversed if the muon is traveling upwards, which is accounted for in this tool. Also note that the value of t_{global} is different for the top and bottom sections, though in most instances the difference was almost negligible. Other time offsets including variations between FEBs and individual channels of FEBs were studied. Figure 6.4 shows the FEB dependent offsets for cosmic data. It was found that the FEB dependent offset was less than 10 ns, and since t_{global} usually had a width of this order, the FEB dependent offset was not applied. The variation in the time from each FEB is partly due to the channel dependent offsets and this is on the order of < 10 ns and therefore also negligible.

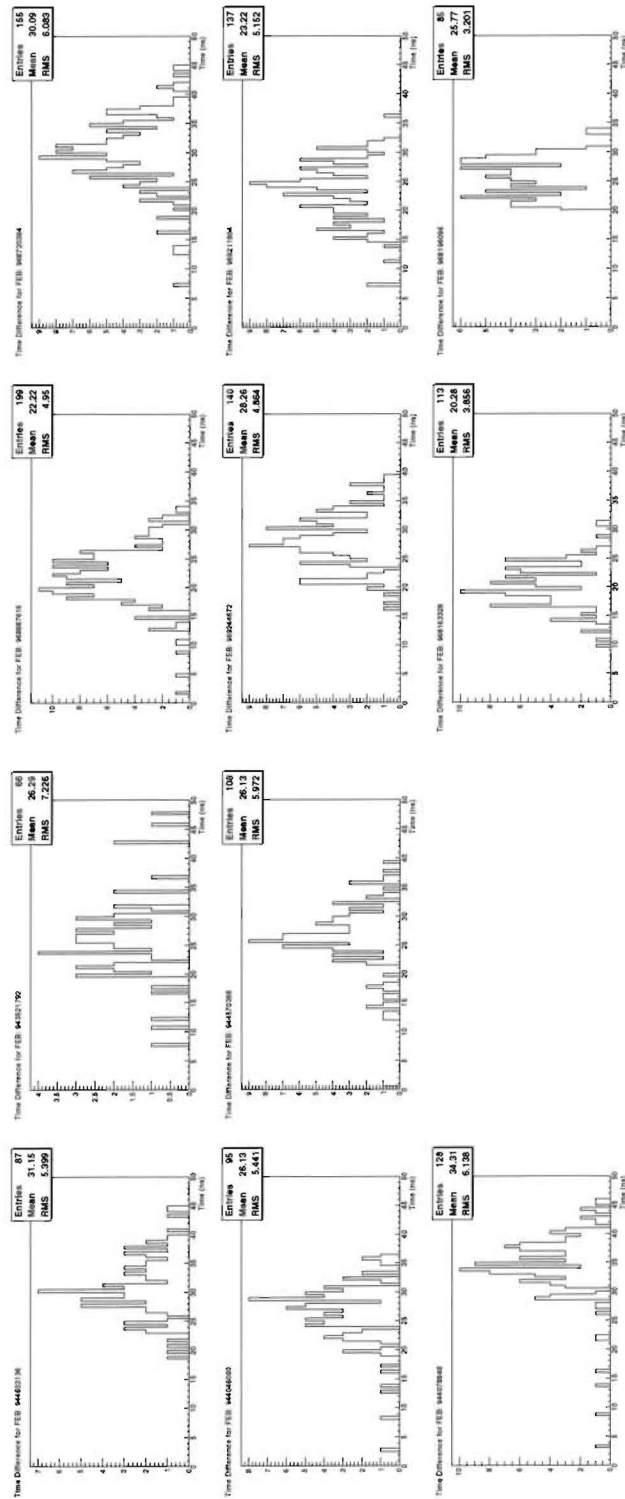


Figure 6.4: The global time offset t_{global} for each FEB in the top (left) and bottom (right) LAr sections having at least 50 muon hits each with a minimum cell energy deposit of 300 MeV. This is from all cosmic data taken in the EM barrel. Details of these data are given in Section 6.5.

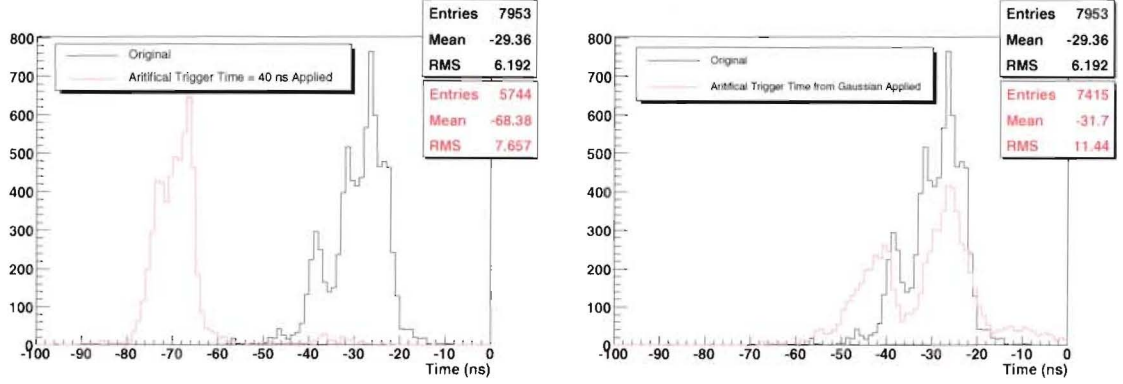


Figure 6.5: A check of the TileInfo tool performed by applying artificial trigger times during the digitization of MC dataset 4936. A constant offset of 40 ns (left) and a random offset from Gaussian distribution with $\sigma = 10$ ns (right) are applied.

The equation that determines the time of a LAr cell [22] is given by:

$$t = (24(n_{peak} - 3) - (t_{phase} - \tau - 25))(25/24) \text{ ns} \quad (6.3)$$

where n_{peak} is the time sample at which the LAr signal peaks, the phase t_{phase} , is as defined earlier (Section 6.1), and τ is the relation $A \cdot t / A$ (Equation 6.1). This equation was used to derive the phase and n_{peak} for each LAr cell using the result of Equation 6.2. Following this process, the same peak reconstruction method is applied as with the Iteration tool using OFCs to determine the time and energy of the LAr signal.

Systematic tests were performed on this tool using the same artificial time offsets as used to test the TMF algorithm. The results are given in Figure 6.5. The time of the signal peak in each LAr cell is offset by approximately the same amount as the artificial trigger offset, confirming that the TileInfo tool correctly determines the signal times. Refer to Section 6.4 for an explanation of the multiple peak structure in the timing distribution.

6.3 Cosmic Ray MC Analysis

The various reconstruction tools were applied to cosmic ray MC dataset 5003 (see Table 5.1) for analysis of the timing. For this analysis, digitization was performed with and without noise to observe the effect expected in real data. The focus of the analysis in this work is

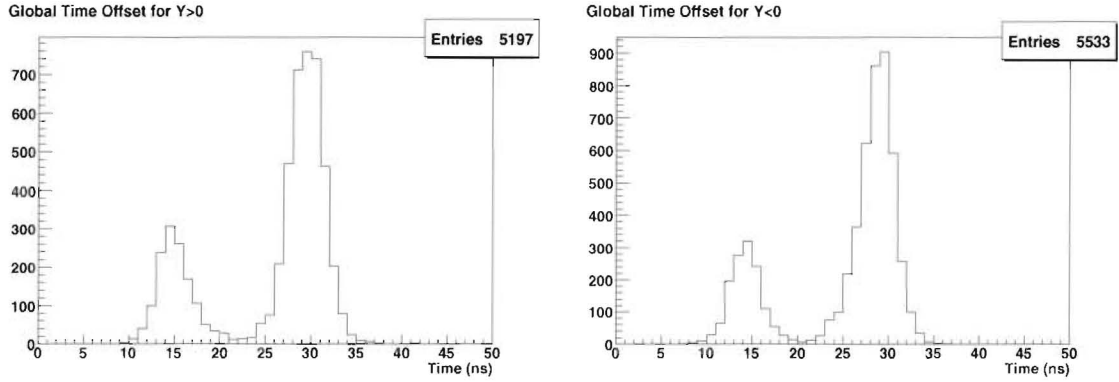


Figure 6.6: Result of the calculation of the global time offset t_{global} for MC dataset 5003 (LAr Endcap) in the top (left) and bottom (right) LAr sections. The peaks on the left and right of each plot correspond respectively to muon hits in the Tile barrel and extended barrel regions.

testing the effectiveness of the TileInfo reconstruction tool, and therefore comparisons of the results using that tool were made with the results of the other default reconstruction tools.

For the TileInfo tool, first the global time offset was found using the result of the LAr cell times reconstructed using the Iteration tool. This is done by solving for t_{global} in Equation 6.2. The results, without noise, for the top and bottom sections are given in Figure 6.6, from which it is clear that there are two distinct values for the global time offset. It was found that one peak refers to muon hits in the Tile barrel and the other to hits within the Tile extended barrel. As dataset 5003 was intended to focus on the endcap, the global time offset between the LAr cells in the endcap and cells in the Tile extended barrel was determined and is shown in Figure 6.7. Note that the resolution on this value is approximately 2 ns, which is the precision of the time from TMF, meaning the LAr time has a similar precision for this MC dataset. Several cuts were applied to obtain these plots using the Iteration tool. The minimum LAr cell energy was required to be 150 MeV, since it was found that even without noise included, cells with energy lower than this contributed to rogue values in the time. Also, the distance between the cells and the muon track from TMF was required to be less than 20 cm to ensure only cells within the vicinity of the muon track were included.

Using the values found for the global time offset, the LAr cell times were computed using

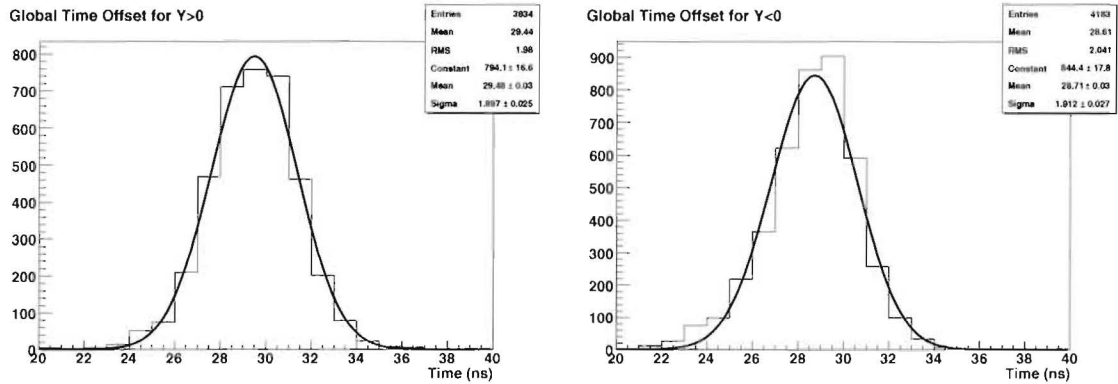


Figure 6.7: A Gaussian fit of the global time offset t_{global} in the endcap region for the top (left) and bottom (right) LAr sections.

the TileInfo reconstruction tool. A comparison of the LAr cell time found using the TileInfo tool was made with the results of the Iteration tool. The same cuts were applied as before, except that in addition to looking at high energy events where the cell energy is greater than 150 MeV, low energy events were also analyzed. The results are shown in Figure 6.8 for the EMEC. For the high energy events, the LAr cell times agree well for the two different methods of reconstruction, since the Iteration tool is expected to work well here. This is therefore an indication that the TileInfo tool also works well for these events. For the low energy events, it is clear that the Iteration tool fails in some cases, but both tools produce multiple peaks. The main reason for the lack of a well defined timing distribution in the endcap is the fact that the majority of the muons have a near vertical trajectory. Since the endcap cells were designed to contain showers from projective events, the showers from cosmic ray muons are not well contained and can therefore produce different times based on how they hit a given cell. Refer to Section 6.4 for further details on the investigation of the cell timing distribution.

Digitization was performed on dataset 5003 with noise included and again the results from the different reconstruction tools were compared. In this case, the minimum cell energy was required to be 450 MeV, since this is the upper end of the noise level for the majority of EMEC cells. Although for HEC and FCAL cells the noise can reach a few GeV, it was found that increasing the cell energy threshold reduced the event number by a large amount without changing the overall structure of the distribution. The results from the Iteration,

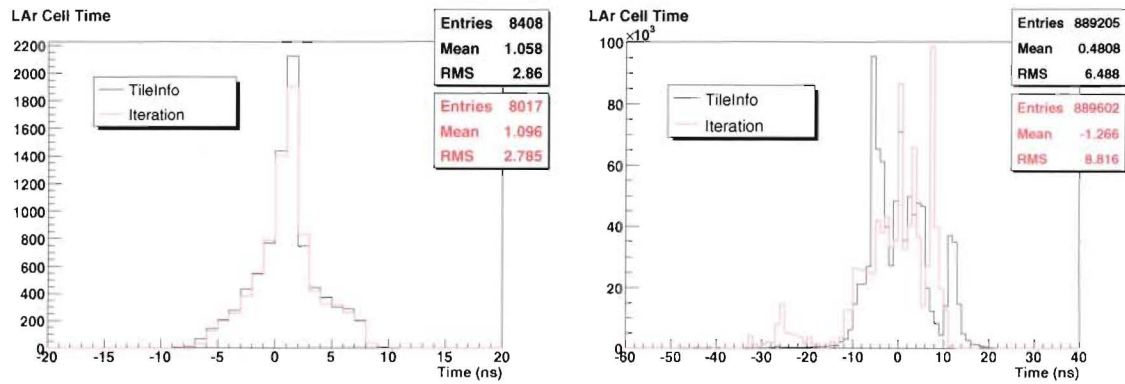


Figure 6.8: The results of the LAr cell times found in the EMEC using the TileInfo and Iteration tools. The plot on the left is for LAr cells with a minimum energy of 150 MeV, while the plot on the right is for cells with energy less than 150 MeV, but greater than zero.

TileInfo, and Fixed methods are given in Figure 6.9. For the Iteration result, the cells with a time value greater than 100 ns were found to originate from FCAL cells with energy greater than 2 GeV. These are not seen using the other two methods, leading to the conclusion that these probably correspond to noisy cells which the Iteration tool finds, whereas the TileInfo and Fixed methods do not, since they do not search for the time sample with the largest signal amplitude. In fact, a main advantage of the TileInfo tool is avoiding reconstruction of noisy cells, since it finds the time sample based on cosmic ray triggering information from the Tile calorimeter.

In the case of the Fixed method, the cell times are offset from zero, but the overall distribution agrees well with the result of the TileInfo tool. The general reason for the good agreement comes from the fact that the surface generated muons will typically occur within 1-2 time samples of each other. Therefore, a fixed time sample and phase will often yield the correct result for MC simulated muons. For real cosmic data, however, the muons are not limited to a pre-defined surface so they are further spread apart in time. Refer to Section 6.6 for the results of the LAr cell energy distributions for each reconstruction method.

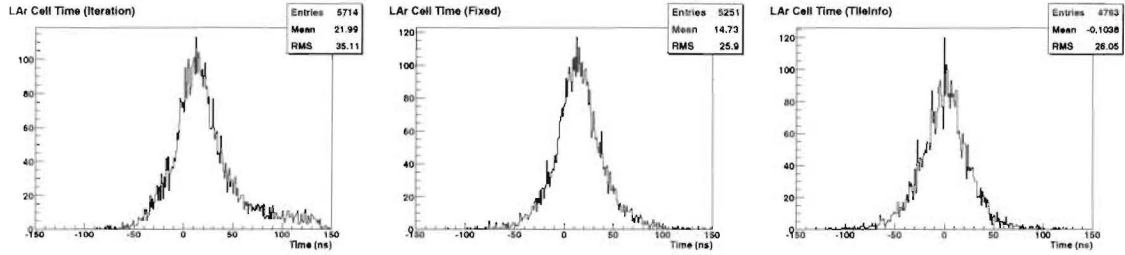


Figure 6.9: The results of the LAr cell times for MC dataset 5003 with noise included, found using the Iteration (left), Fixed (center), and TileInfo (right) tools. The minimum LAr cell energy required is 450 MeV.

6.4 Distribution of the LAr Cell Timing

6.4.1 MC Cosmic Rays in the EM Barrel Calorimeter

This section summarizes the investigation of the timing in MC dataset 4936, which contains semi-projective cosmic events in the barrel calorimeter region.

First we make the comparison between the two main methods of timing reconstruction for cosmic rays; the Iteration and TileInfo reconstruction tools. In this case, the minimum energy in each LAr cell is required to be at least 150 MeV. Also, the cells are required to be within 20 cm of the muon track determined by the TileMuonFitter algorithm. Finally, only muons which strike the Tile barrel region are included, whereas those hitting any part of the Tile extended barrel are excluded. This is done to ensure no timing offsets between the two Tile calorimeter sections interfere with the analysis of the timing in the LAr cells. Given these conditions, the timing in the LAr cells is given in Figure 6.10 for both the Iteration and TileInfo reconstruction methods. Multiple peaks are seen for both cases, and since the Iteration tool is used by default and is intended to work well at high energies, the remaining analysis was performed with the Iteration results. In each step, however, the results from the TileInfo method were analyzed as well and were found to agree well with the Iteration method.

As a first step, only muons with a hit in both the top and bottom sections of the LAr barrel calorimeter were included. The effect of this cut is given in Figure 6.11. It was found that by isolating the different layers of the LAr calorimeter, the number of peaks was reduced. This is a TOF effect since the time of a hit in each layer for a particular event

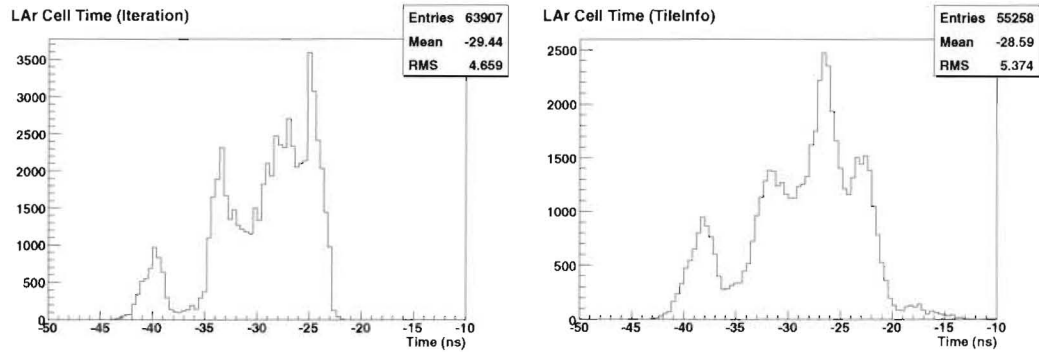


Figure 6.10: The timing in the LAr cells for dataset 4936 found using the Iteration (left) and TileInfo (right) methods of reconstruction. The minimum cell energy is required to be 150 MeV and only muons within the Tile and LAr barrel regions are included.

will be different due to the TOF of the muon from one layer to the next. In particular, the majority of the muons deposit their energy within the middle layer, with the remaining muons depositing energy in the presampler. Therefore, only muons in the middle layer were included, and the top and bottom sections were isolated in order to understand the origin of the multiple timing peaks. The results are given in Figures 6.12 and 6.13.

As these are only semi-projective events, meaning that events are included which may hit the calorimeter in a non-projective manner, a further cut was applied to include only events within a cylindrical volume centered on the IP. The inner radius of the LAr barrel calorimeter (1150 mm) was used as the limit in the following way:

$$\sqrt{x^2 + z^2} < 1150 \quad (6.4)$$

where x and z refer to the position of the LAr cells in the x and z directions, respectively. The application of this cut removed events which produced hits at the calorimeter edges near the horizontal plane. Since the hits of such events occurred near the horizontal plane, they occurred close to the time at $y = 0$, between cells in the top and bottom. These events were therefore responsible for the small peak between the top and bottom peaks. With this cut applied, the result of the timing distributions is given in Figure 6.14. Yet another way to observe the effect of the timing distribution in this region is to remove the cut on the cylindrical volume and use the η and ϕ values of the cells for each event to make a cut on projectivity. A projective event can be defined as one which hits cells with the same η

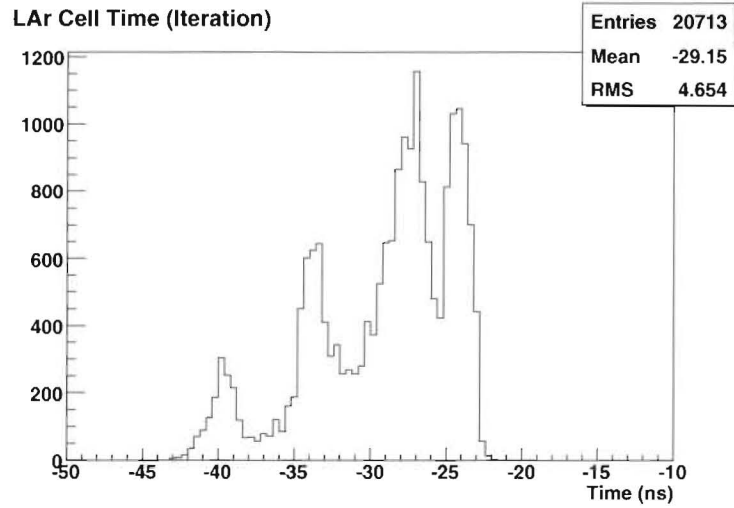


Figure 6.11: The LAr cell timing using the Iteration method with only those muons included which have a hit in both the top and bottom sections of the LAr barrel calorimeter.

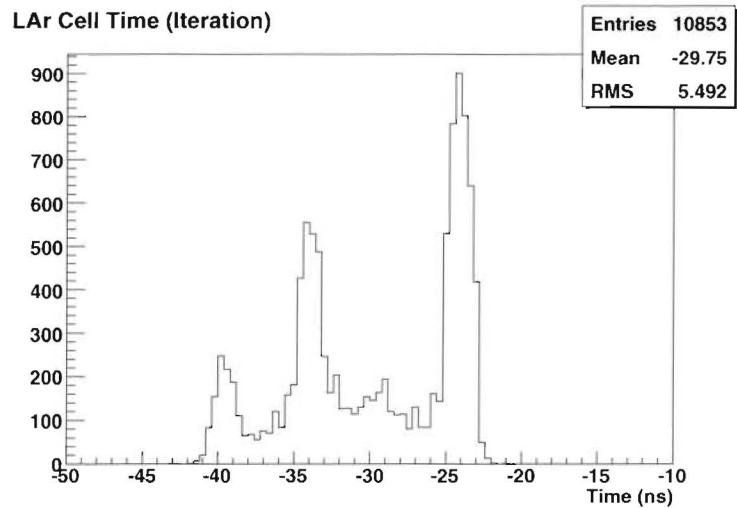


Figure 6.12: Similar to Figure 6.11, except that here only the middle layer of the LAr barrel calorimeter is included.

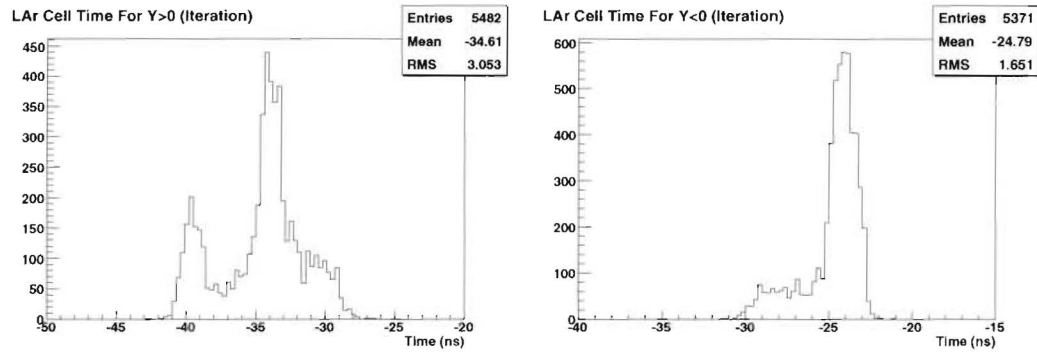


Figure 6.13: The same as in Figure 6.12, except that the top (left) and bottom (right) sections of the LAr calorimeter are shown separately.

and ϕ values, with only a change in sign between the top and bottom calorimeter sections. Using the cell granularity of the middle layer ($\Delta\eta \times \Delta\phi = 0.025 \times 0.025$), a cut was made to include only muons that hit cells with η and ϕ values within this granularity. In this way, all of the calorimeter volume is included, but only a very small number of muons pass the tight cut of being within one bin of the cell granularity in η and ϕ . The result is given in Figure 6.15 and it shows the effect of the timing of the cells in the region around the $y = 0$ plane. The peak in the middle is for cells at the calorimeter edges near the $y = 0$ plane.

There is clearly a second peak in Figure 6.14 for the top portion of the barrel calorimeter. This is most probably due to the fact that cosmic ray muons traverse cells in the top half of the barrel in the opposite direction to particles originating at the IP. This is not true for the bottom half, where the direction of the muons is the same as for $p - p$ collisions. For a given cell in the top, two timing offsets could combine together. One is an offset from the TOF through the cell, which given the width of a middle layer cell, is about 2 ns. Since the cabling offsets, which are arranged to correct for TOF differences from the IP, shift the timing in the wrong direction for cosmic ray muons going through the top calorimeter section, the timing will be shifted by about 4 ns overall. For most events, the timing at the cell would likely be in the middle of the cell. There are rare events, however, when a high energy muon undergoes bremsstrahlung in the cryostat walls located immediately in front of the cells in the top. This could shift the timing of the cell to one end for those particular events, possibly explaining the reason for the smaller second peak in the top section.

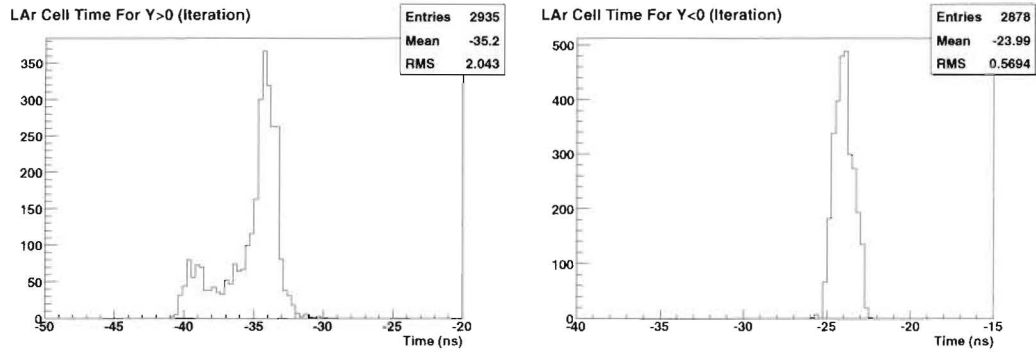


Figure 6.14: As in Figure 6.13, but including only those events which produce hits within the designated cylinder around the IP.

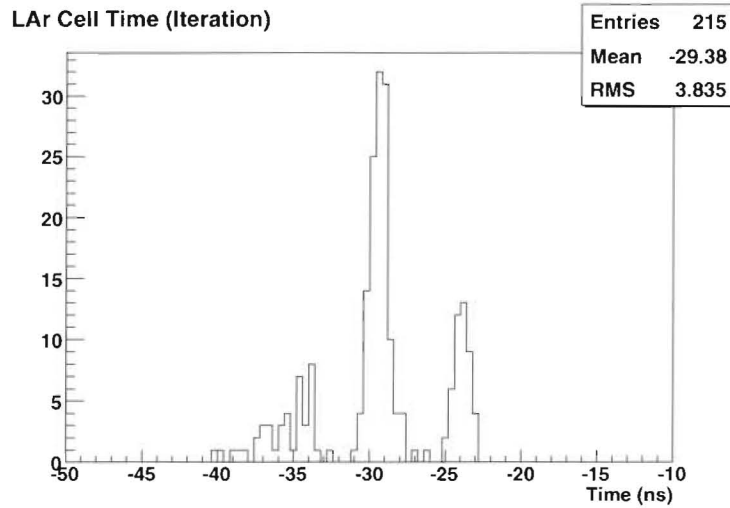


Figure 6.15: The same as in Figure 6.12, except here with a cut on projectivity using the η and ϕ values of the cells for each event. Only those events are included that produce hits in cells with η and ϕ values that fall within the granularity of middle layer cells.

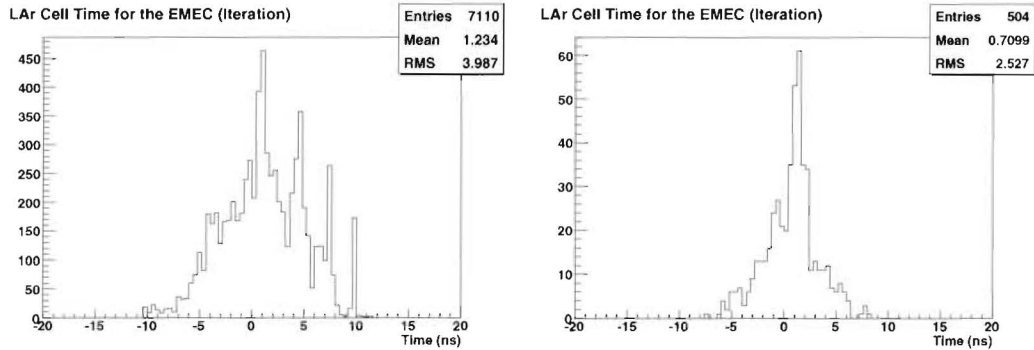


Figure 6.16: The LAr cell timing distribution in the EMEC using the Iteration tool on MC dataset 5003. This is performed for a minimum cell energy of 50 MeV (left) and 150 MeV (right).

6.4.2 MC Cosmic Rays in the Endcap Calorimeters

Here we describe the investigation of the timing in the endcap calorimeters using the results of MC dataset 5003, which is an endcap specific dataset.

The methods of the investigation here are similar to those mentioned above for the barrel calorimeter, except the main purpose here is to show how the cell energy threshold affects the timing distribution. It has been observed that in the endcap calorimeters, increasing the minimum cell energy changes the timing distribution to a more well-defined peak. We apply similar cuts, including the cut on cells outside the 20 cm proximity to the TMF muon track and in this case we only include events which hit the Tile extended barrel. Both the Iteration and TileInfo reconstruction tools were applied and the results compared. There was again very good agreement between the two results and therefore only the Iteration tool results are shown here. In Figure 6.16, the timing distribution for only the cells in the EMEC are shown for both a cell energy threshold of 50 and 150 MeV. It indicates that the timing distribution becomes more well defined at higher cell energies. This can be explained by the observation that because of their non-projective nature, cosmic ray muon energies in the endcaps need to be larger to produce a well defined signal. The same is done for the HEC, but because the average energy deposit in the HEC is much higher than in the EMEC, it appears to require a proportionally higher cell energy threshold to remove the multiple peaks in the timing distribution. These results are shown in Figure 6.17.

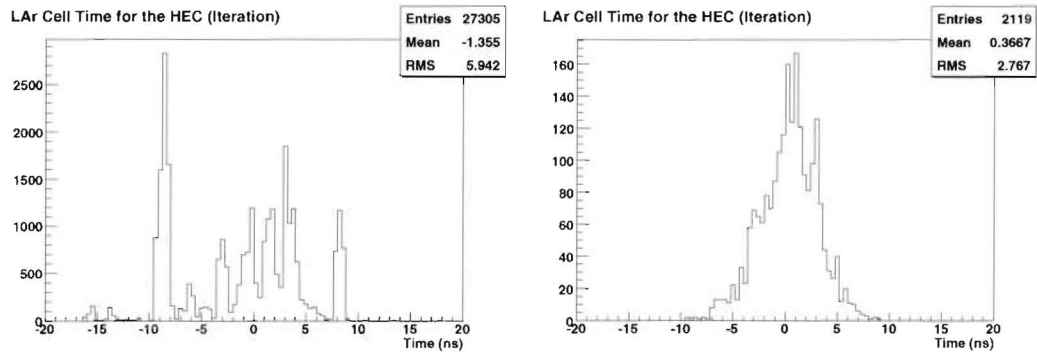


Figure 6.17: The LAr cell timing distribution in the HEC using the Iteration tool on MC dataset 5003. This is performed for a minimum cell energy of 150 MeV (left) and 850 MeV (right).

6.5 Cosmic Ray Data Analysis

6.5.1 Setup

Cosmic ray data were taken in the LAr calorimeters jointly with the Tile calorimeter. Data taking first began in late August 2006 and is ongoing. The first stage of combined LAr/Tile calorimeter data taking occurred in August and October 2006 with 4 LAr barrel crates connected as well as 8 Tile modules in each of the top and bottom sections connected to the trigger boards. Another significant set of cosmic ray data was taken in the LAr barrel calorimeter in March/April 2007. For these runs, several more LAr crates were connected in both top and bottom sections of both the A-side and C-side. The Tile, meanwhile, had a few more modules connected, but for approximately half of these runs the lower modules on the Tile barrel C-side, called LBC, were not connected. In April/May 2007, the Tile extended barrel and one LAr endcap calorimeter (ECA) were connected. Only the EMEC was initially available and there were issues with low trigger rates and a large time offset between the Tile barrel and extended barrel, but these issues were resolved. In June/July 2007, all of ECA as well as most of the LAr barrel and Tile barrel and extended barrel were connected. Table 6.2 gives the details for each of these data taking periods, including the LAr crates and Tile modules that were connected and the number of events from cosmic rays that were recorded. The run numbers indicate the runs that were used for the analysis in this work. Although all the runs mentioned were analyzed, only results from the Aug/Oct 06

and Jun/Jul 07 will be described here. The reasons for this are given below, but generally are related to a lack of interesting events required for this analysis. The labeling of the LAr crates and Tile modules used in Table 6.2 describes their physical locations within the calorimeters. Diagrams of the labeling of crates within the LAr barrel and endcap are given in Appendix A. To simplify, in the LAr barrel, the label I denotes crates in the A-side while the label H is used for crates in the C-side. For the LAr endcap, the label A denotes crates in endcap A, which is the only side to take cosmic data used for this work. For the Tile calorimeter, LBA and LBC refer respectively to the A-side and C-side of the main barrel section, while EBA refers to the Tile extended barrel on the A-side. For both the LAr crates and Tile modules given in Table 6.2, the top row always refers to the top section of the calorimeter, whereas the bottom row is for the bottom section. In cases where a different number of crates or modules was connected for different runs, the most common layouts are given for each data taking period.

Table 6.2: Details of the cosmic ray data taking periods used for this analysis. This information is taken mainly from [23]. Under the LAr Crates and Tile Modules columns, the top rows refer to the top sections of the calorimeter ($y > 0$) and the bottom rows refer to the bottom calorimeter sections ($y < 0$). The layouts of the LAr crates are given in Appendix A.

Run Period	Run Numbers	LAr Crates	Tile Modules	Events Recorded ($\times 10^3$)
Aug/Oct 06	7810-7814, 8035, 8037, 8051, 8055, 8077	H04,H05(C) I12,I13(A)	LBC13-20 LBA45-52	91.4
Mar/Apr 07	1586,2060	I04-I06(A);H05,H06(C) I12,I13(A);H13,H14(C)	LBC15-18;LBA15-18 LBC47-50;LBA47-52	31.1
Apr/May 07	7375,10093	I04-I06(A);H04-H06(C);A01-A06 I12-I14(A);H13,H14(C);A09	LBC15-18,20;LBA11-22;EBA17-20 LBA45,47-54;EBA43-54	5
Jun/Jul 07	14066, 14110, 14834, 14843, 14848,	I04-I06(A);H01-H07(C);A01-A07 I12-I14(A);H12,H14-H16(C);A08-A13	LBA;EBA;LBC (All) LBA;EBA (All);LBC(Half)	12.3

6.5.2 Combined LAr/Tile Barrel Runs

The first set of cosmic ray data using the combined LAr and Tile barrel calorimeters was taken in August and October 2006. The entirety of this dataset was reconstructed using the reconstruction tools described in earlier sections. The results of the Iteration tool were used to compute t_{global} to be used by the TileInfo tool. The results are given in Figure 6.18. Although Table 6.2 indicates that for this data taking period the number of LAr crates connected in the top and bottom sections was equal (2 crates each), for runs 7810-7814 only one crate in the bottom was connected. The result is a larger number of events in the bottom section than the top, as can be seen from Figure 6.18.

A comparison between the reconstructed LAr cell times using the Iteration, Fixed, and TileInfo tools is given in Figure 6.19. The minimum cell energy required in this case was 350 MeV and as with the MC analysis, only cells within 20 cm of the muon track from TMF were included. Again it is clear that for these high energy events the cell time derived by the Iteration and TileInfo tools agree. It was found that using a fixed time sample and phase also yields a cell time that agrees with the result of the Iteration tool. This is mainly because for this data taking period the same cells within the top and bottom of the LAr barrel were connected for all recorded events. The layout of the connected cells was also such that the events were highly projective.

The approximate TOF of a cosmic ray muon from the top of the Tile calorimeter to the bottom is 30 ns. The peak of the LAr signal would therefore likely occur within a single 25 ns time sample for each projective event, with a variation resulting from the shortest and longest possible muon tracks through these particular LAr cells. In fact, for projective muons, the TOF between each LAr cell and the IP, should be approximately equal to the TOF from the LAr cell to the $y = 0$ position of the TMF muon track, which respectively correspond to the variables TOF_{IP} and $TOF_{y=0}$ of Equation 6.2. These values were calculated separately for the top and bottom LAr sections and are plotted as a function of the LAr cell time in Figure 6.20, as determined by the TileInfo tool. From Equation 6.2, we know that for the bottom section TOF_{IP} is subtracted from $TOF_{y=0}$, and should therefore equal zero if they are equal. This is indeed the case, as seen in the right plot of Figure 6.20, with an RMS of less than 1 ns. In the case of the top section, both of these two TOF variables are subtracted from each other, and it was found using the actual positions of the cells connected during this data taking period, that the expected total TOF ranges

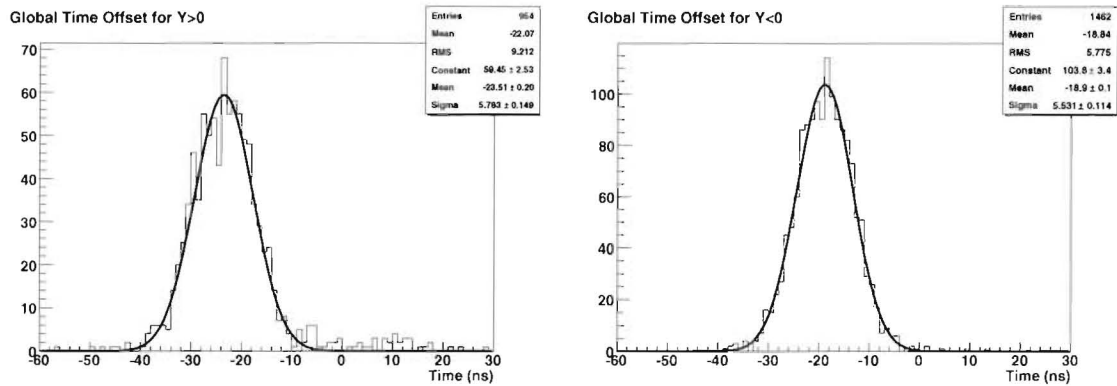


Figure 6.18: A Gaussian fit of the global time offset t_{global} between the LAr and Tile barrel calorimeters for the top (left) and bottom (right) LAr sections.

from 13 to 17 ns based on the shortest and longest possible tracks. This expectation is also observed in the left plot of Figure 6.20, confirming that the cosmic ray muon events recorded during this data taking period were highly projective and therefore a fixed time sample and phase determined the cell times with good accuracy. However, as seen in Figure 6.19, the distribution of the cell time from the Fixed method is narrower than the others and contains fewer entries, since it fails at reconstructing those muons which fall outside of the single time sample, whereas the other two tools successfully reconstruct those events.

Section 6.6 shows the results of the LAr cell energy distributions found for each method of reconstruction.

The combined LAr/Tile barrel cosmic data taken in Mar/Apr 07 were also analyzed in a similar way. Unfortunately the number of cosmic muon events were too few to make any conclusions. Even with the small number of events and large statistical fluctuations, it was found that t_{global} was shifted by more than a 25 ns time sample from the Aug/Oct 06 data. It was therefore noted that the internal clocks of the Tile and/or LAr were changed between the two runs.

6.5.3 Combined LAr/Tile End-Cap Runs

The data taken in Apr/May 07 included the LAr endcap for the first time, but the HEC and FCAL were not yet available, so only the EMEC was connected. Additionally, many of the conditions data such as ramps, pedestals, and OFCs for the endcap crates were not

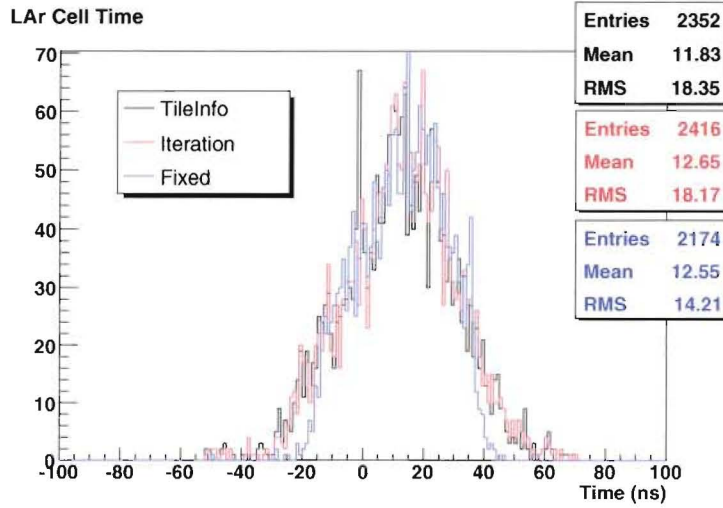


Figure 6.19: A comparison between the results of the LAr cell times for EM barrel data taken in Aug/Oct 2006.

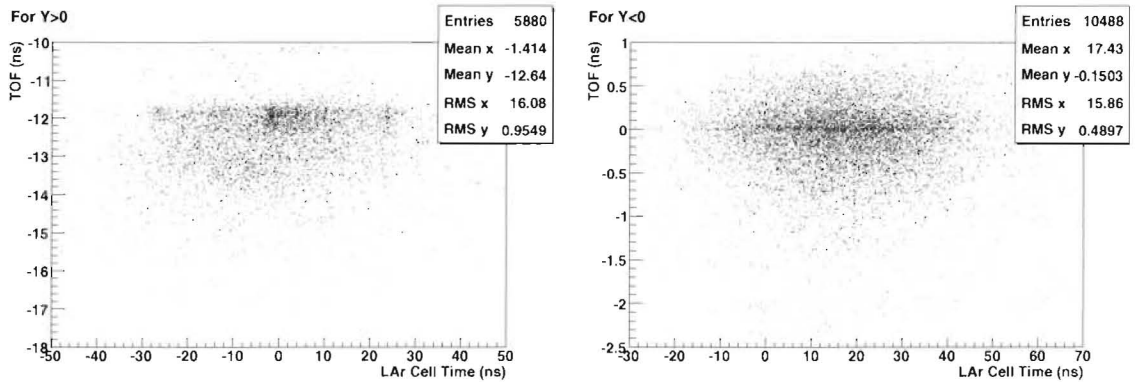


Figure 6.20: The TOF of each LAr cell to the $y = 0$ plane (TOF_{IP} and $TOF_{y=0}$) as a function of the cell time for projective cosmic muon events in the LAr barrel. The left plot is for cells in the top section and the right for cells in the bottom section.

accessible from the database. For most events, the Iteration and TileInfo tools failed as a result and the average tool was used. Consequently, a proper analysis of the timing in the endcap was not possible with data taken during this period.

In Jun/Jul 07, a large set of cosmic ray data was taken with most of the LAr barrel C-side, all of endcap A, approximately 1/3 of LAr barrel A-side, and all of the Tile A-side and C-side, with the exception of approximately 1/2 of the bottom of the Tile barrel C-side. The total calorimeter coverage during this data taking period for LAr cells that had calibration data available is shown in Figure 6.21. The LAr cell times were reconstructed using the Iteration and TileInfo tools, but now with a focus on the data in the endcap. Unlike the barrel data, these are non-projective events and consequently the energy in the endcap cells is deposited differently than what they were designed for. The LAr cell times computed by these two tools are shown in Figure 6.22. This was done for only the HEC cells, since there was some unknown problem for these runs in the EMEC and there were no conditions data available for the FCAL. The minimum cell energy required in the HEC was 500 MeV in this case. Although some cells in the HEC have noise levels beyond this value, we found that increasing beyond this threshold reduced the number events too much without changing the overall distribution. From Figure 6.22, we see again that the Iteration tool finds many noisy cells, whereas the TileInfo tool reconstructs only those cells for which valid information from the Tile calorimeters is available. Refer to Section 6.6 for results of the LAr cell energy distributions derived from these data, as well as a comparison with MC dataset 5003 with noise included.

6.6 Cosmic Ray Energy Deposits

Here we present the results of the energy deposits in the LAr calorimeters for cosmic rays from both MC and real data.

Figure 6.23 shows the comparison of the results of the cell energy between the Iteration, Fixed, and TileInfo tools applied to MC dataset 5003 with electronics noise included. There are generally more entries for the Iteration tool than for the TileInfo tool because the Iteration method tends to reconstruct noisy cells in addition to cells with valid muon energy deposits. In this case, the average cell energy is larger for the Iteration tool result than the TileInfo result because as seen in Figure 6.23, the Iteration tool reconstructs many noisy cells in the FCAL which were found to have cell energies greater than 2 GeV.

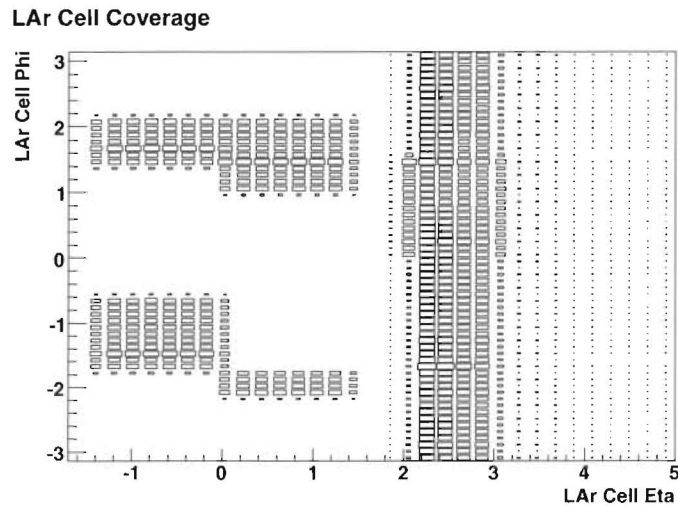


Figure 6.21: The LAr cell coverage during the combined LAr/Tile cosmic data taking period of Jun/Jul 07. The cells shown here are only those for which calibration data were available.

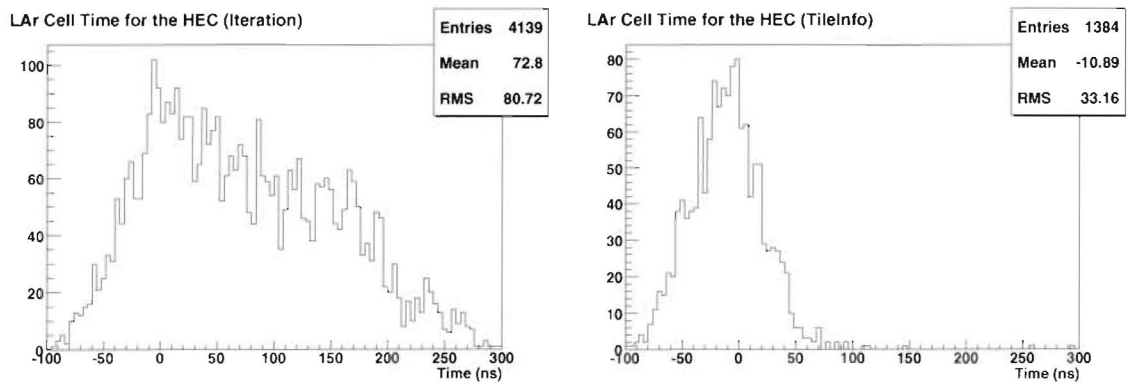


Figure 6.22: The results of the LAr cell times for cosmic data taken in the HEC, on the A-side. The cell times are computed using the Iteration (left) and TileInfo (right) tools for comparison. The minimum cell energy required in the HEC is 500 MeV in this case.

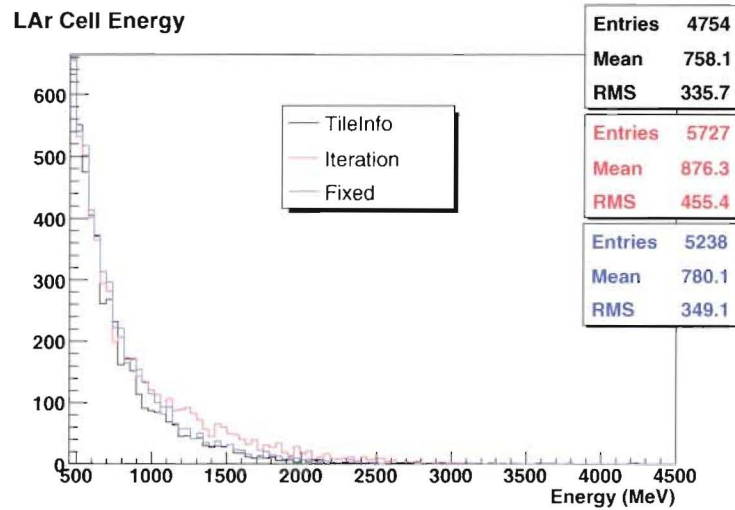


Figure 6.23: The energy deposited per cell for MC dataset 5003 with noise included, found using the Iteration, Fixed, and TileInfo reconstruction methods. The minimum LAr cell energy required is 450 MeV.

In Figure 6.24, the cell energy is again compared for each reconstruction method, but now for real data in the barrel calorimeter. The average cell energies for each of the three methods agree since the cell timing was in good agreement, as seen in Figure 6.19.

A comparison between the reconstructed cell energy of real cosmic ray muons in the HEC for the Iteration and TileInfo tools is given in Figure 6.25. In this case, the Iteration tool yields a lower average cell energy than the TileInfo tool. This is a result of the Iteration tool reconstructing noisy cells in the HEC with low signal amplitudes. Finally, Figure 6.26 compares the cell energy in the HEC for real data and MC cosmic dataset 5003, digitized with noise. There is reasonable agreement in the average cell energy reconstructed using the TileInfo tool.

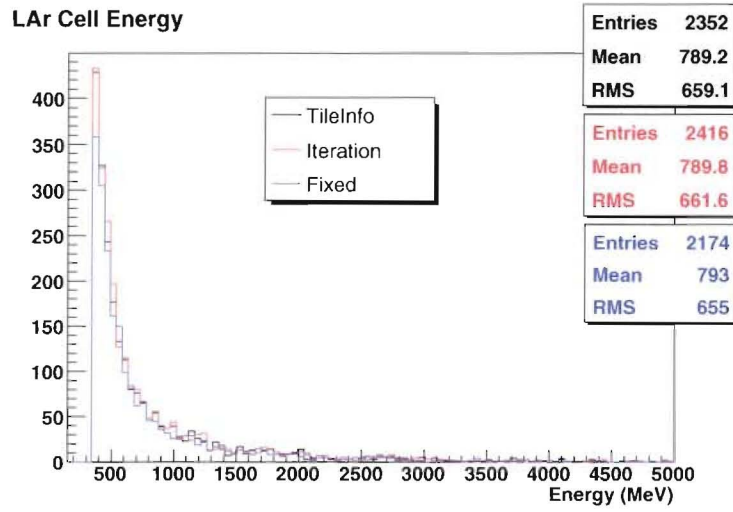


Figure 6.24: The energy deposited per cell for real data in the LAr electromagnetic barrel (EMB) calorimeter using each of the reconstruction methods; TileInfo, Iteration, and Fixed.

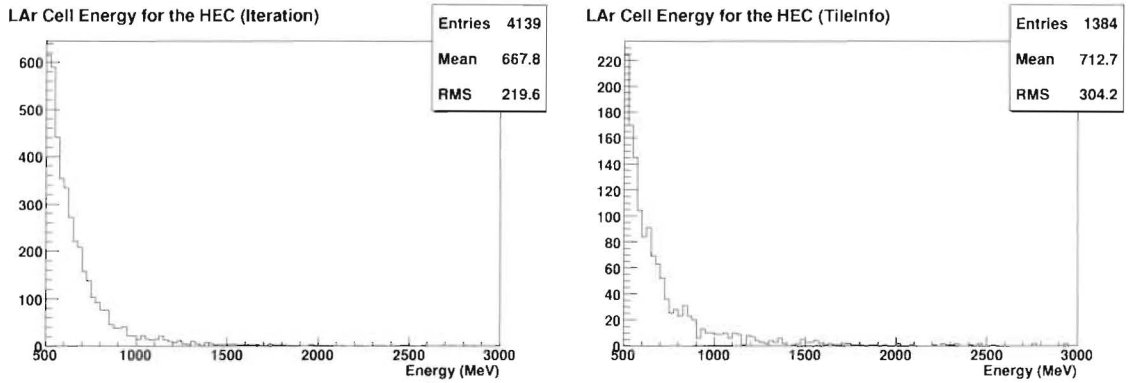


Figure 6.25: The energy deposited per cell in the LAr hadronic endcap (HEC) calorimeter using the Iteration (left) and TileInfo (right) reconstruction tools.

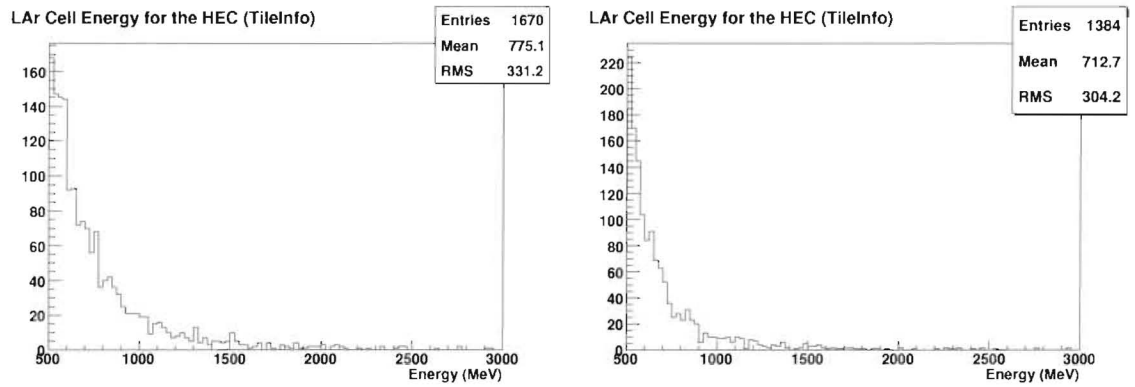


Figure 6.26: The energy deposited per cell in the LAr hadronic endcap (HEC) calorimeter for MC dataset 5003 with noise included (left) and real data (right) using the TileInfo reconstruction tool.

Chapter 7

Conclusion and Outlook

The commissioning of the LAr calorimeters is currently in full operation. Calibration data are being taken in the LAr endcaps for cold commissioning, and in all other calorimeters cosmic ray data are taken at every available opportunity. The calibration data are essential for the correct reconstruction of the energy deposited in the calorimeters and cosmic ray data are particularly useful for being ready for $p - p$ collisions at the LHC in 2008.

In this work we described the Warm/Cold commissioning phase in the LAr endcap calorimeters and showed why this is important for real data taking. The calibration data taken in the form of pedestal, delay, and ramp runs have been used to form a more complete conditions database. This database contains essential conversion factors for energy reconstruction. Testing of the front-end electronics has led to the repair and replacement of electronic components which would have resulted in dead or distorted channels if not addressed properly. This testing continues with cosmic ray data.

Commissioning with cosmic rays was the first opportunity to take real data in the calorimeters, as well as all other detector systems in ATLAS. The MC analysis performed was used to determine the feasibility of this commissioning phase and the results were also used to shape the cosmic ray data taking effort.

The good agreement between the results of the muon gun and air shower cosmic ray generators showed that the muon gun was an acceptable method for MC production of cosmic rays in ATLAS. The results of the MC simulations performed with the muon gun were used in the analysis of the signal reconstruction in the LAr calorimeters. Since dedicated trigger boards were built to be used on the Tile calorimeter, a new reconstruction tool was written to use the information from the Tile calorimeters in order to better reconstruct

the signals in the LAr calorimeters from cosmic ray muons. Both the MC simulation and real data in the LAr barrel and endcap calorimeters were analyzed with this and other reconstruction tools. In particular, the Iteration tool, which iterates over time samples to find the signal peak, was tested. We found that the tool using the Tile calorimeter information, the TileInfo tool, reconstructed the time more accurately than the Iteration tool and was better at avoiding noisy cells. This tool is part of the software package used to analyze data in ATLAS, and is recommended for use in reconstructing data from cosmic rays in the LAr calorimeters.

The steps taken in this work have helped in the commissioning effort of the LAr calorimeters, which are closer to being ready for real data from collisions at the LHC.

Bibliography

- [1] ATLAS Detector Photos. ©The ATLAS experiment at CERN.
<http://atlas.ch/atlas-photos.html>
- [2] LHC Design Report Volume I, 2006.
<http://ab-div.web.cern.ch/ab-div/Publications/LHC-DesignReport.html>
- [3] C. Vanoli, *CERN-DI-0606052 - Accelerators [sic] complex of CERN*, 30 June 2006.
<http://doc.cern.ch//archive/electronic/cern/others/PHO/photo-di/0606052.pdf>.
- [4] ATLAS Detector and Physics Performance Technical Design Report, Volumes I and II, CERN/LHCC 99-14 and CERN/LHCC/99-15, 25 May 1999.
©The ATLAS experiment at CERN.
- [5] ATLAS Collaboration. The ATLAS Experiment at the CERN Large Hadron Collider. Submitted to *JINST*, 24 December 2007.
- [6] H. Gimm J. Hubbell and I. Overbo. *J. Phys. Chem. Ref. Data*, 9:1023, 1980.
- [7] R. Wigmans. *Calorimetry: Energy Measurement in Particle Physics*. New York: Oxford University Press, 2000.
- [8] P. Krieger. The ATLAS Liquid Argon Calorimeter: Construction, Integration, Commissioning and Performance from Selected Particle Beam Test Results. *IEEE Nuclear Science Symposium Conference Record*, 2005.
- [9] M. Boonekamp, F. Gianotti, R.A. McPherson, M. Nessi, and P. Nevksi. Cosmic Ray, Beam-Halo and Beam-Gas Rate Studies for ATLAS Commissioning. *ATLAS Internal Note*, ATL-GEN-2004-001, 2004.

- [10] K. Anderson, J. Pilcher, H. Sanders, F. Tang, and R. Teuscher. Stand-alone Cosmic Ray Trigger Electronics for the ATLAS Tile Calorimeter. *Proceedings of the 10th Workshop on Electronics for LHC Experiments and Future Experiments*, 2004.
- [11] ATLAS Liquid Argon Calorimeter Technical Design Report, 1996.
©The ATLAS experiment at CERN.
<http://atlas.web.cern.ch/Atlas/GROUPS/LIQARGEXT/TDR/ps.html>.
- [12] LArEndcapP3Commissioning.
<https://twiki.cern.ch/twiki/bin/view/Atlas/LArEndcapP3Commissioning>
- [13] N.N. et al., Electromagnetic Energy Measurement in LAr Calorimeter at the CTB 2004, JINST 888 (2008) to be submitted to JINST.
- [14] B. Dowler et al., Performance of the ATLAS hadronic end-cap calorimeter in beam tests, Nucl. Inst. 11295 Meth. A482 94124, 2002.
- [15] J.P. Archambault et al., Energy Calibration of the ATLAS Liquid Argon Forward Calorimeter, JINST 888 (2008) accepted by JINST.
- [16] W.-M. Yao, et al. Review of Particle Physics. *Journal of Physics G*, 33:1, 2006.
- [17] CORSIKA: An Air Shower Simulation Program.
<http://www-ik.fzk.de/corsika/>
- [18] National Geophysical Data Center (NGDC).
<http://www.ngdc.noaa.gov/seg/geomag/magfield.shtml>.
- [19] A. Ahmad. Private communications.
- [20] W. E. Cleland and E. G. Stern. Signal processing considerations for liquid ionization calorimeters in a high rate environment. *Nuclear Instruments & Methods in Physics Research A*, 338:467-497, 1994.
- [21] J. Maneira. TileMuonFitter: An algorithm for the reconstruction of cosmic muons with the ATLAS Tile Calorimeter. *ATLAS Internal Note*, ATL-TILECAL-INT-2007-003, 2007.
- [22] H. Ma. Private communications.

[23] LArCosmicRunList.

<https://twiki.cern.ch/twiki/bin/view/Atlas/LArCosmicRunList>.

Appendix A

LAr Mapping Diagrams

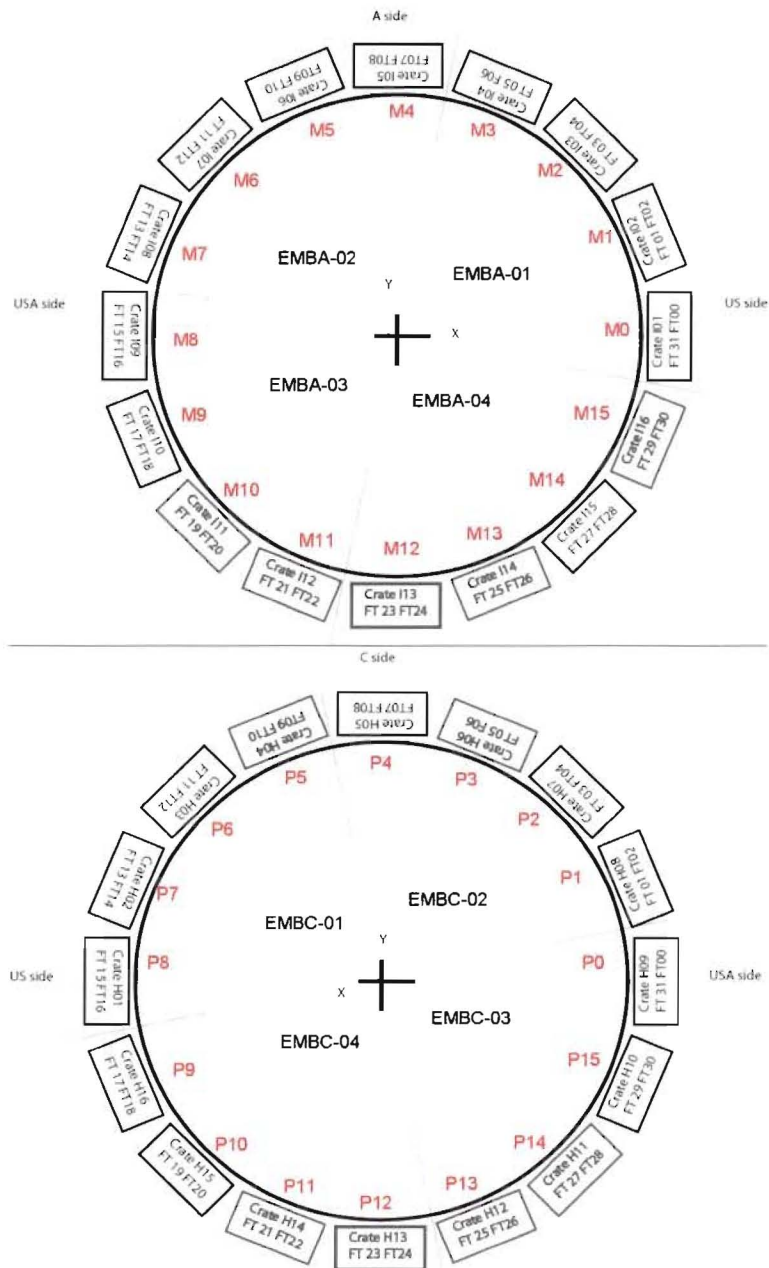


Figure A.1: The mapping of the crates in LAr barrel on the A-side (top) and C-side (bottom).

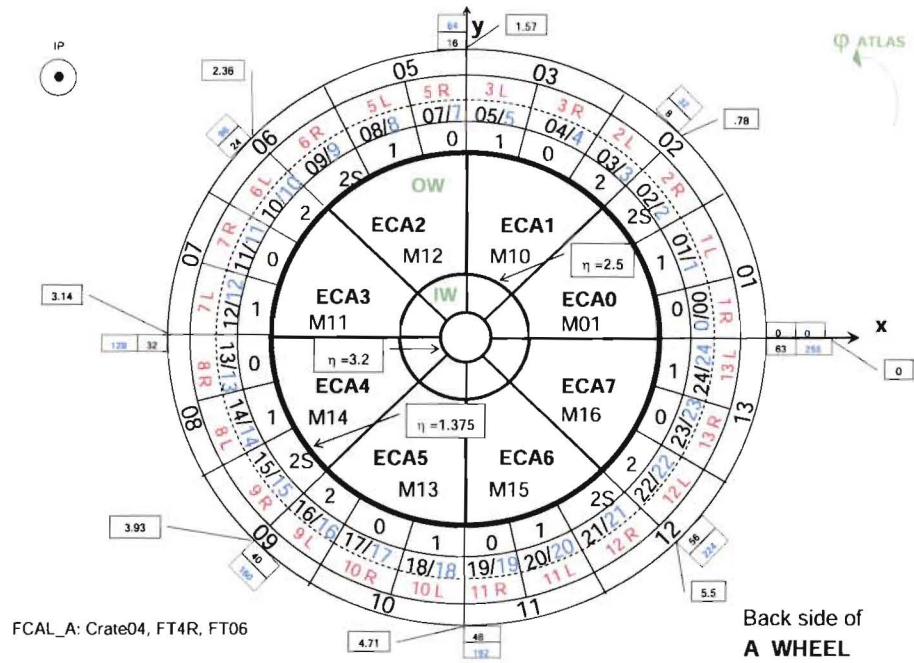


Figure A.2: The mapping of the crates in LAr endcap on the A-side.